Theory and calculations on the Herzberg states of the oxygen molecule

Mirjam C. G. N. van Vroonhoven

Theory and calculations on the Herzberg states of the oxygen molecule

een wetenschappelijke proeve op het gebied van de
Natuurwetenschappen, Wiskunde en Informatica

Proefschrift

ter verkrijging van de graad van doctor
aan de Katholieke Universiteit Nijmegen,
op gezag van de Rector Magnificus Prof. Dr. C.W.P.M. Blom,
volgens besluit van het College van Decanen
in het openbaar te verdedigen op
maandag 2 juni 2003,
des namiddags om 1.30 uur precies

door

Maria Cornelia Gertruda Nicolaas van Vroonhoven

geboren op 1 september 1975
te Sittard

Promotor: Prof. Dr. ir. A. van der Avoird

Copromotor: Dr. ir. G.C. Groenenboom

Manuscriptcommissie: Prof. Dr. D. Parker (voorzitter)
Dr. M.C. van Hemert (Universiteit Leiden)
Dr. ir. P.E.S. Wormer

M.C.G.N. van Vroonhoven
Theory and calculations on the Herzberg states of the oxygen molecule
PhD Thesis, University of Nijmegen, The Netherlands
With summary in Dutch
ISBN 90-9016851-6
printed by: PrintPartners Ipskamp, Enschede

This research has been financially supported by the Council for Chemical Sciences of the Netherlands Organization for Scientific Research (CW-NWO).

Dankwoord

Dit proefschrift heb ik natuurlijk niet alleen gemaakt. Heel veel mensen hebben er een bijdrage aan geleverd, waar ik heel erg dankbaar voor ben. In het bijzonder wil ik hier noemen:

- Gerrit Groenenboom voor de geweldige inspiratie, begeleiding en samenwerking de afgelopen jaren.
- Ad van der Avoird en Paul Wormer, jullie hebben mij wat meer op afstand begeleid, maar waren er toch altijd om te helpen moeilijke theorie te begrijpen en afleidingen en artikelen kritisch te bekijken.
- Gé Vissers, als mijn kamergenoot heb je jarenlang mijn muziek aangehoord.
- Alle andere (voormalige) medewerkers van de afdeling Theoretische Chemie: Tino Heijmen, Erik van Lenthe, Michael Smit, Christina Sanz Sanz, Victor Lotrich, Gilles Verbockhave, Michel Geleijns, Ine Meijer, Mark van der Loo, Wilfried Zeimen, Jacek Kłos en Eugenie Miseroy, voor de prettige samenwerking.
- Onze “buren”, de experimentatoren van de afdeling Molecuul- en Laserfysica: Dave Parker, André Eppink, Bart Buijsse en Dmitriy Chestakov, jullie hebben de velocity-mapped ion-imaging techniek bedacht en hebben de experimenten uitgevoerd, die de inspiratie vormden voor mijn onderzoek.
- Mijn ouders Christ en Ria, mijn zus Esther en Erik Verbruggen. Jullie bleven altijd in mij geloven en waren een hele grote steun voor mij, ook als het moeilijk was en tegenzat.
- En natuurlijk Arthur, Petra, Merijn, Annemieke, Koos, Ronald, Marjolijn en alle andere goede vrienden en vriendinnen die ik hier niet allemaal kan opsommen. We hebben altijd veel lol gemaakt, en zonder jullie support tijdens de laatste zware loodjes was dit proefschrift er niet gekomen.

Contents

Dankwoord **5**

1 Introduction **9**
- 1.1 Oxygen 9
- 1.2 The Born-Oppenheimer approximation 9
- 1.3 Non Born-Oppenheimer effects 11
- 1.4 The Herzberg states 12
- 1.5 photodissociation experiment 13
- 1.6 Bound state spectroscopy 16
- Bibliography 17

2 Photodissociation of O_2 in the Herzberg continuum. I. *Ab initio* calculation of potential energy curves and properties **19**
- 2.1 Introduction 19
- 2.2 Theory 22
- 2.3 Calculations 25
- 2.4 Analytic fit of potentials and couplings 28
- 2.5 Results and Discussion 31
- 2.6 Conclusion 41
- Bibliography 41

3 Photodissociation of O_2 in the Herzberg continuum. II. Calculation of fragment polarization and angular distribution **45**
- 3.1 Introduction 46
- 3.2 Theory 47
- 3.3 Results and discussion 56
- 3.4 Conclusion 64
- Appendix: Derivation of detection angular sensitivity 66
- Bibliography 67

4 Reassignment of the O_2 spectrum just below dissociation threshold based on *ab initio* calculations **69**
- 4.1 Introduction 69

4.2 Theory 71
4.3 Discussion 76
4.4 Summary and conclusions 86
Appendix: Basis functions and rotational Hamiltonian 87
Bibliography 93

5 *Ab initio* calculation of the intensities of the Herzberg I, II, and III bands of O_2 97

5.1 Introduction 98
5.2 Theory 99
5.3 Calculations 108
5.4 Results and discussion 114
5.5 Conclusion 134
Bibliography 135

Summary 139

Samenvatting 141

List of publications 143

Curriculum Vitae 145

Chapter 1

Introduction

1.1 Oxygen

The oxygen molecule (O_2) is very important to us. Most life would not be possible without oxygen. Atmospherical O_2 originates from the photosynthesis process, which occurs in plants. Absorption of solar ultra-violet (UV) radiation by O_2 molecules in the stratosphere leads to photodissociation of these molecules. The resulting oxygen atoms react again with oxygen molecules to form ozone (O_3), which also absorbs UV radiation in photodissociation, though at wavelengths different from the O_2photodissociation. In this way oxygen molecules protect life on earth from the harmful solar UV radiation.

Research, both theoretical and experimental, has been performed on the oxygen molecule for several other reasons. First of all, because of scientific curiosity, and because it is fun to investigate oxygen. It is also a small, relatively simple molecule. This makes it possible to use it as a test case in fundamental research. In theoretical calculations, the molecule is small enough that very high-level, very accurate calculations are feasible using present computers. In this thesis, we present theoretical and computational studies of the oxygen molecule. In the remainder of this introduction we discuss some theoretical background, and we describe in considerable detail the photodissociation experiment that motivated the studies presented in this thesis, in particular the study in Chapter 3.

1.2 The Born-Oppenheimer approximation

Exact solutions of the Schrödinger equation, the basic equation of non-relativistic quantum mechanics, do not exist for O_2. Approximations must be made to solve this equation. Oxygen consists of eighteen particles: two nuclei and sixteen electrons, which we consider as electrically charged point masses. The nuclei are about thirty thousand times as heavy as the electrons, and

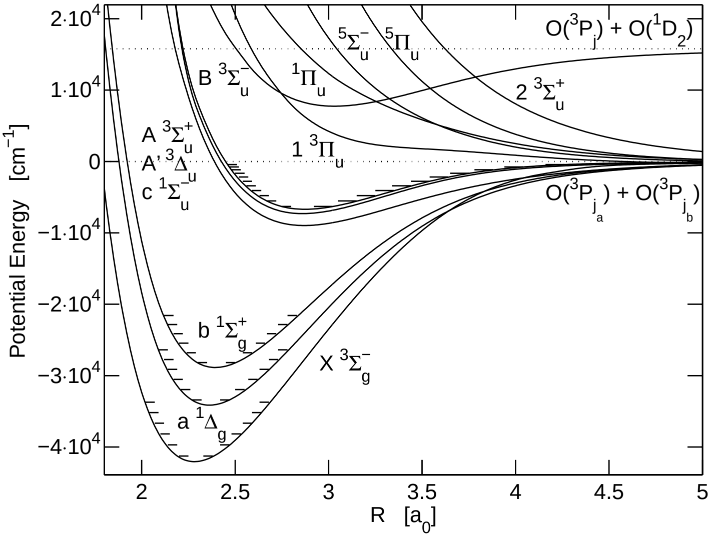

Figure 1.1: Potential energy curves for most of the electronic states of oxygen playing a role in this thesis.

have much less kinetic energy. In 1927 Max Born and Robert Oppenheimer[1] developed the formalism that is now known as the Born-Oppenheimer (BO) approximation. They assumed the nuclei to be stationary for the description of the electronic motion, i.e. the electrons adapt their motion instantaneously to the changing nuclear geometry, minimizing their total (electrostatic potential plus kinetic) energy. The nuclei move in the potential caused by the fast-moving electrons. In this approximation the Schrödinger equation separates into two differential equations, one for the electrons and one for the nuclei.

In the first step of the BO approximation the nuclear kinetic energy term is neglected in the Hamiltonian, and the electronic Schrödinger equation is solved for a set of fixed nuclear geometries (a set of values for the internuclear distance R). This yields electronic energies as function of R, the electronic potential energy curves. The potential energy curves for several electronic states of oxygen are shown in Fig. 1.1. For small R the electronic energy rises very steeply. For large R the electronic energy becomes a constant, the dissociation limit. The zero-point of energy in Fig. 1.1 is the lowest dissociation limit of O_2, the energy of two ground state oxygen atoms.

In the second step of the BO approximation, the nuclear dynamics is considered. The nuclei vibrate in the potential field from the electrons and the internuclear Coulomb repulsion. The nuclei can be in different vibrational states, depending on the form of the potential energy curve for the state the electrons are in. Some potentials in Fig. 1.1 decrease monotonically, for example the states $^1\Pi_u$, $^5\Pi_u$, $^5\Sigma_u^-$, and $2^3\Sigma_u^+$. These states are called repulsive. If the electrons of an oxygen molecule get excited to such a state the molecule will dissociate. Stable vibrational states are only possible for electronic states that have a well for some value of R. The oxygen molecule has six of these strongly bound electronic states below its first dissociation limit: the ground state $X^3\Sigma_g^-$, two low-lying gerade states $a^1\Delta_g$ and $b^1\Sigma_g^+$, and the three Herzberg states $c^1\Sigma_u^-$, $A'\ ^3\Delta_u$, and $A^3\Sigma_u^+$. This thesis focuses mainly on the Herzberg states. The $1^3\Pi_u$ state seems repulsive, but it has a very shallow minimum at $R \approx 5.5$ a$_0$, in the long-range. These states all dissociate into (correlate with) ground state (^3P) oxygen atoms. The $B^3\Sigma_u^-$ state is an example of a bound electronic state that dissociates into an excited state atom ($^1D_2$) and a ground state atom. The small horizontal dashes in the bound potential energy curves in Fig. 1.1 indicate the energies of the nuclear vibrational levels in these states. For example, $v = 0$ to 6 are indicated for the ground state, and $v = 0$ to 10 for $A^3\Sigma_u^+$. The molecule also rotates, with total angular momentum quantum number J. The energy difference between the rotational levels is too small to visualize in Fig. 1.1. One quantum state of the molecule is defined by specification of the electronic, vibrational, and rotational state, and hence it is called a rotational-vibrational-electronic (RVE) state.

1.3 Non Born-Oppenheimer effects

Within the Born-Oppenheimer approximation the nuclear dynamics is treated for each electronic state separately. When two electronic states are close in energy, this is not a valid approximation. This is the case, in particular, in the long-range, where several electronic states approach the same dissociation limit. Here we have to take couplings between the electronic states into account, that were neglected in the calculation of BO potentials.

Spin-orbit interaction (the coupling between the electronic orbital angular momentum and the electron spin) is ignored in the electronic Hamiltonian used in the first step of the BO approximation, as the spin-orbit coupling is usually small compared to the Coulomb interaction. However, spin-orbit coupling is important for the oxygen molecule in the long-range, as it determines the three fine-structure states of ground state O(^3P_j) ($j = 2, 1, 0$) atoms. Spin-orbit coupling may thus induce transitions between Born-Oppenheimer electronic eigenstates in the long-range.

Interactions between the rotational angular momentum and the electronic orbital and spin angular momenta (orbit-rotation and spin-rotation interactions) give also rise to couplings between BO eigenstates, just as the radial derivative coupling ($\partial/\partial R$ matrix elements). Non-BO effects can be important even when the interacting states are not close in energy, for example in the electronic dipole transition from the ground state to the Herzberg states.

This transition is forbidden in the BO approximation, and gains intensity only after inclusion of non-BO effects.

1.4 The Herzberg states

The story of the Herzberg states, that this thesis is about, started in 1932 when Gerhard Herzberg[2] observed very weak absorption bands of the electric dipole forbidden transition from the ground state to $A^3\Sigma_u^+$, the transition that is now known as Herzberg I. The rotational analysis was given in 1952 by Herzberg.[3] The Herzberg II and III transitions (from the ground state to $c^1\Sigma_u^-$ and $A'\ {}^3\Delta_u$ respectively) were also first observed by Herzberg in absorption,[4] and he presented the rotational analysis in 1953.

After the pioneering work of Herzberg, much other work has been done on these states, both theoretical and experimental. The theoretical work was performed mostly within the Born-Oppenheimer approximation: calculation of electronic potential energy curves and rovibrational levels.[5,6] In this thesis we also calculate potential energy curves (Chapter 2). However, non Born-Oppenheimer effects are very important in the description of the O_2 Herzberg states, as we will show in this thesis. In photodissociation, spin-orbit couplings determine the distribution over atomic fine-structure states, and the polarization of the photofragments, i.e., the relative populations of the m components of the atomic fine-structure states. We study these quantities in Chapter 3. This photodissociation process has also been studied experimentally by many people, see Ref. 7 and references therein. We focus on the experiment from Ref. 7, which uses the new velocity-mapped ion-imaging technique. This photodissociation experiment is described in Sec. 1.5 of this introduction.

These spin-orbit couplings also affect the bound RVE states. The shallow long-range minimum of $1^3\Pi_u$ supports two vibrational levels, and spin-orbit coupling of $1^3\Pi_u$ with the Herzberg states perturbs the Herzberg spectra just below the dissociation limit. Employing our potentials and spin-orbit couplings we perform full RVE state calculations in Chapter 4. We found a new assignment of the perturbing levels of the $1^3\Pi_u$ state.

The excitation mechanism of the Herzberg transitions is studied in Chapter 5. The Herzberg transitions are all electric-dipole forbidden, they only gain intensity through spin-orbit and orbit-rotation coupling. A first attempt to include these effects was the calculation by Klotz and Peyerimhoff[8] of electronic transition moments. We apply our excitation mechanism in the calculation of line intensities in the bound state part of the Herzberg spectrum. These integrated line cross-sections have been measured very accurately,[9–12] the experiments are described in Sec. 1.6. This excitation mechanism also influences the photodissociation. The three Herzberg states yield different photofragment fine-structure distributions and polarizations, and the excitation mechanism determines the relative intensities of the three contributing states. Also interferences between the three states are possible.

1.5 Photodissociation experiment: photofragment fine-structure distribution and polarization

In a photodissociation process several vector quantities play a role: the polarization vector $\underline{e}$ of the photolysis laser, the transition dipole moment vector $\underline{\mu}$ of the molecule, the relative velocity vector $\underline{v}$ of the recoiling fragments, the total angular momentum $\underline{\hat{J}}$, and the total angular momenta $\underline{\hat{j}_a}$ and $\underline{\hat{j}_b}$ of both fragments. All these vectors can be related to the laboratory-fixed direction of the laser polarization $\underline{e}$. In addition to scalar properties of the photofragment distribution over atomic fine-structure levels O(^3P_j) we study in Chapter 3 the correlation between $\underline{e}$ and $\underline{v}$, i.e., the angular distribution of photofragments, and the correlation between $\underline{e}$ and the fragment angular momenta $\underline{\hat{j}_a}$ and $\underline{\hat{j}_b}$, i.e., the fragment polarization, characterized by the distribution over the magnetic sublevels m_a, m_b.

In the axial recoil approximation, the two atomic fragments are assumed to recoil along the direction of the internuclear axis at the time of excitation into the continuum state. For a parallel transition ($\Sigma \leftarrow \Sigma$, $\Pi \leftarrow \Pi$) the transition dipole moment $\underline{\mu}$ is oriented along the internuclear axis, and thus, in the case of direct dissociation $\underline{\mu} \parallel \underline{v}$. For a perpendicular transition ($\Sigma \leftarrow \Pi$, $\Pi \leftarrow \Delta$) the transition dipole moment lies perpendicular to the axis, so $\underline{\mu} \perp \underline{v}$. The interaction between the electric field of the photon and the transition dipole moment is given by $\underline{e} \cdot \underline{\mu}$, and the transition intensity depends on the angle between $\underline{e}$ and $\underline{\mu}$, and hence on the angle θ between $\underline{e}$ and $\underline{v}$. The θ dependence of the photofragment angular distribution for a one-photon transition is given by[13]

$$\frac{d\sigma}{d\Omega}(\theta) = \frac{\sigma}{4\pi}[1 + \beta P_2(\cos\theta)], \tag{1.1}$$

where σ is the total cross section. For a purely parallel transition, we have a $\cos^2\theta$ distribution, and for a purely perpendicular transition, the distribution is $\sin^2\theta$. Using the second-order Legendre polynomial $P_2(\cos\theta) = (3\cos^2\theta - 1)/2$ and the anisotropy parameter β we find $\beta = 2$ for a parallel transition, $\beta = -1$ for a perpendicular transition, and an intermediate β for transitions of mixed character.

The angular distribution of photofragments can be measured in an ion-imaging experiment.[14] The molecules are dissociated with a polarized laser pulse, and the resulting fragments are state-selectively detected with resonance enhanced multiphoton ionization (REMPI). A second laser pulse ionizes the atomic photofragments. The ions are accelerated by an electric field towards the detector which consists of a dual microchannel-plate, phosphor screen and CCD camera. The highest spatial resolution is achieved with velocity-map ion imaging,[15,16] invented by Eppink and Parker in Nijmegen in 1997. In this technique an electrostatic lens guides all ions with the same initial velocity and charge/mass ratio to the same point on the detector, irrespective of their initial distance from the lens-axis. When the laser polarization direction is chosen parallel to the vertical axis of the detector screen, the inverse Abel transformation[17] can be used to reconstruct the original three-dimensional (3D) velocity distribution from the two-dimensional (2D) ion image. The measured angular distribution of the ions differs from the photofragment atomic angular distribution, because the REMPI process uses polarized light. Because of this polarization, the ionization efficiency of the atoms depends on their angular distribution and polarization, and on the geometrical setup of the experiment. Using angular momentum theory the atomic fragment angular distribution and polarization can be recalculated from the measured ion angular distribution, as we will show in Chapter 3.

The photodissociation of O_2 in the Herzberg continuum is a fast dissociation process ($\approx 0.1 - 0.3$ ps), which means that the dissociation occurs on a smaller timescale than rotation, and that the axial recoil approximation can be used. Excitation into the Herzberg continuum is of mixed parallel/perpendicular character, due to the forbidden nature of the transitions and the multitude of participating intermediate states. Therefore the angular distribution is a linear combination of the pure $\sin^2\theta$ and $\cos^2\theta$ distributions, with a β somewhere between -1 and 2. In the velocity map ion-imaging experiment of Buijsse *et al.*[7] a pulsed molecular beam of cold (≈ 10 K) O_2 in helium is crossed at right angles by one or two counterpropagating pulsed focussed laser beams. The first (variable wavelength) laser excites ground state O_2 into the Herzberg continuum. The second laser ionizes the nascent $O(^3P_j)$ atoms at 226 nm, the (2+1) REMPI wavelength. In this REMPI process, the $O(^3P)$ atom is ionized with three photons. The resonant intermediate state $O(2p^3(^4S)3p^3P)$ is reached with 2 photons. Dissociation at 226 nm can be studied in a one-laser experiment, in which the same laser is used for both excitation and detection. A raw and Abel inverted ion-image for dissociation of O_2 at 225.67 nm, and subsequent REMPI detection of $O(^3P_2)$ is shown in Fig. 1.2 (a) and (b) respectively.

The 3D velocity distribution is obtained by rotation of the inverted image [Fig. 1.2 (b)] around the vertical symmetry axis (the ϕ polar angle). This is an image from a one-laser experiment. The laser polarization $\underline{e}$ is vertical, and the laser propagation from left to right. All fragments with the same initial velocity form a ring in the inverted image, and the angle θ is given by the angle with the vertical axis of the image. The image shows three rings and a central dot. The central dot is O_2^+ signal with zero transverse kinetic energy. The inner ring is the signal that we are interested in: one-photon excitation into the Herzberg continuum and subsequent dissociation into $O(^3P_2) + O(^3P_j)$. Note that only one atom is detected, $O(^3P_2)$ in this case. The three fine-structure states $O(^3P_j)$ of the second atom give in principle rise to three rings in the ion image,

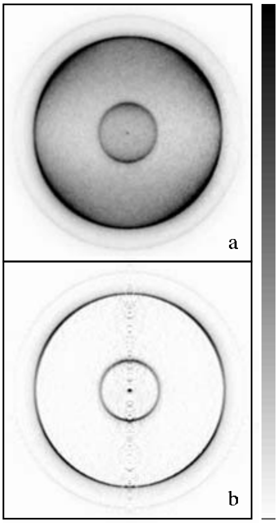

Figure 1.2: Raw (a) and Abel inverted (b) ion image for dissociation of O_2 *at 225.67 nm, and subsequent REMPI detection of* $O(^3P_2)$.

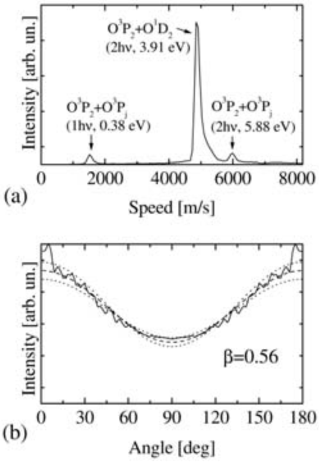

Figure 1.3: Velocity (a) and angular (b) distributions obtained from Fig. 1.2. Panel (b) shows the angular distribution for the one-photon $O(^3P_2) + O(^3P_j)$ *channel (solid line). This angular distribution is best fitted with* $\beta = 0.56$ *(dashed line), for comparison we show also dotted curves with* $\beta = 0.46$ *and* 0.66*. We thank André Eppink*[7] *for making this figure and Fig. 1.2 available to us.*

separated in kinetic energy by the O(^3P) fine-structure splittings. However, the experimental resolution is not sufficient to resolve this small kinetic energy difference. Only one ring is measured, thus summing over the three fine-structure states of the second atom. The other rings are from two-photon excitation and dissociation into O($^3P_2$) + O($^1D_2$) (middle ring) and O($^3P_2$) + O(^3P_j) (outermost ring). These last two rings show a quadrupolar angular distribution, that can be described by a fourth-order Legendre polynomial. This is indicative of the two-photon process.

Fig. 1.3 shows the velocity distribution obtained from Fig. 1.2 (b) by integration over θ and ϕ. The speed distribution shows the three rings as peaks. Branching ratios over the three fine-structure states O(^3P_j) with $j = 0, 1, 2$ were obtained by integrating the one-photon O(^3P_j) + O(^3P) peak for the three images. The fine-structure branching ratio was determined for the one-laser experiment at 226 nm only. In the two-laser experiments at other dissociation energies, the signal intensity depends on the precise overlap of the focal points of the two lasers. This overlap changes too much between the images for different j.

Fig. 1.3 (b) shows the angular distribution of the ions from the inner ring of Fig. 1.2. The data (solid line) is best fitted with a distribution with $\beta =$ 0.56 (dashed line). The β parameter describing the O(^3P_j) atoms angular distribution is not equal to this measured angular distribution of the oxygen ions. The REMPI process uses polarized laser light, with the same polarization direction as the excitation laser pulse in this experiment. Because of this polarization, the ionization efficiency of the atoms depends on their angular distribution, and on the geometrical setup of the experiment. In Chapter 3 we calculate both the angular distribution of the atoms, and the observed angular distribution of the ions. The two distributions differ most for low energies, just above the dissociation limit.

1.6 Bound state spectroscopy: energy levels and transition intensities

Light can induce transitions between RVE states in the molecule, when the states have the correct symmetry-relation with respect to each other. A transition is resonant (occurs most likely) when the energy difference between the initial and final RVE state is equal to the photon energy. The energies of the rovibrational states in the electronic ground state are well known for a time.[18, 19] The energy difference between the ground state and the Herzberg states is about 4 eV, which is in the UV range of the electromagnetic spectrum. From the UV absorption spectrum of ground state oxygen molecules, one can thus infer the energies of RVE states in the electronically excited Herzberg states. Experimental studies of the level positions of Herzberg RVE states are numerous.[2–4, 9–11, 20–24] Vibrational levels in the Herzberg states have been calculated in Chapter 2 of this thesis, and a full RVE state calculation, especially of states closely below the dissociation limit, can be found in Chapter 4.

The intensity of the transition can be measured by integration of the absorption spectrum. This intensity depends on several factors. For example, the rotational quantum number J for initial and final state may differ by at most 1. The vibrational wave functions of both states must have some overlap. The most important factor is the transition dipole moment matrix element between initial and final state electronic wave functions. The transition dipole moment between the ground state, which has $^3\Sigma_g^-$ symmetry, and the Herzberg states, of $^3\Sigma_u^+$, $^3\Delta_u$, and $^1\Sigma_u^-$ symmetries, is zero in first order. The Herzberg transitions gain intensity only after inclusion of spin-orbit and orbit-rotation interactions of ground and excited states with intermediate states of several symmetries. This results in a complicated mechanism for the excitation into the Herzberg states. This mechanism has been elucidated in Chapter 5 where we compare experimental integrated line cross-sections[9–12] with calculated results.

Bibliography

[1] M. Born and R. Oppenheimer, Ann. Physik **84**, 475 (1927).

[2] G. Herzberg, Naturwissenschaften **20**, 577 (1932).

[3] G. Herzberg, Can. J. Phys. **30**, 185 (1952).

[4] G. Herzberg, Can. J. Phys. **31**, 657 (1953).

[5] R. P. Saxon and B. Liu, J. Chem. Phys. **67**, 5432 (1977).

[6] H. Partridge, C. W. Bauschlicher, Jr., S. R. Langhoff, and P. R. Taylor, J. Chem. Phys. **95**, 8292 (1991).

[7] B. Buijsse, W. J. van der Zande, A. T. J. B. Eppink, D. H. Parker, B. R. Lewis, and S. T. Gibson, J. Chem. Phys. **108**, 7229 (1998).

[8] R. Klotz and S. D. Peyerimhoff, Mol. Phys. **57**, 573 (1986).

[9] K. Yoshino, J. R. Esmond, J. E. Murray, W. H. Parkinson, A. P. Thorne, R. C. M. Learner, and G. Cox, J. Chem. Phys. **103**, 1243 (1995).

[10] K. Yoshino, J. R. Esmond, W. H. Parkinson, A. P. Thorne, R. C. M. Learner, and G. Cox, J. Chem. Phys. **111**, 2960 (1999).

[11] K. Yoshino, J. R. Esmond, W. H. Parkinson, A. P. Thorne, R. C. M. Learner, G. Cox, and A. S.-C. Cheung, J. Chem. Phys. **112**, 9791 (2000).

[12] M.-F. Mérienne, A. Jenouvrier, B. Coquart, M. Carleer, S. Fally, R. Colin, A. C. Vandaele, and C. Hermans, J. Mol. Spectrosc. **202**, 171 (2000).

[13] R. N. Zare, *Angular momentum*, Wiley, New York, 1988.

[14] A. R. J. Heck and D. W. Chandler, Annu. Rev. Phys. Chem. **46**, 335 (1995).

[15] A. T. J. B. Eppink and D. H. Parker, Rev. Sci. Instrum. **68**, 3477 (1997).

[16] D. H. Parker and A. T. J. B. Eppink, J. Chem. Phys. **107**, 2357 (1997).

[17] C. J. Dash, Applied Optics **31**, 1146 (1992).

[18] G. Herzberg, *Molecular Spectra and Molecular Structure*, volume I – Spectra of Diatomic Molecules, Krieger, Malabar Florida, 2nd edition, 1950.

[19] P. H. Krupenie, J. Phys. Chem. Ref. Data **1**, 423 (1972).

[20] D. A. Ramsay, Can. J. Phys. **64**, 717 (1986).

[21] P. M. Borrell, P. Borrell, and D. A. Ramsay, Can. J. Phys. **64**, 721 (1986).

[22] B. Coquart and D. A. Ramsay, Can. J. Phys. **64**, 726 (1986).

[23] T. G. Slanger and P. C. Cosby, J. Phys. Chem. **92**, 267 (1988).

[24] A. Jenouvrier, M.-F. Mérienne, B. Coquart, M. Carleer, S. Fally, A. C. Vandaele, C. Hermans, and R. Colin, J. Mol. Spectrosc. **198**, 136 (1999).

Chapter 2

Photodissociation of O_2 *in the Herzberg continuum. I. Ab initio calculation of potential energy curves and properties*

Abstract

We present *ab initio* complete active space self-consistent-field plus multireference configuration interaction (CASSCF + MRCI) potential energy curves for the eight electronically excited ungerade states of oxygen ($A^3\Sigma_u^+$, $c^1\Sigma_u^-$, $A'\ ^3\Delta_u$, $^1\Pi_u$, $^3\Pi_u$, $^5\Pi_u$, $^5\Sigma_u^-$, and $2^3\Sigma_u^+$) that correlate with the $O(^3P)$ + $O(^3P)$ dissociation limit. We also report the R-dependent spin-orbit couplings between these states and the R-dependent radial derivative coupling matrix element $\langle 2^3\Sigma_u^+|\partial/\partial R|\ A^3\Sigma_u^+\rangle$. The near degeneracy in the long range of the same-symmetry states $2^3\Sigma_u^+$ and $A^3\Sigma_u^+$ may result in unphysical mixing of these states in a CASSCF calculation. We derive the correct asymptotic behavior of these states as dictated by the quadrupole-quadrupole interaction and we show how a correct long range description of these states can be achieved numerically by employing undistorted molecular orbitals. Bound state calculations using Herzberg I, II, and III potentials show excellent agreement with all available spectroscopic data. In the accompanying paper the potentials and couplings will be employed in a semiclassical study of the photodissociation of O_2 in the Herzberg continuum.

2.1 *Introduction*

The first step in the formation of ozone (O_3) in the atmosphere is the photodissociation of O_2.[1] Dissociation of ground state $O_2(X^3\Sigma_g^-)$ occurs in the Herzberg continuum (200–240 nm) via transitions to the $A^3\Sigma_u^+$, $c^1\Sigma_u^-$, and

$A'\,^3\Delta_u$ states (the so-called Herzberg I, II, and III transitions). These three transitions are electric dipole forbidden and the photoabsorption cross sections are several orders of magnitude smaller than, e.g., the cross section in the Schumann-Runge continuum (below 176 nm) which arises from an allowed transition. Since the Herzberg continuum is very weak it allows sunlight to penetrate deep into the atmosphere where the O_2 concentration is large. As a result, the Herzberg transitions lead to 90 % of the photodissociation of O_2 in the lower stratosphere and give rise to the Chapman ozone layer.[2,3]

In 1998 Buijsse *et al.*[4] constructed a photoabsorption model based on the latest experimental and theoretical knowledge of the Herzberg system. This model relies to a large extent on extrapolation of spectroscopic data for the Herzberg I, II, and III bands. These bands occur because the three electronically excited states are weakly bound. Note that in recent years several experimental studies re-investigated these bands.[5–10] The Herzberg transitions borrow intensity from electric dipole allowed transitions, mainly through spin-orbit (SO) interactions in electronic ground and excited states. The Herzberg I transitions give the largest contribution to the Herzberg continuum. The dominant channels involve the $A^3\Sigma^+_{u,\pm1}$ state (± 73 % at $\lambda = 226$ nm),

$$X^3\Sigma^-_{g,\pm1} \xrightarrow{||} B^3\Sigma^-_{u,\pm1} \xleftrightarrow{\mathrm{SO}} A^3\Sigma^+_{u,\pm1}$$
$$X^3\Sigma^-_{g,0^+} \xleftrightarrow{\mathrm{SO}} 1^3\Pi_{g,0^+} \xrightarrow{\perp} A^3\Sigma^+_{u,\pm1}$$

and the $A^3\Sigma^+_{u,0^-}$ state (± 19 % at $\lambda = 226$ nm)

$$X^3\Sigma^-_{g,\pm1} \xleftrightarrow{\mathrm{SO}} 1^3\Pi_{g,\pm1} \xrightarrow{\perp} A^3\Sigma^+_{u,0^-},$$

where the symbols $||$ and $\perp$ refer to the parallel and perpendicular components of the dipole operator. The other transitions contributing to the Herzberg continuum are all perpendicular. A one-photon transition gives rise to an angular distribution of the photofragments $P(\theta) = 1 + \beta P_2(\cos\theta)$, where θ is the angle between the laser polarization and the fragment recoil direction and P_2 is the second order Legendre polynomial. In the sudden recoil limit the anisotropy parameter β equals 2 for a parallel transition and -1 for a perpendicular transition. Thus, Buijsse *et al.* could validate their photoabsorption model by determining the overall β parameter in an ion imaging experiment.

In this experiment[4] the atomic fragments were detected by (2+1) REMPI yielding $O(^3P_{j=2,1,0})$ fine-structure resolved, energy dependent anisotropy parameters $\beta_j(E)$. In the adiabatic (low energy) limit all the electronically excited states involved correlate with the $O(^3P_2)$ + $O(^3P_2)$ limit. However, in the experiment $j = 1$ and $j = 0$ atomic fragments were found and furthermore the β_j parameters were different for $j = 2$, 1, and 0. This suggests that initially excited states with different parallel/perpendicular character such as $A^3\Sigma^+_{u,\pm1}$ ($\beta \approx 1.23$) and $A^3\Sigma^+_{u,0^-}$ ($\beta = -1$) have different atomic fine-structure branching ratios. These branching ratios are determined by transitions that occur, as we will show, at interatomic distances between $R_{\text{O–O}} = 4.5$ and 9 a_0 where the separations between the potential energy curves correlating with the $O(^3P)$ + $O(^3P)$ limit are of the same order as the spin-orbit couplings (≈ 1 mE_h). Thus the experimental results contain information about potentials and couplings in a region that is difficult to probe with spectroscopic techniques. In this paper we present *ab initio* calculations of the potentials and couplings for all eight ungerade states that correlate with the $O(^3P)$ + $O(^3P)$ limit. The results are used in a dynamical calculation described in the accompanying paper,[11] where we compare calculated and measured $\beta_j(E)$ parameters.

In the experiment O_2 was prepared in a cold molecular beam, where the population of the ground state ($N = 1$) was estimated to be at least 75%. Hence, we have ignored rotational couplings. We found, however, that in addition to the spin-orbit couplings, also the radial nonadiabatic coupling proportional to the nonadiabatic coupling matrix element (NACME) $\langle 2^3\Sigma_u^+|\partial/\partial R$ $|A^3\Sigma_u^+\rangle$, which arises from the nonseparability of electronic and nuclear motion, becomes important between 4 and 8 a_0. The six ungerade states not involved in this coupling matrix element are all of different $D_{\infty h}$ symmetry, so all other radial derivative couplings are zero.

We will show that in the strong interaction region the CASSCF+MRCI method described in detail in Sec. 2.3 gives very good results by comparing (in Sec. 2.5) calculated vibrational energy levels and rotational constants with spectroscopic data available for the Herzberg bands. However, this method gives convergence problems in the long range (see Sec. 2.3). Furthermore, when the $A^3\Sigma_u^+$ and $2^3\Sigma_u^+$ states become nearly degenerate in the long range, they do not approach the correct atomic limit defined in Sec. 2.2, but some (arbitrary) linear combination. This results in spin-orbit couplings not going to their analytically known long range values. Therefore we present an alternative procedure for obtaining molecular orbitals in the long range, also in Sec. 2.3. In contrast to the CASSCF based calculations, this procedure gives the correct long range limit for the spin-orbit couplings. In Sec. 2.2 we derive this long range limit using the atomic spin-orbit coupling constant and angular momentum theory. We present the derivation in some detail because we will need the analytic description of the long range behavior of the electronic wave functions when we employ the *ab initio* results in the dynamical calculation in the accompanying paper.[11] In particular the relative signs of the couplings must be consistent. In Sec. 2.4 we present fits of the potential curves that smoothly connect short range and long range results, and have the correct asymptotic behavior. We also present fits for the NACME and spin-orbit couplings. We will end with some conclusions in Sec. 2.6. Throughout this paper we employ atomic units. Note that 1 mE_h = 219.474 63 cm^{-1}.

2.2 Theory

2.2.1 Potential Energy Curves

To describe the photodissociation of O_2, we calculated potential energy curves for all ungerade electronic states dissociating into two $O(^3P)$ atoms. Further we computed nonadiabatic and spin-orbit couplings between these states. The total Hamiltonian is given by

$$\hat{H}(R) = \hat{H}_{\mathrm{coul}}(R) + \hat{H}_{\mathrm{SO}}(R), \tag{2.1}$$

where $\hat{H}_{\mathrm{coul}}(R)$ is the usual time independent Coulombic Hamiltonian in the clamped nuclei approximation, $\hat{H}_{\mathrm{SO}}(R)$ is the spin-orbit interaction, and R is the internuclear distance. The potential energy curves $\epsilon_{c|\Lambda|S}(R)$ and the corresponding electronic adiabatic Born-Oppenheimer (ABO) wave functions are defined by

$$[\hat{H}_{\mathrm{coul}}(R) - \epsilon_{c|\Lambda|S}(R)]|c\Lambda S\Sigma; R\rangle = 0, \tag{2.2}$$

where Λ, S, and Σ are the usual Hund's case (a) quantum numbers. The index c distinguishes between states that belong to the same irreducible representation of $D_{\infty h}$ and have the same spin part. All the electronically excited states that are relevant to our problem are ungerade and we omit this symmetry label. Upon dissociation into two Russell-Saunders coupled atoms the ABO wave functions can be expanded in products of atomic wave functions $|l_a\lambda_a\rangle|s_a\sigma_a\rangle|l_b\lambda_b\rangle|s_b\sigma_b\rangle$, or in coupled atomic states

$$|L\Lambda S\Sigma\rangle = |L\Lambda\rangle|S\Sigma\rangle, \tag{2.3}$$

with

$$\begin{aligned} |L\Lambda\rangle &= \sum_{\lambda_a\lambda_b} |l_a\lambda_a\rangle|l_b\lambda_b\rangle\langle l_a\lambda_a l_b\lambda_b|L\Lambda\rangle, \\ |S\Sigma\rangle &= \sum_{\sigma_a\sigma_b} |s_a\sigma_a\rangle|s_b\sigma_b\rangle\langle s_a\sigma_a s_b\sigma_b|S\Sigma\rangle, \end{aligned} \tag{2.4}$$

where a and b label the atoms, for $O(^3P)$ $l_a = l_b = s_a = s_b = 1$, and $\lambda_a, \lambda_b, \sigma_a$, and σ_b are the projections of the atomic angular momenta on the internuclear axis. The symbol $\langle a\alpha b\beta|c\gamma\rangle$ is a Clebsch-Gordan coefficient. The coupling of l_a and l_b to L is not strictly necessary, but very convenient, since the ABO states will turn out to correlate in the long range one-to-one with these coupled atomic states.

If, for a given spin state and Λ quantum number, only one coupled atomic state $|L\Lambda S\Sigma\rangle$ exists it must correlate in the long range to an ABO state on symmetry grounds. Otherwise, we may construct long range ABO states by considering the leading interatomic term of the multipole expansion of $\hat{H}_{\mathrm{coul}}$ at large internuclear distance.[12] To find its matrix elements we write the interatomic potential part $\hat{V}$ of $\hat{H}_{\text{coul}}$ as a multipole expansion in spherical tensor form.[13] With $K \equiv l_1 + l_2$ we have

$$\hat{V} = \sum_{l_1 l_2} \frac{(-1)^{l_2}}{R^{K+1}} \left[\frac{(2K)!}{(2l_1)!(2l_2)!} \right]^{1/2} \hat{T}_K \equiv \sum_K \hat{V}_K, \tag{2.5}$$

with

$$\hat{T}_K = \sum_{m_1 m_2} \hat{Q}^{(a)}_{l_1 m_1} \hat{Q}^{(b)}_{l_2 m_2} \langle l_1 m_1 l_2 m_2 | K0 \rangle, \tag{2.6}$$

where we assumed the molecule to lie along the z-axis. The Wigner-Eckart theorem relates the matrix elements of the atomic multipole operator $\hat{Q}^{(a)}_{l_1 m_1}$ to the reduced matrix element $\langle l_a || \hat{Q}^{(a)}_{l_1} || l'_a \rangle$,

$$\langle l_a m_a | \hat{Q}^{(a)}_{l_1 m_1} | l'_a m'_a \rangle = (-1)^{l_a - m_a} \begin{pmatrix} l_a & l_1 & l'_a \\ -m_a & m_1 & m'_a \end{pmatrix} \langle l_a || \hat{Q}^{(a)}_{l_1} || l'_a \rangle, \tag{2.7}$$

and similarly for atom b. We may also apply the Wigner-Eckart theorem to the coupled spherical tensor $\hat{T}_K$. Using the expression for its reduced matrix element (see, e.g. Eq. 5.68 in Ref. 14) we find

$$\begin{aligned} \langle (l_a l_b) L \Lambda | \hat{T}_K | (l'_a l'_b) L' \Lambda' \rangle &= (-1)^{2K + L' - \Lambda'} \langle L \Lambda L', -\Lambda' | K0 \rangle \\ &\times \begin{Bmatrix} l_a & l'_a & l_1 \\ l_b & l'_b & l_2 \\ L & L' & K \end{Bmatrix} \sqrt{(2L+1)(2L'+1)} \langle l_a || \hat{Q}^{(a)}_{l_1} || l'_a \rangle \langle l_b || \hat{Q}^{(b)}_{l_2} || l'_b \rangle. \end{aligned} \tag{2.8}$$

The only permanent multipole moment of an O(^3P) atom is the quadrupole. The leading term of the interatomic potential is thus the quadrupole-quadrupole interaction $\hat{V}_5$, with $l_1 = l_2 = 2$ and $K = 4$. The $\hat{V}_5$ matrix elements are given by

$$\langle L \Lambda S \Sigma | \hat{V}_5 | L' \Lambda' S \Sigma \rangle = R^{-5} \delta_{L,L'} \delta_{\Lambda,\Lambda'} \frac{3}{2} \sqrt{70} Q_{zz}^2 (-1)^{L-\Lambda} \langle L \Lambda L, -\Lambda | 40 \rangle, \tag{2.9}$$

where we define the quadrupole moment of O(^3P) as

$$Q_{zz} \equiv \langle 10 | \hat{Q}_{2,0} | 10 \rangle = -\sqrt{\frac{2}{15}} \langle 1 || \hat{Q}_2 || 1 \rangle. \tag{2.10}$$

Thus it turns out that the coupled atomic states correspond to long range ABO states, because the off-diagonal elements of V_5 are zero. Therefore we will drop the label c and instead use the notation $|(L)\Lambda S \Sigma; R\rangle$ for the ABO state computed at an interatomic distance R that correlates with $|L \Lambda S \Sigma\rangle$. In Table 2.1 we give for all ABO states relevant to our problem the usual spectroscopic notation, the corresponding quantum numbers L, $|\Lambda|$, and S, and

Table 2.1: The labeling and the correlation with the coupled atomic states of the O_2 ungerade excited states. The coefficient c_0 denotes the fraction of $\lambda = 0$ atomic substates in the coupled atomic state, which is used in the BSSE correction, see Eqs. (2.17) and (2.18).

State	D_{2h}	$\|L\|\Lambda\|S\rangle$	c_0
$A^3\Sigma_u^+$	$B_{1u}(x)$	$\|001\rangle$	1/3
$2^3\Sigma_u^+$	$B_{1u}(x)$	$\|201\rangle$	2/3
$c^1\Sigma_u^-$	$A_u(y)$	$\|100\rangle$	0
$^5\Sigma_u^-$	$A_u(y)$	$\|102\rangle$	0
$^1\Pi_u$	$B_{2u}(y)$ $B_{3u}(x)$	$\|110\rangle$	1/2
$^3\Pi_u$	$B_{2u}(y)$ $B_{3u}(x)$	$\|211\rangle$	1/2
$^5\Pi_u$	$B_{2u}(y)$ $B_{3u}(x)$	$\|112\rangle$	1/2
$A'\ {}^3\Delta_u$	$A_u(y)$ $B_{1u}(x)$	$\|221\rangle$	0

the irreducible representation labels of D_{2h}, the group in which all numerical calculations were performed. The transformation between real D_{2h} adapted states and the complex spherical states $|(L)\Lambda S\Sigma; R\rangle$ is given by

$$\begin{aligned} |(L)\Lambda, x\rangle &= \frac{1}{\sqrt{2(1+\delta_{\Lambda,0})}} \left[(-1)^{\Lambda}|(L)\Lambda; R\rangle + (-1)^{L}|(L)-\Lambda; R\rangle\right] \\ |(L)\Lambda, y\rangle &= \frac{-i}{\sqrt{2(1+\delta_{\Lambda,0})}} \left[(-1)^{\Lambda}|(L)\Lambda; R\rangle - (-1)^{L}|(L)-\Lambda; R\rangle\right], \end{aligned} \tag{2.11}$$

where the spin part of the wave function $|S\Sigma\rangle$ has been omitted on both sides.

2.2.2 Spin-orbit coupling

The Breit-Pauli spin-orbit Hamiltonian $\hat{H}_{\mathrm{SO}}(R)$ is given by[15]

$$\hat{H}_{\mathrm{SO}}(R) = \frac{g\mu_B^2}{c^2}\left(\sum_{i,n}\frac{Z_n\hat{\mathbf{s}}_i\cdot\hat{\mathbf{l}}_i^{(n)}}{r_{in}^3} - \sum_{i>j}\frac{2\hat{\mathbf{s}}_i\cdot\hat{\mathbf{l}}_j^{(i)}+\hat{\mathbf{s}}_i\cdot\hat{\mathbf{l}}_i^{(j)}}{r_{ij}^3}\right). \tag{2.12}$$

In this formula the summation labels i and j indicate electrons and the label n runs over the nuclei. The symbol μ_B is the Bohr magneton, c is the speed of light, Z_n is the charge of nucleus n, $\hat{\mathbf{s}}_i$ is the spin-operator for electron i, $\hat{\mathbf{l}}_i^{(a)}$ is the orbital angular momentum of electron i with respect to particle a

(nucleus or electron), and r_{ab} is the distance between particles a and b. This Hamiltonian couples ABO states with the same value of $\Omega = \Lambda + \Sigma$. Matrix elements are nonzero for $\Delta\Omega = 0$, $\Delta\Lambda = -\Delta\Sigma = 0, \pm 1$, $\Delta S = 0, \pm 1$, $g \leftrightarrow g$, and $u \leftrightarrow u$. From the last two rules follows that we only need to consider the ungerade states, because the initial excitation is into the ungerade Herzberg system. Using the Wigner-Eckart theorem, the matrix elements of $\hat{H}_{\mathrm{SO}}(R)$ can be written as

$$\begin{aligned}\langle (L)\Lambda S\Sigma; R|\hat{H}_{\mathrm{SO}}(R)|(L')\Lambda' S'\Sigma'; R\rangle = \\ (-1)^{S-\Sigma}\begin{pmatrix} S & 1 & S' \\ -\Sigma & m & \Sigma' \end{pmatrix}\langle (L)\Lambda S; R||\hat{H}_{\mathrm{SO}}(R)||(L')\Lambda' S'; R\rangle, \quad (2.13)\end{aligned}$$

where $m = \Sigma - \Sigma'$ and the quantity between brackets is a $3j$ symbol. In the atomic region the spin-orbit coupling is given by

$$\hat{H}_{\mathrm{SO}}(\infty) = A(\hat{l}_a \cdot \hat{s}_a + \hat{l}_b \cdot \hat{s}_b), \quad (2.14)$$

where A is the atomic spin-orbit splitting constant, which has an experimental value of -0.353 mE$_h$ for O(^3P) atoms.[16] For $R \to \infty$ we may also apply the Wigner-Eckart theorem to the orbital part to find an explicit expression for the reduced matrix element in Eq. (2.13),

$$\begin{aligned}\langle (L)\Lambda S; \infty||\hat{H}_{\mathrm{SO}}(\infty)||(L')\Lambda' S'; \infty\rangle = 3A(-1)^{m+L-\Lambda}\begin{pmatrix} L & 1 & L' \\ -\Lambda & -m & \Lambda' \end{pmatrix} \\ \times \left[R(s_a, s_b, S, S')R(l_a, l_b, L, L') + R(s_b, s_a, S, S')R(l_b, l_a, L, L')\right], \quad (2.15)\end{aligned}$$

where the function $R(x_a, x_b, X, X')$ is given in terms of a $6j$ symbol by

$$\begin{aligned}R(x_a, x_b, X, X') = \\ \left[(2X+1)(2X'+1)x_a(x_a+1)\right]^{\frac{1}{2}}(-1)^{x_a+x_b+X'}\begin{Bmatrix} x_a & x_a & 1 \\ X & X' & x_b \end{Bmatrix}. \quad (2.16)\end{aligned}$$

Equation (2.15) can be used to illustrate one of the problems encountered in the long range with the standard CASSCF (+MRCI) method to calculate optimized MOs, properties and molecular energies (see Sec. 2.3). If the wave functions for $A^3\Sigma_u^+$ and $2^3\Sigma_u^+$ do not converge to the correct atomic limits (with $L = 0$ and $L = 2$, respectively), but to an arbitrary linear combination, then the reduced matrix elements calculated on basis of these mixed wave functions will also tend to a linear combination of the values in the correct atomic limit.

2.3 Calculations

2.3.1 Potential Energy Curves

All calculations were performed with the MOLPRO[17] package. In the short range ($R < 6$ a$_0$) we use the augmented correlation consistent polarized valence quintuple zeta (aug-cc-pV5Z) one-electron basis set.[18] The orbitals were optimized with the CASSCF[19,20] method. In the calculations we employ D_{2h} symmetry, but $D_{\infty h}$ symmetry is imposed on the orbitals, using the LQUANT option. The states $A'\ ^3\Delta_u$, $A^3\Sigma_u^+$, and $2^3\Sigma_u^+$ appear all in the same B_{1u} irrep of D_{2h} (in this energy ordering at equilibrium geometry). The orbitals for $2^3\Sigma_u^+$ are obtained in a state averaged calculation together with the $A^3\Sigma_u^+$ and $A'\ ^3\Delta_u$ states. The orbitals for $A^3\Sigma_u^+$ and $A'\ ^3\Delta_u$ are optimized in a state averaged calculation of only those two states. All other states are lowest in their symmetry and are optimized independently. The active space consists of all $2s$ and $2p$ valence orbitals and three extra bonding $[\sigma_g,\ \pi_u(x,y)]$ orbitals. The $1s$ core orbitals were fully optimized but kept doubly occupied.

The orbitals were used in an internally contracted multireference configuration interaction (MRCI)[21,22] calculation with single and double excitations. All configurations that contribute more than 1 % to the CASSCF wave function are used as reference configurations in the MRCI calculation. The energies of the $A^3\Sigma_u^+$ and $A'\ ^3\Delta_u$ states are calculated in a single calculation, optimizing both states simultaneously. The energy of the $2^3\Sigma_u^+$ state is obtained by optimizing only the third B_{1u} state. We applied the Pople size consistency correction.[23] As we will show in Sec. 2.5 this method gives excellent results for the short range part of the potential.

However, for $R > 6$ a$_0$ we encountered three problems with this method.

1. Convergence problems occurred in the CASSCF calculations in some cases.

2. The reference configuration selection mechanism in the MRCI calculation results in discontinuities in the potential curves. The jumps are quite small ($\sim 200\mu\mathrm{E}_h$), which is fully acceptable in the short range. In the long range, however, such jumps are not negligible compared to the interaction energies.

3. The $A^3\Sigma_u^+$ and $2^3\Sigma_u^+$ state did not converge to the correct atomic limit. For example, the analysis in Sec. 2.2 shows that the SO coupling between $A^3\Sigma_u^+$ and $^3\Pi_u$ should vanish for large R, whereas the reduced matrix element for the SO coupling between $2^3\Sigma_u^+$ and $^3\Pi_u$ should be $\frac{3}{2}\sqrt{2}A$. However, at the CASSCF level these couplings are both nonzero (see Sec. 2.5) suggesting that the computed states are linear combinations of the $A^3\Sigma_u^+$ and $2^3\Sigma_u^+$ states. This is of course not too surprising, since these states are of the same symmetry, and nearly degenerate for large R.

To circumvent these problems we employed a somewhat different approach for the long range calculations. For these calculations, we constructed molecular orbitals as fixed linear combinations of atomic orbitals. For instance, a $2p\pi_x$ orbital was constructed as $2p_x(A) + 2p_x(B)$, etc. The atomic orbitals were determined in a separate state averaged CASSCF calculation of the three O(^3P) states, which yields spherical symmetry adapted atomic orbitals. The active space in these calculations consisted of the $2s$ and $2p$ orbitals. In order to use the MOs in an MRCI calculation they were orthogonalized, but not optimized. First, core orbitals were constructed from atomic $1s$ orbitals. Then, the "active" space was constructed by projecting the core component out of the $2s/2p$ valence space. The virtual space was constructed as the orthogonal complement of the core and valence spaces. Within each orbital space orthonormal bases were obtained with Löwdin orthogonalization. In the MRCI calculation we used the complete active space as reference space, thus avoiding the discontinuities arising from configuration selection. In Sec. 2.5 we will demonstrate that these undistorted molecular orbital based calculations yield the correct atomic limit for the SO couplings. For these undistorted "long range" calculations we used a slightly smaller one-electron basis than for the short range. It consists of the $(13s8p)$ primitive set of van Duijneveldt,[24] which was contracted to $[5s4p]$ using the default MOLPRO contraction.[25] The primitive set was supplemented with a $(6d4f2g)$ even-tempered set of polarization functions with exponents of the form $\alpha = 2.5^n\alpha_0$ with $\alpha_0 = 0.13$, 0.29, and 1.24 for the d, f, and g functions respectively and $n = 0, \ldots, k-1$ where k is the number of functions of in the set. These polarization functions were contracted to $[3d2f1g]$, again with the standard MOLPRO contraction. Finally a diffuse $s(\alpha = 0.076666)$ and $p(\alpha = 0.051556)$ orbital and the outermost $d(\alpha = 0.13)$ orbital were added uncontracted.

2.3.2 Basis set superposition error

Extensive literature on van der Waals interactions shows that the Boys-Bernardi[26] counterpoise procedure is an effective method to reduce the basis set superposition error (BSSE).[27] Van Mourik *et al.*[28] showed that for chemically bound diatomic molecules BSSE correction may improve the convergence behavior of molecular properties with basis set size, but that the corrected results are not necessarily in better agreement with the complete basis set limit than the uncorrected results. Hence, for the short range we minimized the BSSE by using a rather large one-electron basis. In the long range we used a BSSE correction. Note, however, that strictly speaking the Boys-Bernardi counterpoise procedure is not defined for a molecule dissociating into open-shell fragments. An ambiguity arises when the O(^3P) atom is calculated in the molecular basis, because the cylinder symmetry of the molecular basis breaks the spherical symmetry of the atom. Specifically, the O(^3P) states split into $\lambda = 0$ and $|\lambda| = 1$ states, where λ is the projection of the electronic orbital angular momentum on the internuclear axis. Fortunately, in the long range we can estimate the contributions from the atomic substates to the molecular wave functions using Eqs. (2.3) and (2.4). Thus, we generalized the Boys-Bernardi counterpoise procedure by defining the atomic energy for a given molecular state as the weighted average of the atomic substates, i.e.,

$$\Delta E_a(R) = c_0 \Delta E_{\lambda=0}(R) + (1 - c_0)\Delta E_{|\lambda|=1}(R), \tag{2.17}$$

with, for a molecular state $|L\Lambda S\Sigma\rangle$,

$$c_0 = \sum_{\lambda_b} |\langle l_a 0 l_b \lambda_b | L\Lambda\rangle|^2 \tag{2.18}$$

and similarly for E_b. The value of c_0 is listed for all molecular states in Table 2.1.

2.3.3 Couplings

We calculated the radial derivative couplings $\langle 2^3\Sigma_u^+|\partial/\partial R|A^3\Sigma_u^+\rangle$ with the two-point finite difference method ($\Delta R = 0.1$ a$_0$) as implemented in MOLPRO at the CASSCF as well as the CASSCF+MRCI level, and we repeated both calculations, using undistorted MOs. In these calculations we used the complete $2s/2p$ active space, and we employed the augmented Duijneveldt basis described above. In Sec. 2.5 we will argue that the results based on the undistorted long range method are to be preferred.

The spin-orbit matrix elements were calculated at the CASSCF level, taking into account both one- and two-electron integrals of the Breit-Pauli operator. Again the active space consisted of the $2s/2p$ orbitals. These calculations were also repeated using the long range method. As the one-electron basis we used the uncontracted ($12s6p3d$) primitive Gaussians from the cc-pVQZ basis,[18] since the spin-orbit integral routines implemented in MOLPRO cannot handle contracted bases. A test calculation with the *s, p, d,* and *f* orbitals of the aug-cc-pV5Z basis resulted in a change of about 1 %. The spin-orbit matrix elements being related by the Wigner Eckart theorem [Eq. (2.13)], we only calculated the 21 independent reduced matrix elements listed below. Since the electronic wave functions were calculated separately at each geometry, the signs of the reduced matrix elements were not consistent between the different geometries. The signs were adapted so that all reduced matrix elements had smooth curves as function of R, and the same sign for $R = 10.9$ a$_0$ as in the atomic approximation given by Eq. (2.15).

2.4 Analytic fit of potentials and couplings

2.4.1 Potential energy curves

Since we employ different methods in the short range and long range parts of the potential we must determine a relative energy shift of the two sets of *ab initio* points before we can fit the potential. The slopes of the potentials in the region where the data sets overlap do not match perfectly. Therefore, instead of matching the potentials in a single point, we leave a small gap between the short range and long range data sets and determine the relative shift by treating it as a free parameter in the fit. In this way we obtain a smooth fit. We use the functional form

$$V(R) = V_{\mathrm{SR}}(R) + V_{\mathrm{LR}}(R), \tag{2.19}$$

with

$$V_{\mathrm{SR}}(R) = \sum_{n=0}^{n_{\mathrm{max}}} \sum_{m=1}^{2} c_{n,m} y^n e^{-m\alpha y}, \tag{2.20}$$

where we introduced a shift $y = R - 2.8$ for numerical reasons. Furthermore,

$$V_{\mathrm{LR}}(R) = \sum_{n=5,6,8,10} \frac{C_n^{(\mathrm{LR})}}{R^n} f_n(\beta R) + V_\infty, \tag{2.21}$$

where $C_5^{(\mathrm{LR})}$ accounts for the electrostatic quadrupole-quadrupole long range part of the potential and $C_6^{(\mathrm{LR})}$, $C_8^{(\mathrm{LR})}$, and $C_{10}^{(\mathrm{LR})}$ for dispersion. The functions f_n are Tang-Toennies damping functions[29]

$$f_n(x) = 1 - e^{-x} \sum_{k=0}^{n} \frac{x^k}{k!}. \tag{2.22}$$

We take $C_5^{(\mathrm{LR})}$ from Eq. (2.9), using the quadrupole moment of $\mathrm{O}(^3P)$ of $Q_{zz} = -0.94464$ a.u. This quadrupole moment was calculated with MOLPRO, using a fourth-order finite field calculation (at field values $\pm 2.5 \times 10^{-4}$ and $\pm 5 \times 10^{-4}$ a.u.) with the partially spin-restricted open-shell single and double excitation coupled cluster method[30, 31] with perturbative triples[32] [RCCSD(T)], employing a sextuple zeta (aug-cc-pV6Z)[33] basis set. We fix the long range coefficient $C_6^{(\mathrm{LR})}$ to the values listed for the various states by Dalgarno *et al.*[34]. Note that the Q_{zz} value of –0.788 used in that paper is about 19 % smaller than ours. That value was apparently calculated at the Hartree-Fock level. The long range coefficients $C_8^{(\mathrm{LR})}$ and $C_{10}^{(\mathrm{LR})}$ and V_∞ are determined in a linear least squares fit of $V_{\mathrm{LR}}(R)$ to the *ab initio* points in range 3 (given in Table 2.2), with the damping function set to 1. A weighting of R^8 was used in this fit. After the long range parameters and V_∞ were determined in this way, all other parameters ($c_{n,m}, \alpha, \beta$, and the relative energy shift) are found in a nonlinear least squares fit, with a weighting of R^3. The short range and long range data sets used in this final fit are given as range 1 and 2 in Table 2.2, which also specifies the values of n_{max}. The asymptotic value of the potentials is made equal by setting $V_\infty = 0$ for all states. The polynomials in the exponential part of the fit cause unphysical oscillatory behavior of the fit when it is extrapolated

Table 2.2: Fit of the potential energy curves. Data points from the "short range" (Range 1) and "long range" (Range 2) calculations used in the fit, and "long range" method data points (Range 3) used in the fit of the coefficients $C_8^{(\mathrm{LR})}$ *and* $C_{10}^{(\mathrm{LR})}$*, are given as* $R_{\min} - R_{\max}$ *(in* a_0*), where all points within the interval (the given values included) with a grid spacing of 0.1* a_0 *have been used. The fit error in the short range part is given in the column headed "SR error" as the maximum absolute error for all points with* $R \leq 8.0\ \mathrm{a}_0$*. The error in the long range is given in the last column as the largest relative error in the data points with* $R > 8.0\ \mathrm{a}_0$*.*

State	Range 1	Range 2	Range 3	$n_{\max}$	SR error (μE$_h$)	LR error (%)
$c^1\Sigma_u^-$	2.2–4.5	5.5–10.0	8.0–10.6	6	40	1.2
$A'\ ^3\Delta_u$	2.3–4.5	5.5–8.0 8.7–10.6	8.4–10.6	6	34	1.6
$A^3\Sigma_u^+$	2.3–4.5	5.5–10.0	7.0–10.3	6	37	0.8
$^1\Pi_u$	3.0–5.9	7.7–10.3	8.5–10.3	5	35	0.8
$^3\Pi_u$	2.7–5.4 5.7–6.5	7.5–10.3	7.5–10.3	5	52	0.4
$^5\Pi_u$	3.0–6.0	7.5–10.3	8.0–10.3	5	23	1.1
$^5\Sigma_u^-$	2.6–5.8	7.0–10.6	8.4–10.6	6	65	1.7
$2^3\Sigma_u^+$	3.7–4.3	4.6–10.0	7.0–11.0	4	17	0.4

towards small R. To ensure physical behavior in the extrapolation we used an exponential function $C' \exp[-\alpha'(R - R'_{\mathrm{shift}})]$, where C' and α' were chosen so that the value and derivative of this exponential match with the fitted curve at the innermost data point (at R'_{shift}). Fortran routines to evaluate the potential energy curves can be downloaded from the EPAPS service.[35]

2.4.2 Nonadiabatic coupling

The nonadiabatic coupling as a function of R consists of a single, somewhat asymmetric peak. The tails of the peak appear to go to zero faster than a Lorentzian and slower than a Gaussian function. We obtained a good fit with the functional form

$$g_{2,A}(R) = \frac{C_1}{1 + C\{e^{-\alpha_1(R-R_1)} + e^{\alpha_1(R-R_1)}\}} + \frac{C_2}{1 + C\{e^{-\alpha_2(R-R_2)} + e^{\alpha_2(R-R_2)}\}}. \tag{2.23}$$

It has two linear parameters, the peak heights C_1 and C_2, and five nonlinear parameters, the peak positions R_1 and R_2, the peak width parameters α_1

and α_2, and the parameter C that influences the shape of the peak. The nonlinear least squares fit employed a weighting function of $|g_{2,A}(R)|^{-1/2}$, i.e. a higher weight when the coupling is smaller. This fit procedure results in a relative error of 0.3 % around the peak maximum. The relative error is smaller than 1 % for $R \leq 9$ a$_0$, and increases to 15 % for $R = 11.0$ a$_0$, where the coupling is only about 1 % of its maximum. To compare the magnitude of the nonadiabatic coupling with the magnitude of the spin-orbit coupling, we have to multiply the nonadiabatic coupling by the dissociation fragment velocity v, which is given by $\sqrt{2E/\mu}$, where E is the kinetic energy, and μ is the reduced mass. At the highest experimental dissociation energy ($\lambda = 204$ nm, see the accompanying paper, Chapter 3 of this thesis) we have an excess kinetic energy of 35 mE$_h$ after dissociation. This corresponds to a fragment velocity of 2.2×10^{-3} atomic units. At the maximum of the peak of the nonadiabatic coupling, this corresponds to an energy $\hbar v \ \langle 2^3\Sigma_u^+|\partial/\partial R|A^3\Sigma_u^+\rangle = -0.43$ mE$_h$, which is comparable to the spin-orbit interaction (effective spin-orbit splitting constant $A = -0.36$ mE$_h$). At internuclear distances $R > 9.0$ a$_0$, $\hbar v\langle\partial/\partial R\rangle <$ 0.03 mE$_h$, which is much smaller than the spin-orbit interaction.

2.4.3 Spin-orbit coupling

The R dependence of the spin-orbit matrix elements does not suggest a simple functional form. Therefore we used cubic spline interpolation, and exponential extrapolation. For extrapolation $R \to \infty$ we fitted a function of the form $A + B\exp[-\alpha(R - R_{\text{end}})]$ through the "long range method" data points with $10.0 \leq R \leq R_{\text{end}} = 10.9$ a$_0$. We determined α in a nonlinear optimization procedure, fitting the parameters A and B using linear least squares, with unit weights. The long range extrapolation was then shifted to pass exactly through the last data point. For inward extrapolation we fitted an exponential of the form $A' + B'\exp[2.5(R - R_{\text{start}})]$, so that the value in the first data point (R_{start}, see Sec. 2.5.2) matched the "short range method" value, and the derivative in the first data point matched the derivative of the line connecting the first two data points. The spline is defined by the extra conditions of the derivatives in the first and last data points. We used "long range method" data points for $R \geq 4.5$ a$_0$, and "short range" data points for $R \leq 4.0$ a$_0$. Fortran routines to evaluate the spin-orbit and nonadiabatic coupling are also available from EPAPS.[35]

2.5 Results and Discussion

2.5.1 Potential energy curves

In Fig. 2.1 we show the fits of the potential energy curves. In Table 2.3 we list the calculated spectroscopic constants R_e, ω_e, and D_e, together with

Table 2.3: Spectroscopic constants for the bound states. Experimental values for the Herzberg states are from Ref. 36 and the experimental values for the $^3\Pi_u$ state are from Ref. 7. Calculated literature values for the Herzberg and very weakly bound states are from Ref. 37.

	R_e (a$_0$)			ω_e (mE$_h$)			D_e (mE$_h$)		
State	Present	Expt.	Calc.	Present	Expt.	Calc.	Present	Expt.	Calc.
$A^3\Sigma_u^+$	2.8735	2.8724	2.880	3.655	3.663	3.563	30.52	30.33	29.55
$A'\ ^3\Delta_u$	2.8602	2.8592	2.867	3.732	3.713	3.590	33.29	33.20	32.38
$c^1\Sigma_u^-$	2.8693	2.8610	2.874	3.601	3.631	3.517	40.87	41.00	40.57
$^5\Sigma_u^-$	5.735		6.24	0.268			0.272		0.199
$^5\Pi_u$	6.168		6.58	0.164			0.160		0.182
$^3\Pi_u$	5.333	…[a]	5.65	0.422	0.31[b]	0.27	1.267	0.64	0.873
$^1\Pi_u$	6.876			0.089			0.095		

---

[a] A value for R_e is not given, only $r_0 = 5.84$ and $r_1 = 6.65$ a$_0$.

[b] This is not ω_e but $\Delta G_{1/2}$.

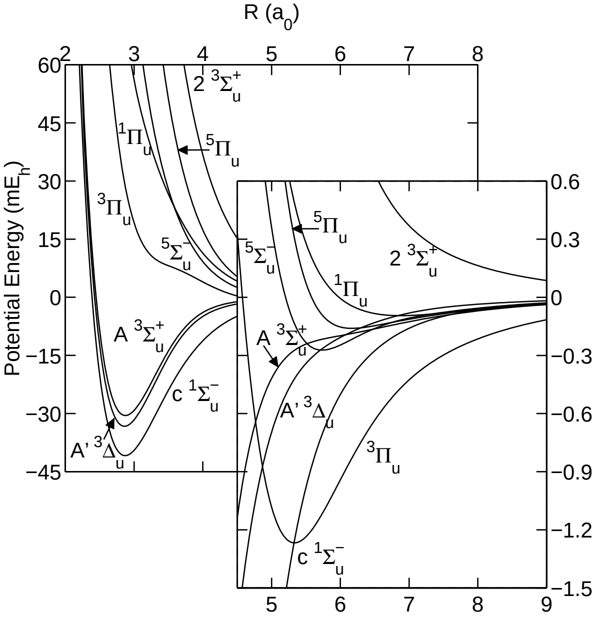

Figure 2.1: Calculated potential energy curves for the ungerade states dissociating to $\mathrm{O}(^3P) + \mathrm{O}(^3P)$*. Note that the potential axis on the right hand side* ($R \geq 4.5$) *is scaled with a factor of 50 with respect to the left hand side of the figure.*

experimental[36] and theoretical[37] literature values. For the three Herzberg states agreement of our results with experiment is excellent. For three of the four weakly bound states ($^5\Sigma_u^-, ^5\Pi_u, ^1\Pi_u$) no experimental data is available. The R_e values that we find for these states are about 0.5 a_0 shorter than the values computed by Partridge *et al.*[37] Our calculated R_e values are determined by our “short range” calculations which employ a larger one-electron basis as well as a larger number of active orbitals than the calculation by Partridge *et al.* The values that we find for the D_e of these weakly bound states in part depend on choices that were made when merging the short range and long range results.

The only spectroscopic data on the $^3\Pi_u$ state derives from its presumed role as perturber of the $A^3\Sigma_u^+$ state.[7] It seems that our values for ω_e and D_e for this state are too large, while the results of Partridge seem closer to the experimental values [Table 2.3]. However, in the region of $R \sim 5 - 7$ a_0 relevant for the observed $v = 0$ and $v = 1$ vibrational levels of the $^3\Pi_u$ state, the splittings between the ABO potentials are comparable to the spin-orbit coupling and one may not assume Hund’s case (a) states. Preliminary calculations

Table 2.4: Vibrational energies and rotational constants of all experimentally known vibrational levels of the $A^3\Sigma_u^+$ state, compared with experimental data from Ref. 7 (where available) and 36.

v	$G(v)(\mathrm{mE}_h)$	Error (%)	$B(v)(\mu\mathrm{E}_h)$	Error (%)
0	1.809	−0.31	4.114	−0.24
1	5.330	−0.26	4.032	−0.30
2	8.712	−0.25	3.947	−0.33
3	11.944	−0.25	3.857	−0.34
4	15.011	−0.26	3.758	−0.36
5	17.897	−0.29	3.647	−0.41
6	20.576	−0.34	3.520	−0.50
7	23.021	−0.43	3.371	−0.66
8	25.195	−0.54	3.190	−0.92
9	27.050	−0.68	2.964	−1.26
10	28.532	−0.82	2.669	−1.43
11	29.588	−0.83	2.281	−0.83
12	30.199	−0.41	1.720	130

that take the SO coupling into account show a much better agreement with experiment when our potentials and SO couplings are used. We will analyze this matter in more detail in a separate paper.[38]

For the Herzberg states we calculated all the vibrational energies and rotational constants with the sinc-function discrete variable representation (sinc DVR) method.[39] In Tables 2.4, 2.5, and 2.6 we compare our results with the experimental values of Jenouvrier *et al.*[7] (where available) and Slanger.[36] Almost all errors are less than 1 %. The most noticeable exceptions are the rotational constants of the highest vibrational levels, for which the errors are 1-2 orders of magnitude larger than for the other levels. This does not indicate a serious deficiency of our potentials. In fact, it can easily be understood because these energy levels are just below the dissociation limit, so that a small relative error in the vibrational energy may give a huge change in the expectation value of $\langle R^{-2}\rangle$.

In Fig. 2.2 we show the R dependence of the BSSE: $\Delta E_{\lambda=0}(R)$ and $\Delta E_{|\lambda|=1}$ (R) for the method that we used in the short range (solid lines) as well as for the method used in the long range (dashed lines). For both methods $\Delta E_{\lambda=0}(R)$ is larger than $\Delta E_{|\lambda|=1}(R)$, which is expected since the $\lambda = 0$ component of the atomic O(^3P) state has two electrons in the p_z orbital (along the internuclear axis) in the dominant configuration, compared to one for the $|\lambda| = 1$ components. Also we see that the short range calculation, which employs a larger one-electron basis gives a smaller BSSE. For the short range calculations the BSSE is about 1 % of the D_e of the Herzberg states and we did not correct

Table 2.5: As Table 2.4, for the $c^1\Sigma_u^-$ state.

v	$G(v)$(mE_h)	Error (%)	$B(v)$($\mu\mathrm{E}_h$)	Error (%)
0	1.784	−0.82	4.127	−0.55
1	5.260	−0.85	4.046	−0.74
2	8.606	−0.85	3.963	−0.58
3	11.818	−0.86	3.876	−0.59
4	14.891	−0.87	3.785	−0.60
5	17.819	−0.87	3.689	−0.61
6	20.596	−0.88	3.588	−0.63
7	23.217	−0.89	3.481	−0.64
8	25.674	−0.90	3.367	−0.63
9	27.964	−0.90	3.246	−0.66
10	30.079	−0.90	3.117	−0.63
11	32.016	−0.89	2.979	−0.58
12	33.770	−0.87	2.832	−0.48
13	35.337	−0.84	2.673	−0.34
14	36.714	−0.80	2.500	−0.21
15	37.895	−0.75	2.310	0.01
16	38.874	−0.70	2.096	0.28
17	39.645	−0.63	1.850	1.26
18	40.205	−0.51	1.567	5.45
19	40.566	−0.32	1.254	8.31

Table 2.6: As Table 2.4, for the $A'\,^3\Delta_u$ state.

v	$G(v)$(mE_h)	Error (%)	$B(v)$($\mu\mathrm{E}_h$)	Error (%)
0	1.846	0.35	4.153	−0.26
1	5.440	0.20	4.073	−0.35
2	8.895	0.09	3.990	−0.34
3	12.202	−0.01	3.902	−0.38
4	15.351	−0.08	3.806	−0.39
5	18.326	−0.15	3.701	−0.41
6	21.109	−0.22	3.582	−0.49
7	23.675	−0.31	3.445	−0.63
8	25.995	−0.43	3.284	−0.84
9	28.033	−0.57	3.091	−1.17
10	29.749	−0.74	2.852	−1.56
11	31.106	−0.89	2.562	−1.63
12	32.098	−0.93	2.224	0.47
13	32.752	−0.76	1.826	46.2

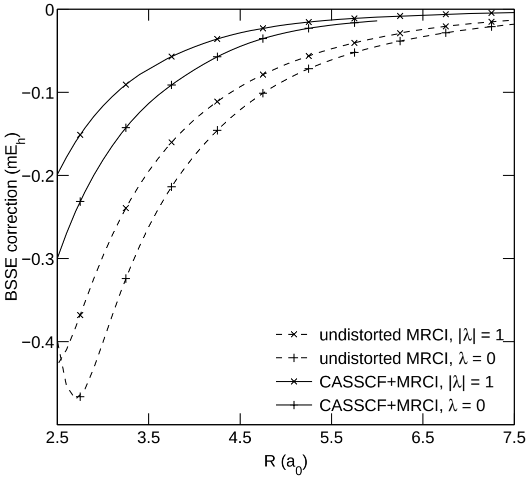

Figure 2.2: The BSSE correction for the short range CASSCF+MRCI (solid lines) and long range undistorted orbitals MRCI calculation (dashed lines). The $\lambda = 0$ (+ marks) and $\lambda = 1$ (× marks) curves refer to atomic substates of Σ and Π symmetry.

for this. Around 6 a$_0$ the BSSE for the long range calculation is in the order of 30 % of the interaction and we applied the correction given in Eq. (2.17).

2.5.2 Spin-orbit coupling

In Table 2.7 we compare the reduced spin-orbit matrix elements calculated at $R = 7.5$ a$_0$ with the undistorted orbital method and with our “short range method”. We also list the asymptotic results corresponding to $A_{\rm exp} = -0.353$ mE$_h$. Generally, there is good agreement between the two calculated values and the experimental value, except when either the $A^3\Sigma_u^+$ or the $2^3\Sigma_u^+$ state is involved. In these cases the results for the “short range method” deviate considerably. We take this as an indication that the state-averaged CASSCF method, with the choice of the active space that we used in the short range, does not properly describe the nearly degenerate $A^3\Sigma_u^+$ and $2^3\Sigma_u^+$ states in the long range. Clearly, one expects the undistorted orbital method to fail somewhere in the strong interaction region. Fortunately, there is a region—as we show in Fig. 2.3—where both methods give nearly the same SO couplings, even when the $A^3\Sigma_u^+$ or $2^3\Sigma_u^+$ states are involved. This justifies our procedure of merging short range and long range results in the fit of the SO couplings.

In Figs. 2.4 and 2.5 we plot all the fits of the reduced matrix elements. We note that there is a considerable variation of the SO couplings with R. The fine-structure energy levels of the $A'\ {}^3\Delta_{u,\Omega}$ state are given by $\epsilon_{v,\Omega} = \epsilon_{v,\Omega=2} + A_v\Lambda\Sigma$,

Table 2.7: Spin-orbit reduced matrix elements $\langle (L)|\Lambda|S;R||\hat{H}_{\mathrm{SO}}||(L')|\Lambda'|S';R\rangle$ in μE_h. Quantum numbers L, Λ, and S for bra and ket states can be found in Table 2.1. The atomic limit is calculated with the experimental splitting constant A = –353 μE_h. The calculated values are for both the calculations for R = 7.5 a_0. Ab initio *calculations were done between R_{start} and 10.9 a_0.*

Number	bra	ket	$R_{\mathrm{start}}(\mathrm{a}_0)$	Atomic	LR method	SR method
1	$^1\Pi_u$	$A'\ ^3\Delta_u$	2.2	705	725	726
2	$^1\Pi_u$	$A^3\Sigma_u^+$	2.2	−814	−815	−558
3	$^1\Pi_u$	$2^3\Sigma_u^+$	3.7	288	355	693
4	$^3\Pi_u$	$A'\ ^3\Delta_u$	2.2	611	628	629
5	$^3\Pi_u$	$A^3\Sigma_u^+$	2.2	0	−54	−405
6	$^3\Pi_u$	$2^3\Sigma_u^+$	3.6	−748	−767	−656
7	$^5\Pi_u$	$A'\ ^3\Delta_u$	1.6	−789	−811	−813
8	$^5\Pi_u$	$A^3\Sigma_u^+$	1.6	911	911	624
9	$^5\Pi_u$	$2^3\Sigma_u^+$	3.5	−322	−396	−755
10	$^3\Pi_u$	$c^1\Sigma_u^-$	1.6	499	513	514
11	$^3\Pi_u$	$^5\Sigma_u^-$	2.1	−558	−574	−575
12	$^5\Pi_u$	$^5\Sigma_u^-$	2.1	−966	−993	−995
13	$^1\Pi_u$	$^3\Pi_u$	2.2	499	513	511
14	$^3\Pi_u$	$^3\Pi_u$	2.2	−432	−444	−443
15	$^5\Pi_u$	$^3\Pi_u$	1.6	−558	−573	−572
16	$^5\Pi_u$	$^5\Pi_u$	2.2	−966	−994	−991
17	$A^3\Sigma_u^+$	$c^1\Sigma_u^-$	1.6	−814	−877	−1021
18	$2^3\Sigma_u^+$	$c^1\Sigma_u^-$	3.6	−576	−532	−64
19	$A'\ ^3\Delta_u$	$A'\ ^3\Delta_u$	1.8	−864	−889	−887
20	$A^3\Sigma_u^+$	$^5\Sigma_u^-$	2.2	911	980	1141
21	$2^3\Sigma_u^+$	$^5\Sigma_u^-$	3.8	644	594	71

where A_v is the effective spin-orbit coupling constant for vibrational level v. It is calculated as the expectation value of the R-dependent SO coupling $(1/2)\langle v|\langle (L=2)\Lambda=2, S=1, \Sigma=1; R|\hat{H}_{\mathrm{SO}}(R)|(L=2)\Lambda=2, S=1, \Sigma=1; R\rangle|v\rangle$ for the vibrational wave function of level v. Since different vibrational wave functions probe different R regions, the R dependence of the SO coupling is reflected in the variation of A_v with v. In Table 2.8 we compare the calculated constants A_v with the experimental values from Refs. 36 and 40. Generally, the deviations from the experimental values are less than 4 %. For $v = 13$ the error is somewhat larger, which is of course consistent with the error found for the rotational constant for this level. We also compared our SO couplings with all the couplings between ungerade O_2 states that were calculated by Klotz and Peyerimhoff[41] and we found that all the differences

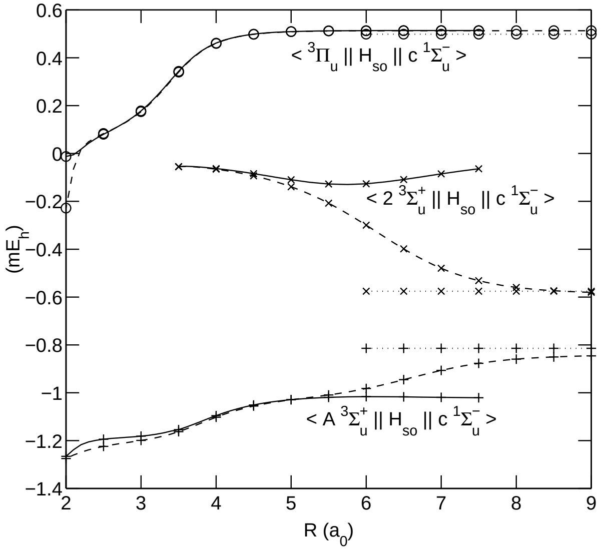

Figure 2.3: Spin-orbit matrix elements $\langle A^3\Sigma_u^+;R||\hat{H}_{\mathrm{SO}}||c^1\Sigma_u^-;R\rangle$ *(+ marks),* $\langle 2^3\Sigma_u^+;R||\hat{H}_{\mathrm{SO}}||c^1\Sigma_u^-;R\rangle$ *(× marks), and* $\langle {}^3\Pi_u;R|\hat{H}_{\mathrm{SO}}|c^1\Sigma_u^-;R\rangle$ *(○ marks), calculated with optimized (solid lines) and undistorted atomic orbitals (dashed lines), and their analytic atomic limits (dotted lines).*

are less than 15 μE$_h$.

At infinite separation, Eq. (2.15) relates all reduced spin-orbit matrix elements to a single atomic SO coupling constant A. We find that $A = -0.3627$ mE$_h$ reproduces all fitted values at infinity to within 6.4 μE$_h$, and all nonzero values within 2 %. A least squares fit of the eigenvalues of $A_{\mathrm{exp}}\hat{l}\cdot\hat{s}$ to the experimental atomic fine-structure levels[16] gives $A_{\mathrm{exp}} = -0.353$ mE$_h$. Note that the experimental energy levels do not exactly obey the Landé interval rule[42, 43] due to spin-spin (and spin-other-orbit) interactions. In particular, $E_{j=1} - E_{j=2} = 0.7222$ mE$_h$ and $E_{j=0} - E_{j=2} = 1.032$ mE$_h$, compared to $-2A_{\mathrm{exp}} = 0.706$ mE$_h$ and $-3A_{\mathrm{exp}} = 1.059$ mE$_h$. Since we do not include spin-spin interactions that cause violation of the Landé interval rule, we cannot expect agreement with experiment to better than about 3 %. In Table 2.7 we also list R_{start}, the R value of the innermost data point. For smaller R, extrapolation has been used.

2.5.3 Nonadiabatic coupling

In Fig. 2.6 we plot the nonadiabatic coupling matrix element $\langle 2^3\Sigma_u^+|\partial/\partial R\,|A^3\Sigma_u^+\rangle$, calculated at the CASSCF (solid lines) and the MRCI (dashed lines) level employing both optimized (+ marks) and undistorted (× marks) orbitals.

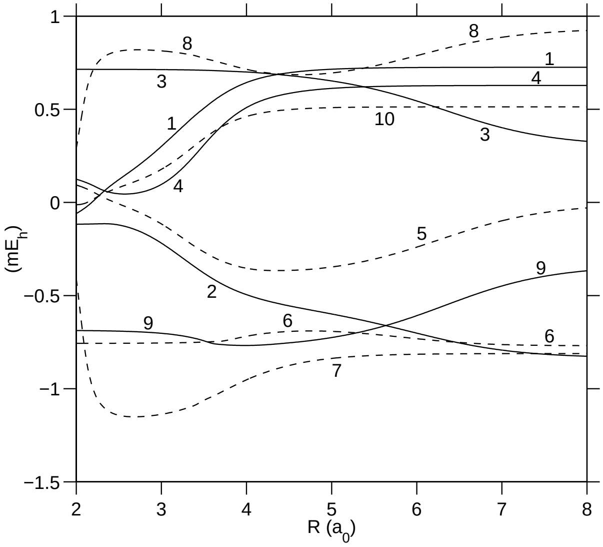

Figure 2.4: Fits of the spin-orbit reduced matrix elements, numbers 1 to 10 from Table 2.7. The different line types are only to distinguish the different matrix elements.

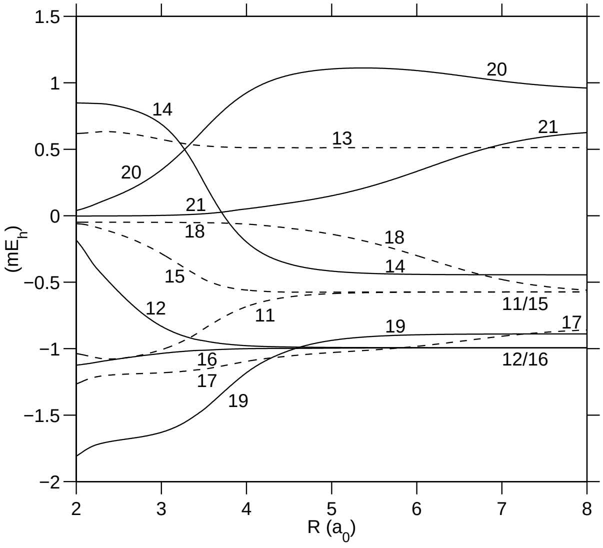

Figure 2.5: As Fig. 2.4, numbers 11 to 21.

Table 2.8: Calculated and experimental (Refs. 36 and 40) spin-orbit splitting constants (in mE_h) for the vibrational levels of $A'\,^3\Delta_u$.

v	A_v calculation	A_v experiment	Error (%)
0	−0.3363	−0.3413	−1.47
1	−0.3344	−0.3401	−1.69
2	−0.3320	−0.3397	−2.27
3	−0.3292	−0.3377	−2.52
4	−0.3257	−0.3351	−2.80
5	−0.3214	−0.3316	−3.08
6	−0.3161	−0.3271	−3.38
7	−0.3092	−0.3211	−3.72
8	−0.3004	−0.3132	−4.08
9	−0.2891	−0.3020	−4.29
10	−0.2746	−0.2860	−3.99
11	−0.2570	−0.2630	−2.31
12	−0.2371	−0.2378	−0.28
13	−0.2163	−0.178	21.5

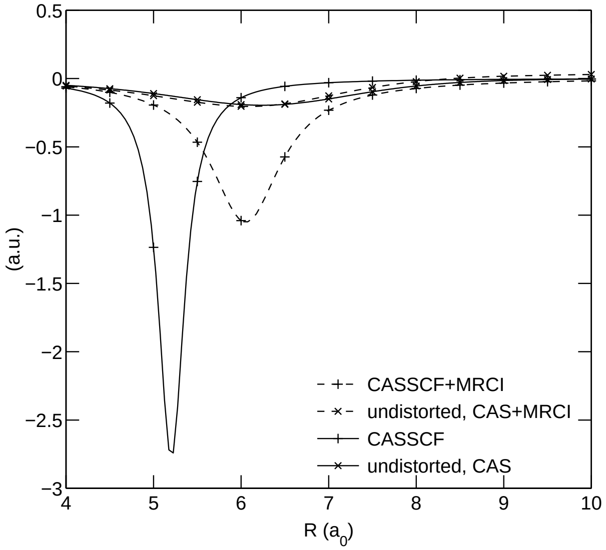

Figure 2.6: The nonadiabatic coupling matrix element $\langle 2^3\Sigma_u^+|\partial/\partial R|A^3\Sigma_u^+\rangle$, as described in Sec. 2.5.3.

We find good agreement between these results in the region $R < 4$ a$_0$ where also the SO couplings match. For the optimized orbitals we find a very large coupling of –3 a.u. at $R = 5$ a$_0$. The MRCI calculation, employing these optimized orbitals gives rather different results, which one may take again as an indication that the optimized orbitals do not provide a good description of the $A^3\Sigma_u^+$ and $2^3\Sigma_u^+$ states in this region. By contrast, for the undistorted orbitals the MRCI results are very similar to the CAS results. In the fit we used the undistorted orbital CAS results.

2.6 Conclusion

We performed high level *ab initio* calculations on the potential energy curves of several excited ungerade states of O_2: the Herzberg states $c^1\Sigma_u^-$, $A'\,^3\Delta_u$, and $A^3\Sigma_u^+$ and the repulsive states $^3\Pi_u$, $^1\Pi_u$, $^5\Sigma_u^-$, $^5\Pi_u$, and $2^3\Sigma_u^+$. We also calculated spin-orbit interactions between these states, and the nonadiabatic coupling matrix element $\langle 2^3\Sigma_u^+|\partial/\partial R|A^3\Sigma_u^+\rangle$. In the long range we used an approach based on undistorted atomic orbitals, to ensure that the states approach their correct atomic limit, defined by the quadrupole-quadrupole interaction, which is the first term in the multipole expansion of the interatomic potential. We combined these long range results with CASSCF optimized orbitals MRCI results employing an aug-cc-pV5Z AO basis. The resulting curves for the bound states reproduce all experimentally known vibrational levels within 1 %, and rotational constants within 1 % for all levels, except the very highest. The correctness of the atomic limit is necessary to obtain consistency in the nonadiabatic coupling matrix element and the spin-orbit matrix elements, that were also calculated as a function of the internuclear distance R. The nonadiabatic coupling was calculated in the same one-electron basis as the potential curves, the spin-orbit interaction in a smaller basis. We estimate the error in the spin-orbit matrix elements to be about 3 %.

Acknowledgments

The authors thank Ad van der Avoird and Paul E. S. Wormer for useful discussions and for carefully reading the paper. This research has been financially supported by the Council for Chemical Sciences of the Netherlands Organization for Scientific Research (CW-NWO).

Bibliography

[1] R. P. Wayne, *Chemistry of Atmospheres*, Clarendon Press, Oxford, 2nd edition, 1991.

[2] D. H. Parker, Acc. Chem. Res. **33**, 563 (2000).

[3] S. Chapman, Mem. R. Meteorol. Soc. **3**, 103 (1930).

[4] B. Buijsse, W. J. van der Zande, A. T. J. B. Eppink, D. H. Parker, B. R. Lewis, and S. T. Gibson, J. Chem. Phys. **108**, 7229 (1998).

[5] M.-F. Mérienne, A. Jenouvrier, B. Coquart, M. Carleer, S. Fally, R. Colin, A. C. Vandaele, and C. Hermans, J. Mol. Spectrosc. **202**, 171 (2000).

[6] K. Yoshino, J. R. Esmond, W. H. Parkinson, A. P. Thorne, R. C. M. Learner, G. Cox, and A. S.-C. Cheung, J. Chem. Phys. **112**, 9791 (2000).

[7] A. Jenouvrier, M.-F. Mérienne, B. Coquart, M. Carleer, S. Fally, A. C. Vandaele, C. Hermans, and R. Colin, J. Mol. Spectrosc. **198**, 136 (1999).

[8] K. Yoshino, J. R. Esmond, W. H. Parkinson, A. P. Thorne, R. C. M. Learner, and G. Cox, J. Chem. Phys. **111**, 2960 (1999).

[9] J. P. England, B. R. Lewis, and S. T. Gibson, Can. J. Phys. **74**, 185 (1996).

[10] K. Yoshino, J. R. Esmond, J. E. Murray, W. H. Parkinson, A. P. Thorne, R. C. M. Learner, and G. Cox, J. Chem. Phys. **103**, 1243 (1995).

[11] M. C. G. N. van Vroonhoven and G. C. Groenenboom, J. Chem. Phys. **116**, 1965 (2002), Chapter 3 of this thesis.

[12] S. J. Singer, K. F. Freed, and Y. B. Band, J. Chem. Phys. **79**, 6060 (1983).

[13] P. E. S. Wormer, F. Mulder, and A. van der Avoird, Int. J. Quantum Chem. **11**, 959 (1977).

[14] R. N. Zare, *Angular momentum*, Wiley, New York, 1988.

[15] R. McWeeny, *Methods of molecular quantum mechanics*, Academic, London, 2nd edition, 1988.

[16] C. E. Moore, *Atomic energy levels as derived from the analysis of optical spectra, Volume I*, Number 35 in National Sandards Reference Data Series, National Bureau of Standards, Washington D.C., 1971.

[17] MOLPRO is a package of ab initio programs written by H.-J. Werner and P. J. Knowles, with contributions from J. Almlöf *et al.*

[18] T. H. Dunning, Jr., J. Chem. Phys. **90**, 1007 (1989).

[19] H.-J. Werner and P. J. Knowles, J. Chem. Phys. **82**, 5053 (1985).

[20] P. J. Knowles and H.-J. Werner, Chem. Phys. Lett. **115**, 259 (1985).

[21] H.-J. Werner and P. J. Knowles, J. Chem. Phys. **89**, 5803 (1988).

[22] P. J. Knowles and H.-J. Werner, Chem. Phys. Lett. **145**, 514 (1988).

[23] J. A. Pople, R. Seeger, and R. Krishnan, Int. J. Quantum Chem., Quantum Chem. Symp. **11**, 149 (1977).

[24] F. B. van Duijneveldt, IBM Research Report RJ945, 1971.

[25] The MOLPRO basis set library can be accessed online at http://www.tc.bham.ac.uk/molpro/molpro2000.1/molpro_basis.

[26] S. F. Boys and F. Bernardi, Mol. Phys. **19**, 553 (1970).

[27] J. H. van Lenthe, J. G. C. M. van Duijneveldt-van de Rijdt, and F. B. van Duijneveldt, Adv. Chem. Phys. **69**, 521 (1987).

[28] T. van Mourik, A. K. Wilson, K. A. Peterson, D. E. Woon, and T. H. Dunning, Jr., Adv. Quantum Chem. **31**, 105 (1999).

[29] K. T. Tang and J. P. Toennies, J. Chem. Phys. **80**, 3726 (1984).

[30] P. J. Knowles, C. Hampel, and H.-J. Werner, J. Chem. Phys. **99**, 5219 (1993).

[31] P. J. Knowles, C. Hampel, and H.-J. Werner, J. Chem. Phys. **112**, 3106 (2000).

[32] J. D. Watts, J. Gauss, and R. J. Bartlett, J. Chem. Phys. **98**, 8718 (1993).

[33] A. K. Wilson, T. van Mourik, and T. H. Dunning, Jr., J. Mol. Struct. (THEOCHEM) **388**, 339 (1997).

[34] B. Zygelman, A. Dalgarno, and R. D. Sharma, Phys. Rev. A **50**, 3920 (1994).

[35] See AIP Document No. E-JCPSA6-116-303204 for a Fortran implementation of the fit of the potential energy curves, spin-orbit couplings, and the radial derivative nonadiabatic coupling matrix element. This document may be retrieved via the EPAPS homepage (http://www.aip.org/pubserv/epaps.html) or via FTP from ftp://ftp.aip.org/epaps/. See the EPAPS homepage for more information. See also http://www.theochem.kun.nl/˜gerritg/.

[36] T. G. Slanger and P. C. Cosby, J. Phys. Chem. **92**, 267 (1988).

[37] H. Partridge, C. W. Bauschlicher, Jr., S. R. Langhoff, and P. R. Taylor, J. Chem. Phys. **95**, 8292 (1991).

[38] M. C. G. N. van Vroonhoven and G. C. Groenenboom, Manuscript in preparation (2001), Chapter 4 of this thesis.

[39] G. C. Groenenboom and D. T. Colbert, J. Chem. Phys. **99**, 9681 (1993), note the mistake in the signs between the two terms in the first and second part of Eq. (48). See also D. T. Colbert and W. H. Miller, J. Chem. Phys. **96**, 1982 (1992).

[40] T. G. Slanger, D. L. Huestis, P. C. Cosby, H. Naus, and G. Meijer, J. Chem. Phys. **105**, 9393 (1996).

[41] R. Klotz and S. D. Peyerimhoff, Mol. Phys. **57**, 573 (1986).

[42] A. Landé, Z. Physik **15**, 189 (1923).

[43] A. Landé, Z. Physik **19**, 112 (1923).

Chapter 3

Photodissociation of $\mathrm{O_2}$ *in the Herzberg continuum. II. Calculation of fragment polarization and angular distribution*

Abstract

Parallel and perpendicular components of the Herzberg I, II, and III transitions contribute to the photodissociation of $\mathrm{O_2}$ in the Herzberg continuum. The photodissociation dynamics determines the $\mathrm{O}(^3P_j)$, $j = 0, 1$, and 2 atomic fine-structure branching ratios and angular distributions, which were determined in ion imaging experiments at $\lambda = 236$, 226, and 204 nm by Buijsse *et al.* [J. Chem. Phys. **108**, 7229 (1998)]. In the preceding paper we presented potential energy curves for all eight ungerade $\mathrm{O_2}$ states that correlate with the $\mathrm{O}(^3P)$ + $\mathrm{O}(^3P)$ dissociation limit, and the R-dependent spin-orbit and the nonadiabatic radial derivative couplings between these states. Here, we employ these potentials and couplings in a semiclassical calculation of the fine-structure branching ratios, atomic polarizations, and fine-structure resolved anisotropy parameters. We discuss the adiabaticity of the dissociation by comparing the results with adiabatic and diabatic models. The $\mathrm{O}(^3P_j)$ 2+1 REMPI detection scheme used in the experiment is sensitive to the polarization of the atomic fragments. We predict an important effect of the polarization on the anisotropy of the $j = 1$ and $j = 2$ ion images at low energies ($\lambda > 236$ nm). The agreement between the semiclassical calculations and experiment is reasonable, possible explanations for the remaining differences are discussed.

3.1 Introduction

The photodissociation of molecules into open-shell fragments is interesting because generally multiple coupled electronic states are involved. For nonsinglet state fragments the (nonadiabatic) couplings determine the fine-structure branching ratios. This has been studied in detail for the relatively simple HCl and OH molecules.[1,2] The photodissociation of O_2 in the Herzberg continuum is complicated since already in the excitation step several electronically excited states are involved. Both parallel and perpendicular electronic transitions contribute. This is reflected in the angular distribution of the photofragments, which was studied by Buijsse *et al.*[3] with the velocity mapped ion imaging technique.[4] In the experiment O_2 was cooled to 5-10 K in a molecular beam, and photodissociated with a linearly polarized laser at 236, 226, and 204 nm. At these energies only the three fine-structure components of the ground state $O(^3P_{j=2,1,0})$ atoms can be produced. State selective detection of the atoms was achieved by (2+1) resonance enhanced multiphoton ionization (REMPI) of the $O(^3P_j)$ states. The angular distribution of the $O(^3P_j)$ photofragments can be expressed as $[1+\beta_j(E)P_2(\cos\theta)]$, where P_2 is the second order Legendre polynomial, θ is the angle between the polarization of the dissociation laser and the recoil velocity, and $\beta_j(E)$ is the fine-structure resolved and energy dependent anisotropy parameter. The observed ion image actually corresponds to the distribution of the ions. This may be different from the distribution of the atoms when the atoms are polarized, because the ionization efficiency depends on the angle between the recoil velocity and the polarization of the detection laser. This angle is equal to θ because the laser polarizations were taken parallel to each other. In the case of direct dissociation, which is appropriate in this case, the fine-structure averaged β parameter is fully determined by the parallel/perpendicular character of the initial electronic excitation.

The fine-structure dependent anisotropy parameters $\beta_j(E)$ may differ for $j = 2$, 1, and 0, if the fine-structure branching ratios of the electronic states reached via a parallel transition differ from those reached via perpendicular transitions. In the adiabatic limit all electronic states involved correlate with the $O(^3P_2) + O(^3P_2)$ limit. It turns out that even at 236 nm the dissociation is not fully adiabatic and hence the experiment contains information on the nonadiabatic coupling between the electronic states.

Apart from the initially excited Herzberg states ($A^3\Sigma_u^+$, $c^1\Sigma_u^-$, and $A'\,^3\Delta_u$) there are five other ungerade states ($1^1\Pi_u$, $1^3\Pi_u$, $2^3\Sigma_u^+$, $1^5\Pi_u$, and $1^5\Sigma_u^-$) that correlate with the $O(^3P) + O(^3P)$ dissociation limit and are involved in the dissociation dynamics through spin-orbit interactions (in the long range). Furthermore, the $A^3\Sigma_u^+$ and $2^3\Sigma_u^+$ states are coupled through the radial derivative coupling $g_{2,A}(R) = \langle 2^3\Sigma_u^+|\partial/\partial R|A^3\Sigma_u^+\rangle$ which arises from the nonseparability of the electronic and nuclear motion. In the preceding paper,[5] which we will refer to as paper I, we presented high quality *ab initio* calculations of the potential energy curves and R-dependent spin-orbit couplings for all eight electronic states, as well as $g_{2,A}(R)$. In the present paper we employ these *ab initio* results in a semiclassical calculation of the energy dependent fine-structure branching ratios for the three Herzberg states. We also compute the energy dependent atomic alignment. By taking into account the experimental values in Ref. 3 for the parallel and perpendicular branching ratios of the Herzberg transitions we calculate the anisotropy parameters for the ions, which we compare to the experimental results of Buijsse.[3]

In the present work we neglect the possible effects of coherent excitation of the Herzberg states and Coriolis coupling. Such effects may be important for photodissociation of O_2 in a well defined initial quantum state, for which no experimental data is available yet. Also, properly describing these effects may require a full coupled-channels quantum treatment. Thus, the present semiclassical study should be considered as the first step beyond the adiabatic and diabatic models. Note that a full quantum treatment would also require knowledge of the radial second derivative nonadiabatic couplings and a complete model of the initial electronic excitation, rather than just the electronic excitation branching ratios.

The outline of this paper is as follows. In the next section (Sec. 3.2) we present the theoretical framework of this paper. We describe the construction of diabatic and adiabatic models (Sec. 3.2.1), the semiclassical calculation and our extended diabatic model, which includes the nonadiabatic radial derivative coupling (Sec. 3.2.2), and the procedure to calculate atomic fine-structure branching ratios, alignment and ion images from the dynamics results (Sec. 3.2.3). In Sec. 3.3 we discuss the results of the dynamics calculations, and the resulting fragment branching ratios and alignments. We present our conclusions in Sec. 3.4. The derivation of the angular REMPI detection sensitivity is given in the Appendix.

3.2 Theory

3.2.1 Adiabatic and diabatic model

The construction of adiabatic and diabatic models to describe the fine-structure branching in diatomic molecules is well established.[6,7] First, we partition the total electronic Hamiltonian

$$\hat{H}(R) = \hat{H}_{\text{coul}}(R) + \hat{H}_{\text{SO}}(R), \tag{3.1}$$

where $\hat{H}_{\text{coul}}(R)$ is the nonrelativistic electronic Hamiltonian in the clamped nuclei approximation, $\hat{H}_{\text{SO}}(R)$ is the (Breit-Pauli) spin-orbit operator and R is the internuclear separation. In the region where the initial photoexcitation occurs ($R = R_a$) we assume that the eigenfunctions of $\hat{H}_{\text{coul}}$ are a good first order approximation to the eigenfunctions of the full electronic Hamiltonian and $\hat{H}_{\text{SO}}$ gives a small perturbation. The choice of R_a is not critical, provided that the adiabatic Born-Oppenheimer (ABO) potentials, i.e. the eigenvalues of $\hat{H}_{\text{coul}}$, are well separated in this region. We take $R_a = 2.85$ a$_0$. Adiabatic dissociation with respect to $\hat{H}_{\text{coul}}$ implies that the ith electronic eigenstate of $\hat{H}_{\text{coul}}(R_a)$ of a given symmetry evolves into the ith eigenstate of the same symmetry for $R \to \infty$. When, for a given symmetry, the eigenstates of $\hat{H}_{\text{coul}}(\infty)$ are degenerate we define the asymptotic ABO eigenstates by considering the leading interatomic term of the multipole expansion of $\hat{H}_{\text{coul}}$ at large R that lifts the degeneracy. We followed this procedure in paper I to arrive at the ABO states $|(L)\Lambda S\Sigma; R\rangle$, which are eigenstates of $\hat{H}_{\text{coul}}(R)$ and where Λ, S, and Σ are (good) Hund's case (a) quantum numbers of the O_2 molecule. By considering the quadrupole-quadrupole interaction between the O(^3P) fragments, we found that L, which is the asymptotic total orbital angular momentum, can be used to label the asymptotically degenerate $A^3\Sigma_u^+(L=0)$ and $2^3\Sigma_u^+(L=2)$ states for any R.

The ABO states are eigenfunctions of the electronic inversion operator[8] $\hat{\pi}$, with eigenvalues $(-1)^{L+S}$. Here we consider only ungerade states, so $L+S$ must be odd. We should also consider the inversion operator $\hat{\imath}$, which inverts both electronic and nuclear coordinates and which determines parity. For $\Omega \equiv \Lambda + \Sigma \neq 0$ states, however, this operator affects the rotational part of the wave function,[9] which we do not explicitly include in the present semiclassical formulation and so we may ignore it. For $\Omega = 0$ states we have[9]

$$\hat{\imath}|(L)\Lambda S\Sigma; R\rangle = (-1)^{L+S}|(L){-\Lambda} S{-\Sigma}; R\rangle. \tag{3.2}$$

Ungerade states with $\Lambda = \Sigma = 0$ have an intrinsic parity of -1. For $\Lambda = -\Sigma \neq 0$ both odd and even parity states can be constructed. Note, however, that in the calculation of the spin-orbit coupling in paper I we employed the parity unadapted $^{3,5}\Pi_{u,0}(\Lambda = \pm 1)$ states. Asymptotically the ABO wave functions $|L\Lambda S\Sigma\rangle \equiv |(L)\Lambda S\Sigma; \infty\rangle$ can be expanded in product atomic wave functions

$$|L\Lambda S\Sigma\rangle = \sum_{\lambda_a\lambda_b\sigma_a\sigma_b} |l_a\lambda_a\rangle|s_a\sigma_a\rangle|l_b\lambda_b\rangle|s_b\sigma_b\rangle\langle l_a\lambda_a l_b\lambda_b|L\Lambda\rangle\langle s_a\sigma_a s_b\sigma_b|S\Sigma\rangle, \tag{3.3}$$

where a and b label the atoms and for O(^3P) $l_a = l_b = s_a = s_b = 1$ and $\lambda_a, \lambda_b, \sigma_a$, and σ_b are projections of the atomic angular momenta on the internuclear axis. The symbol $\langle a\alpha b\beta|c\gamma\rangle$ is a Clebsch-Gordan coefficient.

Since the spin-orbit interaction does not vanish asymptotically the analysis of the photofragments requires a recoupling to product atomic multiplet states $|j_a\omega_a j_b\omega_b\rangle \equiv |j_a\omega_a\rangle|j_b\omega_b\rangle$ where

$$|j_i\omega_i\rangle = \sum_{\lambda_i\sigma_i} |l_i\lambda_i\rangle|s_i\sigma_i\rangle\langle l_i\lambda_i s_i\sigma_i|j_i\omega_i\rangle \;;\; i = a, b. \tag{3.4}$$

The transformation between the ABO states and the atomic eigenstates can be expressed as[9]

$$\langle j_a\omega_a j_b\omega_b|L\Lambda S\Sigma\rangle = \sum_{j'=0}^{4}\langle j_a\omega_a j_b\omega_b|j'\Omega\rangle\langle j'\Omega|L\Lambda S\Sigma\rangle\sqrt{[j_a][j_b][L][S]}\begin{Bmatrix} l_a & s_a & j_a \\ l_b & s_b & j_b \\ L & S & j' \end{Bmatrix}, \tag{3.5}$$

where $[X] \equiv 2X+1$ and the last factor is a $9-j$ symbol. This description of the photodissociation, correlating the ABO eigenstates $|(L)\Lambda S\Sigma; R_a\rangle$ of $\hat{H}_{\text{coul}}(R_a)$ with asymptotic ABO states $|L\Lambda S\Sigma\rangle$, and using Eq. (3.5) to transform the asymptotic ABO states into product atomic multiplet states, is called *diabatic* with respect to spin-orbit coupling, since the effect of the spin-orbit coupling is treated by the basis transformation. According to the Massey criterion[10] the diabatic or spin-orbit sudden limit is reached when the time for traversing the SO recoupling zone is small compared to $\hbar/\Delta E_{\text{SO}}$, where ΔE_{SO} is the spin-orbit coupling. This is the high recoil velocity limit.

The low recoil velocity limit may be described by a model which is adiabatic with respect to the total electronic Hamiltonian $\hat{H}(R)$ [Eq. (3.1)]. In this case Λ and Σ are no longer good quantum numbers and the noncrossing rule only applies to states with the same value of Ω. Since $\hat{\pi}$ commutes with $\hat{H}_{\text{SO}}$ as well as with $\hat{H}_{\text{coul}}$ and the electronic states excited are ungerade, we construct *ungerade* coupled atomic states

$$|j_a\omega_a j_b\omega_b\rangle_u = 2^{-\frac{1}{2}}\left[|j_a\omega_a j_b\omega_b\rangle - |j_b\omega_b j_a\omega_a\rangle\right]. \tag{3.6}$$

Note that for dissociation into a $j_a = j_b$ channel we must have $\omega_a \neq \omega_b$. For $\omega_a + \omega_b = \Omega = 0$ intrinsic parity adapted states may be constructed using

$$\hat{\imath}|j_a\omega_a j_b{-}\omega_a\rangle = (-1)^{j_a+j_b}|j_a{-}\omega_a j_b\omega_a\rangle. \tag{3.7}$$

From this it follows that ungerade $\Omega = 0$ states with $j_a = j_b$ are odd parity states. The asymptotic energy of $|j_a\omega_a j_b\omega_b\rangle_u$ is $E_{j_a} + E_{j_b}$ with

$$E_j = (1/2)A[j(j+1) - l(l+1) - s(s+1)] = (1/2)A[j(j+1) - 4], \tag{3.8}$$

where A is the atomic spin-orbit coupling constant[11] of –0.353 mE$_h$. These rules are sufficient to derive the adiabatic correlation diagram for the eight ungerade O_2 states as shown in Fig. 8 of Ref. 7. The Herzberg states all correlate adiabatically with the $j_a = j_b = 2$ limit. For $\Omega = 2, 3$ [i.e. $A'\ ^3\Delta_{u,2/3}$] we immediately find that the asymptotic states must be $|2220\rangle_u$ and $|2221\rangle_u$, respectively. However, for $\Omega = 0^-$ there are two asymptotically degenerate states: $|222{-}2\rangle_{u^-}$ and $|212{-}1\rangle_{u^-}$, and for $\Omega = 1$ we have $|222{-}1\rangle_u$ and $|2120\rangle_u$. In order to find the atomic polarization in the adiabatic model for the $\Omega = 0^-$ states we must find the proper linear combination of $|222{-}2\rangle_{u^-}$ and $|212{-}1\rangle_{u^-}$ that correlates with the lowest lying $\Omega = 0^-$ Herzberg state

Table 3.1: Adiabatic correlation between molecular Herzberg states and product atomic states.

State	$\sum_i c_i \vert j_a\omega_a j_b\omega_b\rangle_u$
$c^1\Sigma^-_{u,0^-}$	$0.525\,73\vert 2{-}222\rangle_u - 0.850\,65\vert 2{-}121\rangle_u$
$A^3\Sigma^+_{u,0^-}$	$0.850\,65\vert 2{-}222\rangle_u + 0.525\,73\vert 2{-}121\rangle_u$
$A'\ {}^3\Delta_{u,1}$	$-0.985\,87\vert 2{-}122\rangle_u + 0.167\,51\vert 2021\rangle_u$
$A^3\Sigma^+_{u,1}$	$0.167\,51\vert 2{-}122\rangle_u + 0.985\,87\vert 2021\rangle_u$
$A'\ {}^3\Delta_{u,2}$	$1.0\vert 2220\rangle_u$
$A'\ {}^3\Delta_{u,3}$	$1.0\vert 2122\rangle_u$

$(c^1\Sigma^-_{u,0^-})$. For $\Omega = 1$ we must find the proper linear combination of $|222{-}1\rangle_u$ and $|2120\rangle_u$ that correlates with $A'\ {}^3\Delta_{u,1}$, the lowest lying $\Omega = 1$ Herzberg state. Just as in the construction of the asymptotic ABO states we do this by diagonalizing the quadrupole-quadrupole interaction in the basis of degenerate states. The matrix elements ${}_u\langle j_a\omega_a j_b\omega_b|\hat{V}_5|j_a\omega'_a j_b\omega'_b\rangle_u$ are found by inserting the resolution of identity in the molecular basis, $\hat{I} = \sum_{L\Lambda S\Sigma} |L\Lambda S\Sigma\rangle\langle L\Lambda S\Sigma|$, twice ($\hat{V}_5 = \hat{I}\hat{V}_5\hat{I}$). The transformation coefficients are given in Eq. (3.5) and the quadrupole-quadrupole matrix elements in the molecular basis are given in Eq. (9) in paper I. Following this procedure we obtained the complete adiabatic model for the Herzberg states as given in Table 3.1.

3.2.2 Semiclassical Dynamics

The Massey criterion gives only a crude indication of the validity of the adiabatic or diabatic models for predicting branching ratios. It is even less clear whether the models can be used to predict fragment polarization. Furthermore, the diabatic model presented so far does not take into account the effect of the nonadiabatic radial derivative coupling between the $A^3\Sigma^+_u$ and $2^3\Sigma^+_u$ states, which should be important in the high energy limit. Finally, the SO coupling in the Franck-Condon region is not completely negligible. Thus, we performed semiclassical calculations to study the energy dependence of the photodissociation process. It is well established[12, 13] that the semiclassical approximation is valid for a De Broglie wavelength $\lambda/a_0 \ll 2\pi$. For the energy range considered in the experiment we have $0.2a_0 \leq \lambda \leq 0.6a_0$.

In the present semiclassical study we neglect the possible effects of coherent excitation of the Herzberg states. At $R_a = 2.85$ a$_0$ we compute the eigenfunctions of the total electronic Hamiltonian

$$\left[\hat{H}(R_a) - E_{i\Omega}(R_a)\right] \Psi_{i\Omega}(R_a) = 0, \tag{3.9}$$

where i labels the eigenstates, sorted on energy, within each Ω symmetry

Table 3.2: Herzberg excitation branching ratios $r_{i\Omega}$ and anisotropy parameters $\beta_{i\Omega}$ for the different molecular eigenstates $(i\Omega)$ of the Herzberg transition. These depend on the excitation wavelength λ in nm. Given energy dependencies are linear fits from Fig. 7 of Ref. 3, and $\lambda' \equiv \lambda - 226$.

State	$(i, \|\Omega\|)$	$\beta_{i\Omega}$	$r_{i\Omega}$
$c^1\Sigma^-_{u,0^-}$	$(1,0)$	-1	$0.0228 + 3.439 \cdot 10^{-4}\lambda'$
$A'\ {}^3\Delta_{u,1}$	$(1,1)$	-1	$0.0223 + 3.356 \cdot 10^{-4}\lambda'$
$A'\ {}^3\Delta_{u,2}$	$(1,2)$	-1	$0.0334 + 5.034 \cdot 10^{-4}\lambda'$
$A'\ {}^3\Delta_{u,3}$	$(1,3)$	-1	$0.0005 + 7.5 \cdot 10^{-6}\lambda'$
$A^3\Sigma^+_{u,0^-}$	$(2,0)$	-1	$0.1883 - 6.822 \cdot 10^{-4}\lambda' +5.67 \cdot 10^{-7}\lambda'^2$
$A^3\Sigma^+_{u,1}$	$(2,1)$	$1.2288 +2.2589 \cdot 10^{-3}\lambda' -2.1328 \cdot 10^{-6}\lambda'^2$	$0.7327 - 5.0779 \cdot 10^{-4}\lambda' -5.67 \cdot 10^{-7}\lambda'^2$

block. Near equilibrium geometry the energy ordering of the states is $c^1\Sigma^-_u$, $A'\ {}^3\Delta_u$, and $A^3\Sigma^+_u$. So for $\Omega = 0$, $i = 1$ and 2 correspond to $c^1\Sigma^-_u$ and $A^3\Sigma^+_u$ respectively. For $\Omega = 1$ the lowest state ($i = 1$) is $A'\ {}^3\Delta_u$, and $A^3\Sigma^+_u$ corresponds to $i = 2$. For $\Omega = 2$ and 3 we only have $A'\ {}^3\Delta_u$ initial states, these have $i = 1$. See also Table 3.2. We take each of the eigenfunctions corresponding to the Herzberg states as initial conditions for the semiclassical propagation. We expand $\Psi_{i\Omega}(R)$ in a basis of ABO states,

$$\Psi_{i\Omega}(R) = \sum_{L\Lambda S\Sigma} c^{i\Omega}_{L\Lambda S\Sigma}(R)|(L)\Lambda S\Sigma; R\rangle. \tag{3.10}$$

Substituting this expression in the time-dependent Schrödinger equation while treating $R = R(t)$ as a classical coordinate and projecting with $\langle(L)\Lambda S\Sigma; R|$ gives the quantum-mechanical equations of motion

$$\begin{aligned} i\hbar\frac{\partial}{\partial t}\left\{c^{i\Omega}_{L\Lambda S\Sigma}[R(t)]\right\} = \sum_{L'\Lambda'S'\Sigma'} \Big\{ & \langle(L)\Lambda S\Sigma; R|\hat{H}[R(t)]|(L')\Lambda'S'\Sigma'; R\rangle \\ & -i\hbar\frac{dR(t)}{dt}\langle(L)\Lambda S\Sigma; R|\frac{\partial}{\partial R}|(L')\Lambda'S'\Sigma'; R\rangle\Big\} c^{i\Omega}_{L'\Lambda'S'\Sigma'}[R(t)]. \end{aligned} \tag{3.11}$$

The diagonal elements of the first term on the right-hand side of this equation are equal to the ABO potentials $\epsilon_{L|\Lambda|S}(R)$ and the off-diagonal elements are the SO couplings. The radial derivative term arises from $\frac{\partial}{\partial t} = \frac{dR}{dt}\frac{\partial}{\partial R}$. This term only couples the $A^3\Sigma^+_u(|(0)01\Sigma; R\rangle)$ and $2^3\Sigma^+_u(|(2)01\Sigma; R\rangle)$ states. The computation of the ABO potentials and the SO and $\partial/\partial R$ coupling is described in paper I. The nuclear motion $[R(t)]$ is governed by the classical Hamiltonian

$$H_{\mathrm{cl}} = \frac{p_R^2}{2\mu} + \langle \Psi[R(t)] | \hat{H}[R(t)] | \Psi[R(t)] \rangle, \tag{3.12}$$

where μ is the reduced mass of O_2 and p_R is the momentum conjugate to R. The classical equations of motion are

$$\frac{dR}{dt} = \frac{\partial H_{\mathrm{cl}}}{\partial p_R} = \frac{p_R}{\mu} \tag{3.13}$$

$$\begin{aligned} \frac{dp_R}{dt} &= -\frac{\partial H_{\mathrm{cl}}}{\partial R} \\ &= -\sum_{L\Lambda S\Sigma} \sum_{L'\Lambda' S'\Sigma'} c_{L\Lambda S\Sigma}^{i\Omega *}[R(t)] \langle L\Lambda S\Sigma | \frac{\partial \hat{H}}{\partial R} | L'\Lambda' S'\Sigma' \rangle c_{L'\Lambda' S'\Sigma'}^{i\Omega}[R(t)]. \end{aligned} \tag{3.14}$$

The initial conditions for the electronic state $(i\Omega)$ are $R(0) = R_a$ and $p_R(0) = \sqrt{2\mu(E - E_{i\Omega})}$. The total energy is given by $E = h\nu - D_0 + 2E_{j=2}$, where ν is the frequency of the dissociation laser, $D_0 = 188.034$ mE$_h$ is the dissociation energy[14] of the ground state $X^3\Sigma_g^-$ and $E_{j=2} = -0.3526$ mE$_h$ is the energy of an $O(^3P_2)$ atom with respect to our zero point of energy, which is chosen such that $\epsilon_{L|\Lambda|S}(\infty) = 0$. The semiclassical equations have been solved numerically using the MATLAB computer linear algebra system.[15]

In addition to the semiclassical calculations we will also present the results of an extended diabatic model. In this model we still assume that SO coupling is negligible, but we do take into account the radial derivative coupling. Hence one may also refer to this model as spin-orbit sudden. Only for the $A^3\Sigma_u^+$ state it deviates from the diabatic model presented above. For this state it amounts to expanding the wave function as

$$\Psi(R) = c_0(R) |(0)01\Sigma; R\rangle + c_2(R) |(2)01\Sigma; R\rangle \tag{3.15}$$

and solving the semiclassical equations for two states, without the SO coupling, and with the initial condition $c_0(R_a) = 1; c_2(R_a) = 0$. Thus Eq. (3.11) becomes

$$i\hbar \frac{\partial}{\partial t} \begin{bmatrix} c_0[R(t)] \\ c_2[R(t)] \end{bmatrix} = \begin{bmatrix} \epsilon_{001}[R(t)] & i\hbar \dot{R} g_{2,A}[R(t)] \\ -i\hbar \dot{R} g_{2,A}[R(t)] & \epsilon_{201}[R(t)] \end{bmatrix} \begin{bmatrix} c_0[R(t)] \\ c_2[R(t)] \end{bmatrix}. \tag{3.16}$$

When $\dot{R} = \frac{dR}{dt}$ is negligible we find $|c_0(\infty)| = 1$ and $c_2(\infty) = 0$ and hence the model reduces to the simple diabatic model presented above. In the high energy limit the potentials are negligible compared to the coupling and we find $c_0(\infty) = \cos\phi$ and $c_2(\infty) = \sin\phi$ with

$$\phi = -\int_{R_a}^{\infty} g_{2,A}(R') dR'. \tag{3.17}$$

With the radial derivative coupling computed in paper I we find $\phi = 33.74°$.

3.2.3 Ion image

The computation of the ion image requires the O(^3P_j) fine-structure populations and polarizations.[16,17] These are obtained by expanding the electronic wave function at large $R = R_b$ (we take $R_b = 15$ a$_0$ in the semiclassical calculation) in the coupled atomic basis

$$\Psi_{i\Omega}(R_b) = \sum_{j_a\omega_a j_b\omega_b} c^{i\Omega}_{j_a\omega_a j_b\omega_b}(R_b)|j_a\omega_a j_b\omega_b\rangle. \tag{3.18}$$

The expansion coefficients are calculated using the recoupling matrix element given in Eq. (3.5),

$$c^{i\Omega}_{j_a\omega_a j_b\omega_b}(R_b) = \sum_{L\Lambda S\Sigma} \langle j_a\omega_a j_b\omega_b|L\Lambda S\Sigma\rangle c^{i\Omega}_{L\Lambda S\Sigma}(R_b). \tag{3.19}$$

The two-atom density matrix is defined by

$$\rho^{i\Omega}_{j_a\omega_a j_b\omega_b;j'_a\omega'_a j'_b\omega'_b}(R_b) = c^{i\Omega}_{j_a\omega_a j_b\omega_b}(c^{i\Omega}_{j'_a\omega'_a j'_b\omega'_b})^*. \tag{3.20}$$

A partial trace over the quantum numbers of atom b gives the reduced density matrix for atom a

$$\rho^{i\Omega}_{j_a\omega_a;j'_a\omega'_a}(R_b) = \sum_{j_b\omega_b j'_b\omega'_b} \rho^{i\Omega}_{j_a\omega_a j_b\omega_b;j'_a\omega'_a j'_b\omega'_b}(R_b)\delta_{j_b j'_b}\delta_{\omega_b\omega'_b}. \tag{3.21}$$

Since atoms a and b are indistinguishable and we are only interested in relative intensities we may ignore atom b. Using $\omega_a + \omega_b = \Omega = \omega'_a + \omega'_b$ in Eq. (3.21) shows that $\rho^{i\Omega}_{j_a\omega_a;j'_a\omega'_a}(R_b) = 0$ for $\omega_a \neq \omega'_a$. This is a direct consequence of ignoring coherence in the excitation of different Ω states. The detection is fine-structure selective, hence the atomic products are described by a $j_a = j'_a = j$ block of the density matrix, which is diagonal

$$\rho^{i\Omega}_{j\omega;j\omega'}(R_b) = P^{i\Omega}_{j\omega}\delta_{\omega\omega'}. \tag{3.22}$$

The R_b dependence disappears when R_b is sufficiently large. The atomic fine-structure level populations are given by

$$P^{i\Omega}_j = \sum_\omega P^{i\Omega}_{j\omega}. \tag{3.23}$$

The polarizations of the O(^3P_j) states are given by the irreducible components of the density matrix[18]

$$\begin{aligned}\rho^{(k)}_q(i\Omega;j) &= (P^{i\Omega}_j)^{-1}\sum_{\omega\omega'}(-1)^{j-\omega}\langle j\omega j{-}\omega'|kq\rangle\rho^{i\Omega}_{j\omega;j\omega'}(R_b)\\ &= (P^{i\Omega}_j)^{-1}\delta_{q,0}\sum_{\omega}(-1)^{j-\omega}\langle j\omega j{-}\omega|k0\rangle P^{i\Omega}_{j\omega}.\end{aligned} \tag{3.24}$$

We normalized the multipole moments with respect to the population of level j. Note that

$$\begin{aligned}\rho_0^{(0)}(i\Omega;j) &= (2j+1)^{-1/2}\\ -\frac{2}{\sqrt{6}} \leq \rho_0^{(2)}(i\Omega;j=1) &\leq \frac{1}{\sqrt{6}}\\ -\frac{2}{\sqrt{14}} \leq \rho_0^{(2)}(i\Omega;j=2) &\leq \frac{2}{\sqrt{14}}\\ -\frac{4}{\sqrt{70}} \leq \rho_0^{(4)}(i\Omega;j=2) &\leq \frac{6}{\sqrt{70}}.\end{aligned} \tag{3.25}$$

These normalized multipole moments are related to Zare's molecular frame polarization parameters[19] $A_q^{(k)}$ through:

$$\rho_0^{(k)}(j) = \frac{\sqrt{2k+1}[j(j+1)]^{k/2}}{c(k)\langle j||J^{(k)}||j\rangle} A_0^{(k)}. \tag{3.26}$$

For k up to 4 the reduced matrix elements $\langle j||J^{(k)}||j\rangle$ of the operator equivalents $J^{(k)}$ of order k are listed by Zare,[19] and the normalization constants $c(k)$ are given by Orr-Ewing.[20] General expressions for these quantities are

$$\begin{aligned}\langle j||J^{(k)}||j\rangle &= \sqrt{\frac{(2j+k+1)!(k!)^2}{(2j-k)!2^k(2k)!}}\\ c(k) &= \sqrt{\frac{(2k-1)!!}{k!}}(1+\delta_{k,2}).\end{aligned} \tag{3.27}$$

The REMPI detection scheme uses a two-photon transition, for which in general the relative absorption intensity is given by[21]

$$I = \sum_k \frac{\tilde{\rho}_0^{(k)}}{\tilde{\rho}_0^{(0)}} I_k(j), \tag{3.28}$$

where $I_k(j)$ are relative geometrical factors. In appendix 3.4 we derive for the REMPI detection scheme used in the experiment of Buijsse *et al.*[3] that $I_0(j) = 1, I_2(1) = 2^{-\frac{1}{2}}, I_2(2) = -\sqrt{7/10}$, and $I_4(2) = 0$. The $\tilde{\rho}_0^{(k)}$ are the $q = 0$ multipole moments of the density matrix with respect to the probe frame, i.e., with respect to the polarization axis of the detection laser. Thus, we rotate the multipole moments with respect to the recoil frame to the probe frame by[21]

$$\begin{aligned}\tilde{\rho}_0^{(k)}(i\Omega;j) &= \sum_q \rho_q^{(k)}(i\Omega;j) C_{kq}(\theta,\phi)\\ &= \rho_0^{(k)}(i\Omega;j) P_k(\cos\theta),\end{aligned} \tag{3.29}$$

where we used $\rho_q^{(k)} = 0$ for $q \neq 0$ and for the Racah normalized spherical harmonics $C_{k0}(\theta, \phi) = P_k(\cos\theta)$.

To obtain the ion images we multiply the angular distribution of the atoms $[1 + \beta_{i\Omega} P_2(\cos\theta)]$ with the relative absorption intensity and we weight the contributions of the initial Herzberg states according to the branching ratios $r_{i\Omega}$,

$$I_j^{\text{obs}}(\theta) = \sum_{i\Omega} r_{i\Omega} \left[1 + \beta_{i\Omega} P_2(\cos\theta)\right] \left\{ P_j^{i\Omega} \sum_{k=0}^{2j} \frac{\rho_0^{(k)}(i\Omega; j)}{\rho_0^{(0)}(i\Omega; j)} I_k(j) P_k(\cos\theta) \right\}. \tag{3.30}$$

The branching ratios $r_{i\Omega}$ and the anisotropy parameters $\beta_{i\Omega}$ are taken from the experimental papers[3, 22] and are summarized in Table 3.2. Note that $r_{i\Omega}$, $\beta_{i\Omega}$, $P_j^{i\Omega}$, and $\rho_0^{(k)}(i\Omega; j)$ all depend on the photodissociation laser wavelength. When we multiply out the two Legendre polynomials in Eq. (3.30), and re-expand the result in Legendre polynomials, we find the following expression for the ion image

$$I_j^{\text{obs}}(\theta) = \sum_{k=0,2,4} c_k(E, j) P_k(\cos\theta), \tag{3.31}$$

with

$$\begin{aligned}
c_0(E, j) &= \sum_{i\Omega} r_{i\Omega} P_j^{i\Omega} \left\{ 1 + \frac{2}{10} \beta_{i\Omega} \frac{\rho_0^{(2)}(i\Omega; j)}{\rho_0^{(0)}(i\Omega; j)} I_2(j) \right\}, \\
c_2(E, j) &= \sum_{i\Omega} r_{i\Omega} P_j^{i\Omega} \left\{ \frac{\rho_0^{(2)}(i\Omega; j)}{\rho_0^{(0)}(i\Omega; j)} I_2(j) + \beta_{i\Omega} \left[1 + \frac{2}{7} \frac{\rho_0^{(2)}(i\Omega; j)}{\rho_0^{(0)}(i\Omega; j)} I_2(j) \right] \right\}, \\
c_4(E, j) &= \frac{18}{35} \sum_{i\Omega} r_{i\Omega} \beta_{i\Omega} P_j^{i\Omega} \frac{\rho_0^{(2)}(i\Omega; j)}{\rho_0^{(0)}(i\Omega; j)} I_2(j).
\end{aligned} \tag{3.32}$$

Note that Buijsse *et al.* did not attempt to extract the ratio c_4/c_0 from the images. This results in the following intensity ratios for the ion images for $j = 0, 1, 2$:

$$r_j^{\text{obs}}(E) = c_0(E, j) / \sum_{j'=0}^{2} c_0(E, j') \tag{3.33}$$

and anisotropy parameters of the ions

$$\beta_j^{\text{obs}}(E) = c_2(E, j)/c_0(E, j). \tag{3.34}$$

The polarization effects on the detection can be seen when we compare intensity ratios to the O(^3P_j) fragment branching ratios

$$r_j(E) = \frac{\sum_{i\Omega} r_{i\Omega} P_j^{i\Omega}}{\sum_{i\Omega} \sum_{j'=0}^{2} r_{i\Omega} P_{j'}^{i\Omega}} \tag{3.35}$$

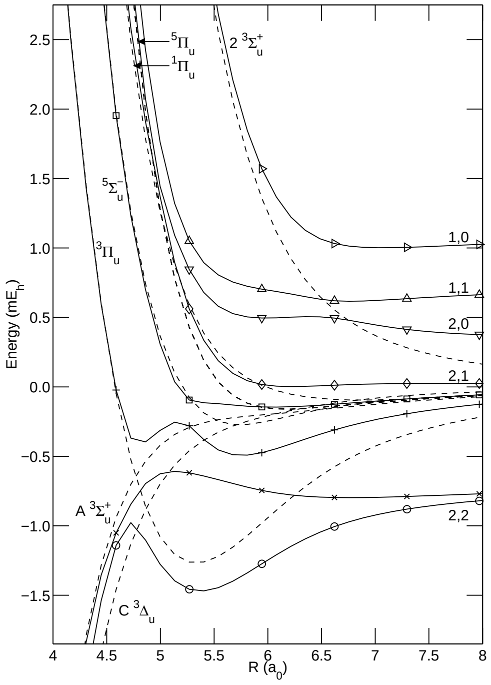

Figure 3.1: The ABO potentials (dashed) and the eigenvalues of the total Hamiltonian $\hat{H}(R)$ (solid), for $\Omega = 1$. The asymptotic limits are marked j_a, j_b.

and anisotropy parameters

$$\beta_j(E) = \frac{\sum_{i\Omega} r_{i\Omega}\beta_{i\Omega}P_j^{i\Omega}}{\sum_{i\Omega} r_{i\Omega}P_j^{i\Omega}}. \tag{3.36}$$

3.3 Results and discussion

Before we present the calculated branching ratios and anisotropy parameters and compare them to the experimental results we will analyze the photodissociation dynamics of the $A^3\Sigma_{u,1}^+$ state in some detail. We select this $\Omega = 1$ state because it is the major channel (≈ 73 %).

In Fig. 3.1 we show the ABO potentials $\epsilon_{L|\Lambda|S}(R)$ as well as the Hund's case (c) potentials, i.e., the eigenvalues of the total Hamiltonian $\hat{H}(R)$, for all $\Omega = 1$ states. At small R the Coulomb interaction dominates the SO coupling, and the two sets of curves nearly coincide and can be labeled with Hund's case (a) quantum numbers. For large R only the spin-orbit interaction lifts the degeneracy of the states and the Hund's case (c) curves approach the

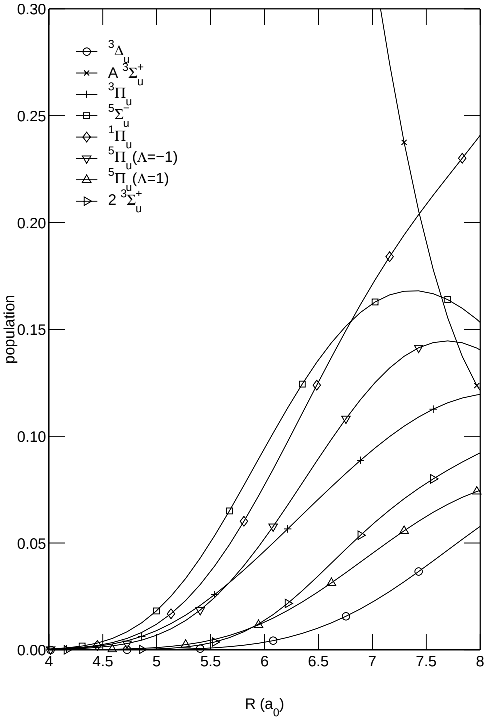

Figure 3.2: Populations of the ABO states in the electronic wave function for semiclassical dissociation of initial state $A^3\Sigma^+_{u,1}$*, at* λ *= 226 nm.*

asymptotic values given in Eq. (3.8) while the ABO potentials all go to zero (with our choice of the zero of energy). Note that the ABO curves, in contrast with the Hund's case (c) curves, may cross when they have the same Ω. The first crossing, around $R = 4.75$ a$_0$, involves the $A^3\Sigma^+_{u,1}$ and the $^3\Pi_{u,1}$ state.

In Fig. 3.2 we show the contributions of the ABO states to the electronic wave function as obtained from the semiclassical calculation for the dissociation of the $A^3\Sigma^+_u$ state at 226 nm. For $R < 4.5$ a$_0$ the wave function remains in the initially excited state. We observe that states that have a nonzero spin-orbit matrix element with the $A^3\Sigma^+_u$ state become populated before the other states [$A'\ ^3\Delta_{u,1}$ and $2^3\Sigma^+_{u,1}$] mix in by a two-step process, as expected. At large R the populations of the ABO states do not reach an asymptotic value, but keep oscillating because the ABO states are not eigenfunctions of $\hat{H}(R)$. In order to analyze at what value of R the fine-structure branching ratios reach their asymptotic value, we plot in Fig. 3.3 the populations of the asymptotic Hund's case (c) basis functions $|j_a\omega_a j_b\omega_b\rangle_u$. Note that we summed the populations of states with the same (j_a, j_b) quantum numbers. To give an indication of the

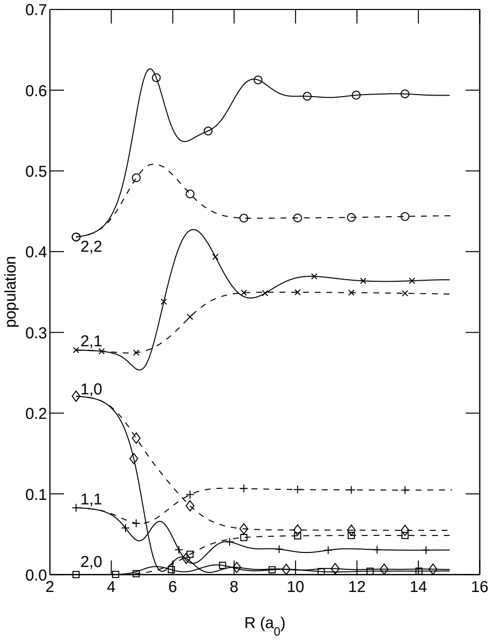

Figure 3.3: The electronic wave function for semiclassical dissociation of $A^3\Sigma^+_{u,1}$*, at* $\lambda = 236$ *nm (solid lines) and* $\lambda = 204$ *nm (dashed lines). Plotted are populations of asymptotic Hund's case (c) basis functions* $|j_a\omega_a j_b\omega_b\rangle_u$*, where populations of states with the same* j_a, j_b *value were added.*

effect of the photodissociation energy we show curves corresponding to $\lambda =$ 236 nm (solid lines) and $\lambda = 204$ nm (dashed lines). At low energy we see a higher population of states with $(j_a, j_b) = (2, 2)$ and a lower population of states yielding $j = 0$ fragments. This is expected since the low energy adiabatic limit predicts purely $j = 2$ fragments.

The effect of the nonadiabatic radial derivative coupling is most easily visualized for the extended diabatic model, where it is the *only* coupling. Fig. 3.4 shows how the $2^3\Sigma^+_u$ state is populated as a function of R for a range of photodissociation wavelengths. Although the coupling has its maximum around 6 a$_0$ (see Fig. 6 in paper I) the transitions mostly occur at somewhat larger R because the energy gap between the $A^3\Sigma^+_u$ and the $2^3\Sigma^+_u$ states is smaller there. The $E \to \infty$ limit is computed from Eq. (3.17). Note that at $\lambda = 204$ nm, this limit is not yet reached. In the semiclassical calculations the effect of the radial derivative coupling is expected to be less important because spin-orbit coupling reduces the population of the $A^3\Sigma^+_u$ state. Neglecting the radial derivative coupling in the semiclassical calculation changes the fine-structure branching ratios by at most 0.03 and the anisotropy parameters by

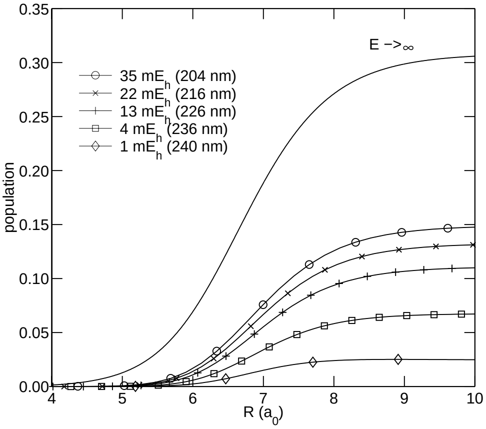

Figure 3.4: Population of the $2^3\Sigma_u^+$ *ABO basis state* $(|(2)01\Sigma; R\rangle)$ *for dissociation of* $A^3\Sigma_u^+$ $(|(0)01\Sigma; R\rangle)$ *in the extended diabatic model, at different dissociation energies (laser wavelengths).*

at most 0.05.

The populations $P_j^{i\Omega}$ and the alignment parameters $\rho_0^{(k)}(i\Omega; j)$ are given in Tables 3.3 and 3.4, respectively, for all Herzberg states separately. Semiclassical results are given for five energies, including the three energies $E = 4.325$, 12.87, and 34.61 mE$_h$, that correspond to the three wavelengths $\lambda = 236, 226$, and 204 nm for which experiments were done. We also give the results for the adiabatic model and for the extended diabatic model at $\lambda = 204$ nm. Note that for most Herzberg states the semiclassical results for the populations are between the adiabatic and diabatic limits. The exceptions are $A^3\Sigma_{u,0}^+$ and $A'\ ^3\Delta_{u,2}$ states. For the latter state, the $j = 2$ population actually has a minimum around $E = 6$ mE$_h$. In the adiabatic model only the $j = 2$ state is populated. In the semiclassical calculation for $E = 1.108$ mE$_h$ ($\lambda = 240$ nm) however only the $c^1\Sigma_{u,0}^-$ and $A'\ ^3\Delta_{u,3}$ have reached a $j = 2$ population of more than about 90 %, whereas the other states still have substantial contributions for $j < 2$. At $E = 34.61$ mE$_h$ the populations are generally quite close to the diabatic limit, with the largest absolute difference of 0.13 for the $j = 2$ population for the $c^1\Sigma_u^-$ state. Note however that the relative differences with the diabatic limit for the $j = 0$ populations can be about a factor of 2, e.g. for the $A^3\Sigma_{u,1}^+$ and $c^1\Sigma_u^-$ states.

By definition $\rho_0^{(0)}(i\Omega; j) = 1/\sqrt{2j+1}$ so this parameter is not listed in Table 3.4. We recall from Section 3.2.3 the ranges for the other parameters: –0.816 $\leq \rho_0^{(2)}(i\Omega; j = 1) \leq 0.408$, –0.535 $\leq \rho_0^{(2)}(i\Omega; j = 2) \leq 0.535$, and –0.478 $\leq \rho_0^{(4)}(i\Omega; j = 2) \leq 0.717$. Note that $\rho_0^{(2)}(\ A'\ ^3\Delta_{u,3}\ ; j = 1)$ is equal to its

Table 3.3: Populations $P_j^{i\Omega}(E)$ for the extended diabatic model at the highest energy (34.61 mE_h), for the semiclassical calculation at several energies, and for the adiabatic limit, which is not energy dependent.

			Semiclassical					Diabatic
			$E = 1.108$	4.325	12.87	22.20	34.61	34.61mE_h
State	j	Adiabatic	$\lambda = 240$	236	226	216	204	204nm
$A^3\Sigma^+_{u,1}$	2	1	0.778	0.744	0.692	0.663	0.642	0.547
	1	0	0.216	0.240	0.273	0.292	0.306	0.359
	0	0	0.005	0.016	0.035	0.045	0.052	0.094
$A^3\Sigma^+_{u,0^-}$	2	1	0.591	0.557	0.490	0.472	0.472	0.573
	1	0	0.369	0.330	0.337	0.339	0.335	0.282
	0	0	0.040	0.113	0.173	0.189	0.193	0.145
$c^1\Sigma^-_{u,0^-}$	2	1	0.948	0.899	0.820	0.771	0.732	0.593
	1	0	0.051	0.095	0.159	0.196	0.223	0.311
	0	0	0.001	0.005	0.021	0.033	0.045	0.096
$A'\,^3\Delta_{u,1}$	2	1	0.640	0.538	0.439	0.405	0.385	0.334
	1	0	0.337	0.404	0.468	0.485	0.493	0.500
	0	0	0.023	0.058	0.092	0.110	0.122	0.166
$A'\,^3\Delta_{u,2}$	2	1	0.552	0.532	0.549	0.559	0.567	0.584
	1	0	0.365	0.334	0.281	0.266	0.258	0.250
	0	0	0.083	0.134	0.170	0.175	0.175	0.166
$A'\,^3\Delta_{u,3}$	2	1	0.896	0.842	0.807	0.795	0.788	0.751
	1	0	0.104	0.158	0.193	0.205	0.212	0.249
	0	0	0	0	0	0	0	0

Table 3.4: Alignment parameters $\rho_0^{(k)}(i\Omega;j)(E)$ *for the extended diabatic model at the highest energy (34.61* mE_h*), for the semiclassical calculation at several energies, and for the adiabatic limit, which is not energy dependent. The parameters with* $k=0$ *are* $1/\sqrt{2j+1}$ *by definition, those are not listed.*

			Semiclassical					Diabatic
State	(j,k)	Adiabatic	$E=1.108$	4.325	12.87	22.20	34.61	$34.61\mathrm{mE}_h$
$A^3\Sigma^+_{u,1}$	(1,2)		−0.272	0.083	0.095	0.068	0.047	0.037
	(2,2)	−0.3859	−0.282	−0.153	−0.073	−0.041	−0.021	0.013
	(2,4)	0.1111	0.033	0.049	0.010	−0.014	−0.033	−0.067
$A^3\Sigma^+_{u,0^-}$	(1,2)		0.122	−0.214	−0.498	−0.569	−0.610	−0.538
	(2,2)	0.3129	0.094	0.137	0.189	0.219	0.243	0.309
	(2,4)	−0.0457	−0.099	−0.039	0.078	0.127	0.153	0.128
$c^1\Sigma^-_{u,0^-}$	(1,2)		0.195	0.212	0.165	0.113	0.060	−0.162
	(2,2)	−0.0457	0.072	0.171	0.225	0.242	0.252	0.221
	(2,4)	−0.3129	−0.213	−0.136	−0.093	−0.074	−0.057	−0.000
$A'\ ^3\Delta_{u,1}$	(1,2)		−0.244	−0.194	−0.198	−0.201	−0.202	−0.205
	(2,2)	0.1186	−0.096	−0.167	−0.227	−0.310	−0.327	−0.334
	(2,4)	−0.1709	−0.088	−0.061	−0.055	−0.069	−0.086	−0.178
$A'\ ^3\Delta_{u,2}$	(1,2)		−0.307	−0.424	−0.638	−0.719	−0.762	−0.816
	(2,2)	0.000	0.214	0.309	0.380	0.391	0.392	0.381
	(2,4)	0.4183	0.012	0.035	0.128	0.160	0.178	0.205
$A'\ ^3\Delta_{u,3}$	(1,2)		0.408	0.408	0.408	0.408	0.408	0.408
	(2,2)	0.1336	0.180	0.209	0.230	0.237	0.242	0.266
	(2,4)	−0.1793	−0.145	−0.123	−0.108	−0.102	−0.099	−0.080

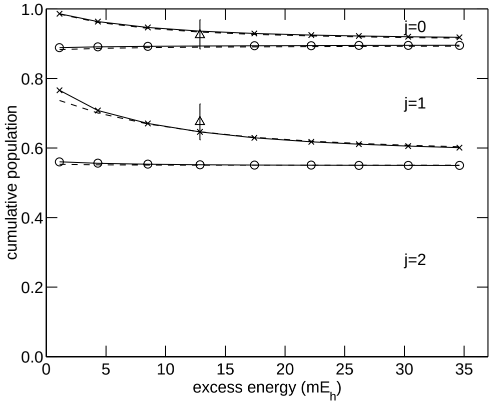

Figure 3.5: Cumulative plot of distribution over atomic j levels. The diabatic model is marked ∘. *The experimental data are given with* △ *marks and error bars. The semiclassical results are marked* ×. *The dashed lines represent the fine-structure branching ratios r_j, the solid lines represent the intensity ratios of the ion images, $r_j^{\mathrm{obs}}(E)$.*

maximum value of 0.408 for all energies. This can be easily understood since a $j_a = 1$ atom arising from an $\Omega = 3$ state must necessarily have $\omega_a = 1$, because $\omega_a + \omega_b = \Omega$ and $|\omega_b| \leq 2$. We observe that in general the largest variations in the polarization parameters occur for low energies. The atomic polarizations have not yet been measured directly. Experimental determination of these parameters would be a welcome extra test of the present calculations. We only list the $\rho_0^{(4)}(i\Omega; j)$ parameters for completeness, they do not play a role in the present two-photon detection scheme.

We compute the fine-structure branching ratios for the photodissociation of O_2 $[r_j(E)]$ by combining the branching ratios for excitation of the different Herzberg states ($r_{i\Omega}$) given in Table 3.2 with the population parameters $P_j^{i\Omega}$ according to Eq. (3.35). The energy dependent results for the semiclassical as well as the extended diabatic calculations are shown in Fig. 3.5. The intensity ratios that may be determined from the ion images formally depend on the polarization of the atoms according to Eq. (3.33). In Fig. 3.5 we see that only for the lowest energy in the semiclassical calculation there is a small difference between the intensity ratios in the images (solid lines) and the branching ratios (dashed lines). Experimentally determined intensity ratios are only available for $\lambda = 226$ nm. We find that the semiclassical results lie within the experimental error bars, while the extended diabatic model is clearly outside the error bars. Note that the semiclassical results are between the adiabatic (100 % $j = 2$) and diabatic limits for the full energy range considered.

In Figs. 3.6, 3.7, and 3.8 we compare the calculated anisotropy parame-

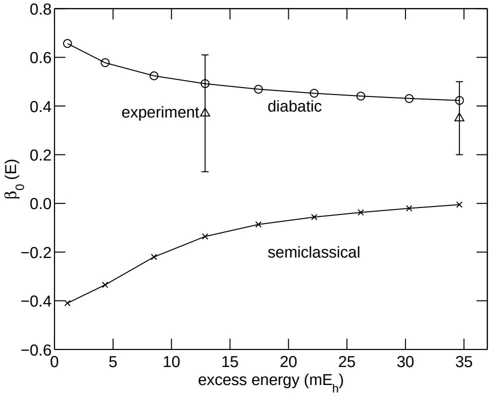

Figure 3.6: The anisotropy parameter $\beta_0(E)$. The markers have the same meaning as in Fig 3.5.

ters with experiment for, respectively, $j = 0, 1$, and 2 atomic fragments. For $j = 1$ and $j = 2$ polarization of the atoms may cause a difference between the anisotropy of the atomic fragment distribution [$\beta_j(E)$, the dashed lines in the figures] and the experimentally determined anisotropy parameters $\beta_j^{\rm obs}(E)$ of the ion images [solid lines in the figures]. Note that the largest polarization effects are predicted for low energies. For $j = 2$ and $j = 1$ the semiclassical results are in better agreement with experiment than the extended diabatic model. For $j = 2$ we also have results for the adiabatic model. For this model

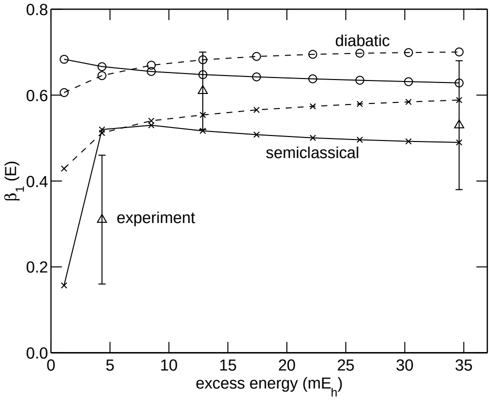

Figure 3.7: The parameters $\beta_1(E)$ (dashed) and $\beta_1^{\rm obs}(E)$ (solid). The semiclassical calculation is marked $\times$, the diabatic model results are marked $\circ$, and the experiment is marked with $\triangle$ and error bars.

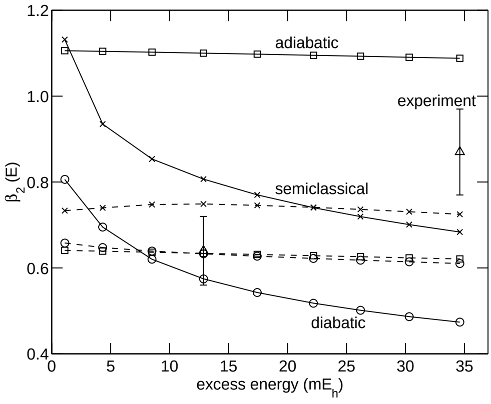

Figure 3.8: The parameters $\beta_2(E)$ and $\beta_2^{\mathrm{obs}}(E)$. The adiabatic model results are marked with squares, the other markers have the same meaning as in Fig 3.7.

we find a large polarization effect, just as for the semiclassical calculations at low energy. The largest deviations between the semiclassical calculation and experiment occur for $j = 0$ (Fig. 3.6). This is somewhat surprising since in this case there are no polarization effects, so the branching ratios determine the anisotropy parameters. However, in Fig. 3.5 we already saw that the semiclassical results are in good agreement with the experimentally determined branching ratios at $\lambda = 226$ nm. Clearly, additional independent experimental data on the branching ratios and anisotropy parameters would be most welcome to further test our understanding of the photodissociation dynamics of O_2 in the Herzberg continuum. Furthermore, note that we took the Herzberg excitation branching ratios and anisotropy parameters from the experimental paper.[3] These values were determined from extrapolation of spectroscopic data. However, the R dependence of the transition moments that was used in the excitation model in Ref. 3 is not in full agreement with *ab initio* calculations.[3,23]

3.4 Conclusion

Several electronic states contribute to the photodissociation of O_2 in the Herzberg continuum. The photodissociation dynamics determines the fine-structure branching ratios for these states. This is reflected in the anisotropy of the fine-structure resolved fragment distributions. In paper I we computed potentials, spin-orbit and radial derivative couplings for electronic wave functions that were carefully constructed to have the correct long range behavior. In this paper we present the results of semiclassical dynamics calculations, which apply these potentials and couplings. We compare the calculated branching ratios and anisotropy parameters to experimental results. In order to investigate the adiabaticity of the dissociation we also present results for the limiting adiabatic and diabatic models.

We find that at the lowest energy for which experimental data ($\lambda = 236$ nm) are available the dynamics is still not fully adiabatic and at the highest energy ($\lambda = 204$ nm) it is not yet fully diabatic. The dynamics is mainly determined by transitions that occur between 4.5 and 9 a_0, where the spin-orbit interaction becomes large compared to the separation of the ABO potentials. We also considered the effect of the radial derivative coupling between the $A^3\Sigma_u^+$ and $2^3\Sigma_u^+$ states. In the hypothetical infinite energy limit this coupling causes a $2^3\Sigma_u^+$ population of about 30 %. In the extended diabatic limit we ignore the SO coupling and only include the radial derivative coupling. We find that for $\lambda = 204$ nm the $2^3\Sigma_u^+$ state is still only populated by about 15 %. In the semiclassical calculations the $A^3\Sigma_u^+$ state becomes (partly) depopulated through spin-orbit coupling before the radial derivative coupling reaches its maximum, hence the effect on the calculated images is small.

The 2+1 REMPI detection used in the experiment is sensitive to the polarization of the atoms. The semiclassical calculations show that strong polarization effects on the anisotropy of the ion images can be expected for low energies. Formally, polarization of the atoms also affects the determination of the fine-structure branching ratios from the ion images, but we find that this effect is almost negligible.

Generally, there is reasonable agreement between the semiclassical calculations and experiment. The largest difference between the semiclassical calculations and experiment occurs for the anisotropies in the $j = 0$ images. In the present study we took the Herzberg excitation branching ratios from literature results which mainly rely on experimental data. We believe that additional *ab initio* calculations of the transition moments may help to resolve the remaining differences. Also, experimental determination of the anisotropy parameters with smaller error bars and a direct determination of the polarization of the atoms, particularly at low energies would be most welcome.

Acknowledgments

The authors thank Ad van der Avoird and Paul E. S. Wormer for useful discussions and for carefully reading the manuscript. This research has been financially supported by the Council for Chemical Sciences of the Netherlands Organization for Scientific Research (CW-NWO).

Appendix: Derivation of detection angular sensitivity

The geometrical factors $I_k(j)$ for the REMPI detection are derived from the spherical components of the two-photon excitation intensity operator. Following Ref. 24 we write the $q = 0$ spherical components of the geometrical factors of a general two-photon transition in the case of linearly polarized light as

$$I_k^{\mathrm{SF}}(j_i, j_f) = \sum_m (-1)^{j_i - m}\sqrt{2k+1}\begin{pmatrix} j_i & k & j_i \\ -m & 0 & m \end{pmatrix} \times \left| \sum_{j_e} (-1)^{j_f + j_e} \begin{pmatrix} j_f & 1 & j_e \\ -m & 0 & m \end{pmatrix} \begin{pmatrix} j_e & 1 & j_i \\ -m & 0 & m \end{pmatrix} R(j_e) \right|^2 , \quad (3.37)$$

where

$$R(j_e) = \sum_{n_e} \frac{\langle n_f j_f || r^{(1)} || n_e j_e \rangle \langle n_e j_e || r^{(1)} || n_i j_i \rangle}{E_{n_e} - E_{n_i} - h\nu + i(\Gamma_e/2)} . \quad (3.38)$$

The transition is from initial state $|n_i j_i m\rangle$ to final state $|n_f j_f m\rangle$, through intermediate states $|n_e j_e m\rangle$, where j_i, j_e, j_f denote the total angular momentum, m denotes the projection of the angular momentum on the space fixed (SF) axis of laser polarization, and n_i, n_e, n_f denote all other quantum numbers of initial, intermediate, and final state, respectively. The symbols $\langle n_f j_f || r^{(1)} || n_e j_e \rangle$ and $\langle n_e j_e || r^{(1)} || n_i j_i \rangle$ represent the reduced matrix elements of the transition dipole $r_m^{(1)}$, E_{n_e} and E_{n_i} are the energies of intermediate and initial state, ν is the frequency of the detection laser, and Γ_e is the homogeneous linewidth. The factors $I_k^{\mathrm{SF}}(j_i, j_f)$ are called P_k by Mo *et al.* Components with $q \neq 0$ are zero for a two-photon absorption process.

Experiments[25] and theoretical calculations[26] have shown that the intermediate state $2s^2 2p^3 3s\,^3\mathrm{S}^0$ contributes about 97% of the total two-photon excitation line strength in the (2+1) REMPI detection of $\mathrm{O}(^3P_j)$ at 226 nm. When we neglect possible other intermediate states, the only possible value for j_e equals 1, and the summation over n_e drops out of the reduced matrix element factor $R(j_e)$. Then $R(j_e)$ is the same for all components of one transition $|n_f j_f\rangle \leftarrow |n_i j_i\rangle$. Since we are only interested in relative intensities, this factor can be divided out. We find

$$I_k^{\mathrm{SF}}(j_i, j_f) = \sum_m (-1)^{j_i - m}\sqrt{2k+1}\begin{pmatrix} j_i & k & j_i \\ -m & 0 & m \end{pmatrix} \times \begin{pmatrix} j_f & 1 & j_e \\ -m & 0 & m \end{pmatrix}^2 \begin{pmatrix} j_e & 1 & j_i \\ -m & 0 & m \end{pmatrix}^2 . \quad (3.39)$$

In the experiment, the final state is not resolved, and we have to sum over all possible final states. Using the single-intermediate-state model the branching

Table 3.5: *Branching ratios* $r^{\mathrm{at}}(j_f \leftarrow j_i)$ *for the REMPI transition* $\mathrm{O}(2p^3(^4S)3p\,^3P_{j_f}) \leftarrow \mathrm{O}(2p^4\,^3P_{j_i})$ *via the* $2p^33s\,^3S^0$ *intermediate state.*

j_i	j_f	$r^{\mathrm{at}}(j_f \leftarrow j_i)$
0	0	1/3
0	1	0
0	2	2/3
1	0	0
1	1	1/2
1	2	1/2
2	0	2/15
2	1	3/10
2	2	17/30

ratios $r^{\mathrm{at}}(j_f \leftarrow j_i)$ from one given j_i to the three possible final states j_f are also given by Bischel.[25] These values are are given in Table 3.5. We then finally find

$$I_k(j) = \sum_{j_f=0}^{2} r^{\mathrm{at}}(j_f \leftarrow j) I_k^{\mathrm{SF}}(j, j_f)/I_0^{\mathrm{SF}}(j, j_f). \tag{3.40}$$

Bibliography

[1] H. M. Lambert, P. J. Dagdigian, and M. H. Alexander, J. Chem. Phys. **108**, 4460 (1998).

[2] G. Parlant and D. R. Yarkony, J. Chem. Phys. **110**, 363 (1999).

[3] B. Buijsse, W. J. van der Zande, A. T. J. B. Eppink, D. H. Parker, B. R. Lewis, and S. T. Gibson, J. Chem. Phys. **108**, 7229 (1998).

[4] A. T. J. B. Eppink and D. H. Parker, Rev. Sci. Instrum. **68**, 3477 (1997).

[5] M. C. G. N. van Vroonhoven and G. C. Groenenboom, J. Chem. Phys. **116**, 1954 (2002), Chapter 2 of this thesis.

[6] S. J. Singer, K. F. Freed, and Y. B. Band, Adv. Chem. Phys. **61**, 1 (1985).

[7] Y.-L. Huang and R. J. Gordon, J. Chem. Phys. **94**, 2640 (1991).

[8] B. Zygelman, A. Dalgarno, and R. D. Sharma, Phys. Rev. A **49**, 2587 (1994).

[9] S. J. Singer, K. F. Freed, and Y. B. Band, J. Chem. Phys. **79**, 6060 (1983).

[10] J. B. Delos, Rev. Mod. Phys. **53**, 287 (1981).

[11] C. E. Moore, *Atomic energy levels as derived from the analysis of optical spectra, Volume I*, Number 35 in National Sandards Reference Data Series, National Bureau of Standards, Washington D.C., 1971.

[12] J. B. Delos, W. R. Thorson, and S. K. Knudson, Phys. Rev. A **6**, 709 (1972).

[13] J. B. Delos and W. R. Thorson, Phys. Rev. A **6**, 720 (1972).

[14] P. C. Cosby and D. L. Huestis, J. Chem. Phys. **97**, 6108 (1992).

[15] The MATLAB computer linear algebra system is available from The Mathworks, Inc., accessible online at http://www.mathworks.com/.

[16] C. H. Greene and R. N. Zare, Annu. Rev. Phys. Chem. **33**, 119 (1982).

[17] L. D. A. Siebeles, M. Glass-Maujean, O. S. Vasyutinskii, J. A. Beswick, and O. Roncero, J. Chem. Phys. **100**, 3610 (1994).

[18] K. Blum, *Density matrix theory and applications*, Physics of atoms and molecules series, Plenum Press, New York and London, 1981, Chapter 4 deals with the irreducible components of the density matrix.

[19] R. N. Zare, *Angular momentum*, Wiley, New York, 1988.

[20] A. J. Orr-Ewing and R. N. Zare, Annu. Rev. Phys. Chem. **45**, 315 (1994).

[21] Y. Mo and T. Suzuki, J. Chem. Phys. **109**, 4691 (1998).

[22] C. M. L. Kerr and J. K. G. Watson, Can. J. Phys. **64**, 36 (1986).

[23] R. Klotz and S. D. Peyerimhoff, Mol. Phys. **57**, 573 (1986).

[24] Y. Mo, H. Katayanagi, M. C. Heaven, and T. Suzuki, Phys. Rev. Lett. **77**, 830 (1996).

[25] W. K. Bischel, B. E. Perry, and D. R. Crosley, Applied Optics **21**, 1419 (1982).

[26] M. S. Pindzola, Phys. Rev. A **17**, 1021 (1978).

Chapter 4

Reassignment of the O_2 *spectrum just below dissociation threshold based on ab initio calculations*

Abstract

Vibrational Herzberg bands of the O_2 molecule just below its first $O(^3P)$ + $O(^3P)$ dissociation limit are since long known to be perturbed. Jenouvrier *et al.* [J. Mol. Spectr. **198**, 136 (1999)] assigned the cause of the perturbations to five vibrational levels supported by the shallow minimum in the $1^3\Pi_u$ potential energy curve around 5.5 a_0. Using *ab initio* potential energy curves and spin-orbit couplings from previous work [J. Chem. Phys. **116**, 1954 (2002)] we present a full quantum calculation of all ungerade rotation-vibration-electronic states of oxygen just below the dissociation threshold, through a total angular momentum quantum number of $J = 19$. This calculation shows that the original assignment, based on a Hund's case (a) model of a regular $1^3\Pi_u$ multiplet was not correct. Based on our calculation we present a new assignment of the perturbing states: $1^3\Pi_{u,\Omega=2}(v{=}0)$, $1^3\Pi_{u,1}(0)$, $1^3\Pi_{u,2}(1)$, $1^3\Pi_{u,1}(1)$, and $1^3\Pi_{u,0^-}(0)$ in order of ascending term values. We show the new assignment to be consistent with experimental data and we also propose new spectroscopic parameters for the perturbing states.

4.1 Introduction

Eight ungerade states of O_2 correlate with its lowest dissociation limit $O(^3P)$ + $O(^3P)$. Three of these states are very well characterized by extensive spectroscopic studies[1–11] of the so-called Herzberg bands, bands corresponding to transitions from the $X^3\Sigma_g^-$ ground state to the $A^3\Sigma_u^+$(Herzberg I),

$c^1\Sigma_u^-$(Herzberg II), and $A'\ ^3\Delta_u$(Herzberg III) states. The other five ungerade states, $1^3\Pi_u$, $1^5\Sigma_u^-$, $1^5\Pi_u$, $1^1\Pi_u$, and $2^3\Sigma_u^+$, are difficult to detect because these potentials have only shallow minima at large internuclear separations ($r > 5$ a_0), which leads to very unfavorable Franck-Condon overlap with the ground state that has an $r_0 = 2.29$ a_0. Still, the spin-orbit interaction between all these states affects the $O(^3P_j)$ fine-structure branching ratios for photodissociation of O_2 in the Herzberg continuum.[12, 13] These interactions (together with spin-orbit interactions amongst the gerade states) are also responsible for the excitation and quenching of the fine-structure levels in collisions among oxygen atoms.[14, 15] A quantitative understanding of processes affecting fine-structure level populations is very important in atmospheric chemistry.[16] Clearly *ab initio* calculations are a valuable source of information about these potentials and couplings. However, the open shell character of these states complicates the proper treatment of the electron correlation and the basis set superposition error.[12] Thus, spectroscopic information on states in the so called recoupling region ($r \approx 4 - 7$ a_0) can provide useful benchmark information.

A glimpse of the spectroscopy of the weakly bound states is provided by perturbations in the Herzberg bands that occur less than about 110 cm^{-1} below the dissociation limit. The weakly bound states cause a characteristic pattern of deviations from straight lines which emerge when the term values of the observed Herzberg levels are plotted as a function of $J(J+1)$. Perturbations in the $v = 11$ band of the $A^3\Sigma_u^+$ state were first noted by Herzberg[2] in 1952. In 1986 Borrell *et al.*[5] report perturbations in the $N = 9$, 11, and 13 rotational levels of this band. They suggest, based on potentials of Saxon and Liu,[17] that the $^5\Sigma_u^-$ state is the perturber. In 1991, Partridge *et al.*[18] perform more advanced *ab initio* calculations on these states and propose the $1^3\Pi_u$ state, which has a deeper well, as the more likely candidate.

Jenouvrier *et al.*[19] recently remeasured the Herzberg bands with high resolution Fourier transform spectroscopy, identifying perturbations in the $A^3\Sigma_u^+$ (v=11), $c^1\Sigma_u^-$(v=18,19), and $A'\ ^3\Delta_{u,2}$(v=12) Herzberg bands. They attributed the perturbations to five $1^3\Pi_u$ levels. Assuming that this state is a regular Hund's case (a) multiplet, the perturbing levels were assigned to be $1^3\Pi_{u,\Omega=1}$ (v=0), $1^3\Pi_{u,2}(0)$, $1^3\Pi_{u,0}(1)$, $1^3\Pi_{u,1}(1)$, and $1^3\Pi_{u,2}(1)$ in order of ascending term values. It was assumed that the $1^3\Pi_{u,0}(0)$ level was the lowest $1^3\Pi_u$ level, although no corresponding perturbations were observed. In a previous paper,[12] which we will refer to as paper I, we calculated potential energy curves for all the electronic states involved at the internally contracted multireference configuration interaction level plus Pople size consistency correction, employing large basis sets. We also computed all diagonal and off-diagonal spin-orbit couplings amongst those states at the complete active space self consistent field level. We employed these *ab initio* data in a semiclassical study of the photodissociation of O_2 in the Herzberg continuum.[13]

In the present paper we use the *ab initio* results in a full quantum calculation of the spectroscopically observed levels of O_2 just below dissociation. Our calculations indicate that the major perturbing state, $1^3\Pi_u$, cannot be described by a regular Hund's case (a) state in the relevant region of $r \approx 5.5\ a_0$. In fact, the diagonal spin-orbit coupling matrix element is negative and spin-orbit couplings with other electronic states cannot be neglected. Although the electronic states are mixed we can assign the perturbing state and propose a new assignment by comparing the exact results with more approximate Hund's case (a) and (c) calculations. Many of the observed perturbations involve rather high rotational levels with J up to 17. Since in some cases the experimental $J = 0$ spectroscopic parameters depend on the assignment and the too simplistic Hund's case (a) model, we also performed calculations for the rotational levels that were actually observed. The pattern of perturbations depends very sensitively on the position of the $1^3\Pi_u(0,1)$ levels relative to the highly vibrationally excited Herzberg levels. To achieve better agreement with experiment we slightly scaled and adjusted our potentials. This scaling also allows us to draw a conclusion about the accuracy of the *ab initio* calculations of potential energy curves of and couplings between weakly interacting open shell atoms. We also use the plot of the term values versus $J(J+1)$ to extract the rotational constant of the "pure" $1^3\Pi_u$ level via a fit of the term values to a polynomial in $J(J+1)$. Since most $1^3\Pi_u$ levels are mixed with the Herzberg states, computation of the rotational constant as the expectation value of $1/2\mu r^2$ typically yields larger rotational constants.

The outline of this paper is as follows: In Sec. 4.2 we discuss the theoretical aspects of our calculation, the different parts of the Hamiltonian, and the basis functions used to expand the wave functions for the rotation-vibration-electronic (RVE) states. We also give some computational details on the discrete variable representation used for the radial nuclear motion. In Sec. 4.3, we discuss our potentials, the rotationless vibrational level positions in the Hund's case (a) and (c) approximations, and in a full coupled calculation, the scaling and adjusting of the potential energy curves, and finally in Sec. 4.3.6 the results including the full rotational part of the Hamiltonian. We give our conclusions in Sec. 4.4. In appendix 4.4 we define our basis functions, and derive their behavior under the parity operation. We also present a new derivation of the rotational kinetic energy matrix element which avoids the use of Hougen's isomorphic Hamiltonian.[20]

4.2 Theory

We compute RVE bound states of the O_2 molecule as eigenstates of the total Hamiltonian,

$$\hat{H} = \hat{H}_{\text{Coul}} + \hat{H}_{\text{SO}} + \hat{H}_{\text{vib}} + \hat{H}_{\text{rot}}, \tag{4.1}$$

where $\hat{H}_{\text{Coul}}$ is the usual Coulombic Hamiltonian in the clamped nuclei approximation and $\hat{H}_{\text{SO}}$ is the Breit-Pauli spin-orbit (SO) Hamiltonian. The nuclear radial kinetic energy is given by $\hat{H}_{\rm vib} = -(\hbar^2/2\mu)r^{-1}(\partial^2/\partial r^2)r$, where r is the interatomic distance and $\mu = 7.9975u$ is the reduced mass of ${}^{16}\mathrm{O}^{16}\mathrm{O}$. The rotational energy part $\hat{H}_{\rm rot}$ will be discussed below. The electronic adiabatic Born-Oppenheimer (ABO) wave functions, i.e., the eigenfunctions of $\hat{H}_{\rm Coul}$, are taken from paper I. The ABO states are pure Hund's case (a) wave functions and we denote them by $|(L)\Lambda S\Sigma; r\rangle$, where Λ and Σ are the projections, respectively, of the total electronic angular momentum ($\underline{\hat{L}}$) and the electron spin ($\underline{\hat{S}}$) on the internuclear axis. At large internuclear separation L is also a good quantum number and we use it to distinguish between the triplet states $A^3\Sigma_u^+(L=0)$ and $2^3\Sigma_u^+(L=2)$ of the same ($D_{\infty h}$) symmetry, as was explained in paper I.

In that paper we presented analytic fits to the ABO potentials $V_{L|\Lambda|S}(r)$ for different values of $L, |\Lambda|$, and S, which are defined by

$$V_{L|\Lambda|S}(r) = \langle (L)\Lambda S\Sigma; r|\hat{H}_{\rm Coul}|(L)\Lambda S\Sigma; r\rangle. \tag{4.2}$$

In addition, we computed r-dependent SO coupling matrix elements which, using the Wigner-Eckart theorem may be expressed as

$$\begin{aligned}&\langle (L)\Lambda S\Sigma; r|\hat{H}_{\rm SO}|(L')\Lambda' S'\Sigma'; r\rangle = \\ &\qquad (-1)^{S-\Sigma}\begin{pmatrix} S & 1 & S' \\ -\Sigma & (\Sigma-\Sigma') & \Sigma' \end{pmatrix}\langle (L)\Lambda S; r||\hat{H}_{\rm SO}(r)||(L')\Lambda' S'; r\rangle,\end{aligned} \tag{4.3}$$

where the quantity between large parentheses is a $3j$ symbol. Note that matrix elements are only nonzero when $\Delta\Omega = 0$, where $\Omega = \Lambda + \Sigma$. We provided fits to the 21 independent reduced SO matrix elements $\langle (L)\Lambda S; r||\hat{H}_{\rm SO}(r)||(L')\Lambda' S'; r\rangle$. We also presented in paper I the only nonvanishing radial derivative coupling matrix element amongst the eight ABO states, i.e., $\langle A^3\Sigma_u^+; r|\partial/\partial r|2^3\Sigma_u^+; r\rangle$. However, in semiclassical calculations on the photodissociation of O_2 we found that the effect of this coupling just above the dissociation limit is negligible and hence we do not include it in the present bound state calculations.

4.2.1 The rotational Hamiltonian

The rotational Hamiltonian is given by

$$\begin{aligned}\hat{H}_{\rm rot}^{\rm (exact)} = \frac{1}{2\mu r^2}\Big[&(\hat{J}^2 - \hat{J}_z^2) + (\hat{L}^2 - \hat{L}_z^2) + (\hat{S}^2 - \hat{S}_z^2) \\ &+ (\hat{L}^+\hat{S}^- + \hat{L}^-\hat{S}^+) - (\hat{L}^+\hat{J}^- + \hat{L}^-\hat{J}^+) - (\hat{S}^+\hat{J}^- + \hat{S}^-\hat{J}^+)\Big],\end{aligned} \tag{4.4}$$

in body-fixed operators, with $\underline{\hat{J}} = \underline{\hat{l}} + \underline{\hat{L}} + \underline{\hat{S}}$ and $\underline{\hat{l}}$ is the angular momentum associated with the rotation of the nuclei. In the Appendix we derive this Hamiltonian and its matrix elements. Asymptotically, the states we are considering are derived from coupling atomic P states and hence we have at most $L = 2$.

Furthermore, the expectation value of $\hat{L}^2$ in diatomic molecules is generally only weakly r-dependent for a given electronic state.[21] Hence the $\hat{L}^2$ term only induces a shift in the electronic energy in the order of $L(L+1)\hbar^2/2\mu r^2$ and we neglect this contribution. The $\hat{L}^{\pm}\hat{S}^{\mp}/2\mu r^2$ term couples states which are also coupled by SO coupling. However, because of the $1/2\mu r^2$ factor it is much smaller than the SO coupling (see paper I) and we neglect it. We also neglect the $\hat{L}^{\pm}\hat{J}^{\mp}$ term. This term couples states with different Λ values, so its main effect would be to give (small) perturbations for nearly degenerate states of different electronic character, e.g., near crossings. We do keep the $\hat{S}^{\pm}\hat{J}^{\mp}$ term, however, since it gives rise to intra state coupling. In particular, it couples the $\Omega = 0^-, \pm 1$ components of the $A^3\Sigma_u^+$ state. We will come back to this point in the discussion (Sec. 4.3.6).

To summarize we use a rotational Hamiltonian,

$$\hat{H}_{\mathrm{rot}} = \hat{H}_{\mathrm{rot}}^{(\mathrm{diag})} + \hat{H}_{\mathrm{rot}}^{(\mathrm{JS})} \tag{4.5}$$

with

$$\hat{H}_{\mathrm{rot}}^{(\mathrm{diag})} = \frac{1}{2\mu r^2}(\hat{J}^2 + \hat{S}^2 - \hat{J}_z^2 - \hat{L}_z^2 - \hat{S}_z^2) \tag{4.6}$$

and

$$\hat{H}_{\mathrm{rot}}^{(\mathrm{JS})} = \frac{-1}{2\mu r^2}(\hat{S}^+\hat{J}^- + \hat{S}^-\hat{J}^+). \tag{4.7}$$

In the Appendix we define electronic-rotation Hund's case (a) basis functions $|(L)\Lambda S\Sigma JM\Omega; r\rangle$, which are eigenfunctions of $\hat{H}_{\mathrm{Coul}}$ [see Eq. (4.1)] as well as $\hat{H}_{\mathrm{rot}}^{(\mathrm{diag})}$:

$$\left\{\hat{H}_{\mathrm{rot}}^{(\mathrm{diag})} - \left[J(J+1) + S(S+1) - \Omega^2 - \Lambda^2 - \Sigma^2\right]\right\} |(L)\Lambda S\Sigma JM\Omega; r\rangle = 0. \tag{4.8}$$

The matrix elements of $\hat{H}_{\mathrm{rot}}^{(\mathrm{JS})}$ follow directly from

$$\hat{S}^{\pm}\hat{J}^{\mp}|(L)\Lambda S\Sigma JM\Omega; r\rangle = c_{\pm}(J,\Omega)c_{\pm}(S,\Sigma)|(L)\Lambda S\Sigma \pm 1 JM\Omega \pm 1; r\rangle, \tag{4.9}$$

where $c_{\pm}(l,m) = [l(l+1) - m(m\pm 1)]^{1/2}$. In the Appendix we show that states of parity $p = \pm 1$, containing an ungerade electronic part, can be constructed as

$$|(L)\Lambda S\Sigma JM\Omega p; r\rangle = \frac{1}{\sqrt{2(1+\delta_{\Lambda,0}\delta_{\Sigma,0})}}[|(L)\Lambda S\Sigma JM\Omega; r\rangle - p(-1)^J|(L){-\Lambda} S{-\Sigma} JM{-\Omega}; r\rangle]. \tag{4.10}$$

4.2.2 Vibrational motion

The vibrational motion is treated by a sinc-function discrete variable representation[22] (sinc-DVR). The localized radial basis functions $\phi_n(r) = \langle r|n\rangle$ are associated with the grid points $r_n = r_0 + n\Delta$, where Δ is the grid spacing, via

$$\phi_n(r) = \frac{1}{\sqrt{\Delta}} \mathrm{sinc}\left(\pi \frac{r - r_n}{\Delta}\right), \tag{4.11}$$

where $\mathrm{sinc}(x) = \sin(x)/x$. These functions are orthonormal. The matrix elements of $\hat{H}_{\mathrm{vib}}$ are given by

$$\langle n|\hat{H}_{\mathrm{vib}}|n'\rangle = \begin{cases} \frac{\hbar^2}{2\mu}\frac{\pi^2}{3\Delta^2}, & n = n', \\ \frac{\hbar^2}{2\mu}\frac{2}{\Delta^2}\frac{(-1)^{n-n'}}{(n-n')^2}, & n \neq n'. \end{cases} \tag{4.12}$$

In a DVR all multiplicative operators are represented by diagonal matrices, so for the potential matrix elements we have

$$\langle n|V_{L|\Lambda|S}(r)|n'\rangle = \delta_{n,n'} V_{L|\Lambda|S}(r_n). \tag{4.13}$$

When evaluating rotational Hamiltonian matrix elements we may use

$$\langle n|\frac{1}{2\mu r^2}|n'\rangle = \delta_{n,n'} \frac{1}{2\mu r_n^2}. \tag{4.14}$$

Our RVE basis functions are products:

$$|(L)\Lambda S\Sigma JM\Omega n\rangle \equiv |(L)\Lambda S\Sigma JM\Omega; r\rangle \phi_n(r). \tag{4.15}$$

Since we neglect the electronic radial derivative coupling for Hund's case (a) basis functions, the vibrational Hamiltonian matrix is diagonal in all angular quantum numbers.

The total dimension of the basis that is required to converge all the states up to the dissociation limit is quite large (order 10^4). Therefore we follow a two-step procedure in which we exploit the fact that $\hat{H}_{\mathrm{rot}}^{(\mathrm{JS})}$ is the only term in the Hamiltonian that couples different Ω values. Thus for each value of Ω we compute and diagonalize the Hamiltonian matrix of

$$\hat{H}_0 = \hat{H}_{\mathrm{Coul}} + \hat{H}_{\mathrm{SO}} + \hat{H}_{\mathrm{vib}} + \hat{H}_{\mathrm{rot}}^{(\mathrm{diag})}. \tag{4.16}$$

Since $\hat{H}_0$ does not lift the degeneracy of odd and even parity states, we solve this problem in a parity unadapted basis with $\Omega \geq 0$ and we obtain the eigenfunctions as

$$|J\Omega v\rangle = \sum_{\substack{L\Lambda S\Sigma n \\ (\Lambda+\Sigma=\Omega)}} |(L)\Lambda S\Sigma JM\Omega n\rangle c_{L\Lambda S\Sigma n}^{(J\Omega v)}. \tag{4.17}$$

Note that for $\Omega = 0$ these eigenfunctions have an intrinsic parity. These functions are labeled $\Omega = 0^+$ for $p = +1$ or $\Omega = 0^-$ for $p = -1$. For $\Omega \neq 0$ we obtain parity adapted functions as

$$|J\Omega vp\rangle = \sum_{L\Lambda S\Sigma n} |(L)\Lambda S\Sigma JM\Omega pn\rangle c^{(J\Omega v)}_{L\Lambda S\Sigma n}. \tag{4.18}$$

We will use the conventional e/f parity label which corresponds to $p(-1)^J$ being even (e) and odd (f), respectively [see Eq. (4.10)]. For the $^{16}\mathrm{O}^{16}\mathrm{O}$ molecule one can show that the ungerade states must have odd parity ($p = -1$) (see the Appendix) and hence for even J only f states exist and for odd J only e states. Also note that 0_u^+ states must have e parity (and hence only occur for odd J) and 0_u^- states must have f parity (and hence occur only for even J).

In the final step of the calculation we select all (odd parity) eigenfunctions of $\hat{H}_0$ which have an energy E that is less than a certain threshold (E_{thresh}) and we use these functions as a basis to diagonalize the total Hamiltonian $\hat{H} = \hat{H}_0 + \hat{H}^{(JS)}_{\mathrm{rot}}$. Convergence of the calculations is checked by comparing the eigenvalues of $\hat{H}$ for several values of E_{thresh}.

For a given set of potential energy curves and spin-orbit couplings this procedure gives essentially exact results. However, since we cannot expect our *ab initio* calculations to be accurate to spectroscopic resolution, we need a thorough understanding of the spectrum in order to convincingly argue that a new assignment is called for. For this purpose we also report the results of approximate calculations in which we ignore the rotational part of the Hamiltonian ($\hat{H}_{\mathrm{rot}}$) and treat the molecule as either a pure Hund's case (a) or (c). In the Hund's case (a) calculations we use a Hamiltonian that includes $\hat{H}_{\mathrm{Coul}}$, $\hat{H}_{\mathrm{vib}}$, and the part of $\hat{H}_{\mathrm{SO}}$ that is diagonal in $(L), \Lambda$ (and Σ) [see Eq. (4.3)]. For the Hund's case (c) calculation we first diagonalize $\hat{H}_{\mathrm{Coul}} + \hat{H}_{\mathrm{SO}}$ in the electronic basis for each point of the radial grid to obtain Hund's case (c) potentials. Subsequently, we take into account the vibrational Hamiltonian in a Born-Oppenheimer type approximation, i.e., treating the system as a set of independent one-dimensional vibrational problems. To compare with these approximate calculations we also report a full calculation, with all of the electronic couplings included, but with neglect of the rotational Hamiltonian.

4.2.3 Convergence of the sinc-DVR

In the DVR calculation we employed a grid ranging from $r = 1.6$ a$_0$ to $r = 27$ a$_0$ with a grid spacing of $\Delta r = 0.045$ a$_0$. For the most strongly bound state in our study, the $c^1\Sigma_u^-$ state, which has a D_e of 8999 cm^{-1}, this Δr corresponds to 4 points per De Broglie wavelength, which we computed as $2\pi(2\mu D_e)^{-1/2}$. We checked that the convergence with respect to Δr of even the highest vibrational level ($v = 19$) of the c state is better than $4 \cdot 10^{-7}$ cm^{-1}.

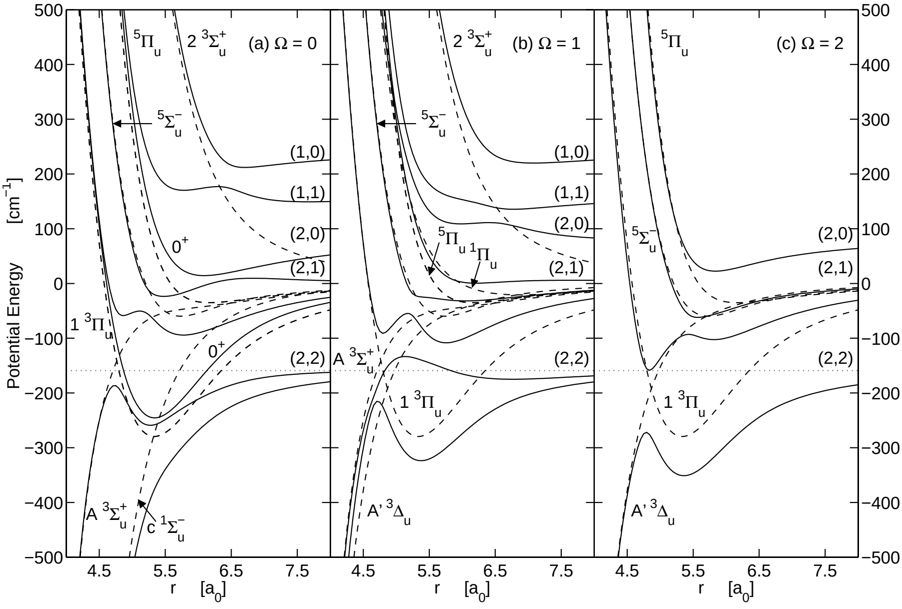

Figure 4.1: *Hund's case (a) (dashed lines) and (c) (solid lines) potential energy curves for $\Omega = 0$, 1, and 2 in part (a), (b), and (c) respectively. In part (a), case (c) $\Omega = 0^+$ curves have been marked 0^+, other (not marked) curves are 0^-. Hund's case (a) labels are formally only applicable to the dashed lines. The dotted line represents the $O(^3P_2) + O(^3P_2)$ dissociation limit, the different case (c) dissociation limits $O(^3P_{j_a}) + O(^3P_{j_b})$ are marked (j_a, j_b).*

The innermost point of the grid at 1.6 a_0 is chosen well into the repulsive region of all potentials involved and the results are fully converged with respect to this parameter. The very large grid size guarantees that even states located at only about 1 cm^{-1} below the dissociation limit are converged to better than 10^{-3} cm^{-1}.

4.3 Discussion

4.3.1 Potentials

In Fig. 4.1 we show the ABO potentials (the dashed lines) and the Hund's case (c) potentials (the solid lines) for $\Omega = 0, 1$, and 2. Details of the *ab initio* calculations of the potentials and the spin-orbit couplings used to construct the Hund's case (c) potentials, as well as the fits can be found in paper I. In Table 4.1 we report the spectroscopic parameters r_e, D_e, and ω_e for these potentials. The D_e is computed with respect to the $O(^3P_2)$+$O(^3P_2)$ dissociation limit

Table 4.1: Spectroscopic parameters D_e and ω_e (in cm^{-1}) and r_e (in a$_0$) for Hund's case (a) and (c) $1^3\Pi_{u,\Omega}$ potentials. For the case (c) potentials we also report the position r (in a$_0$) of the barrier between the inner and outer well and its height (in cm^{-1}) relative to the minimum of the outer well at $r = r_e$.

					Barrier	
case	Ω	r_e	D_e	ω_e	r	Height
(a)	0,1,2	5.33	120.4	92.5	–	–
(c)	0^-	5.27	100.0	91.7	4.73	73.0
(c)	1	5.37	164.6	83.0	4.72	109.0
(c)	2	5.36	192.0	85.4	4.79	79.4

(dotted line in Fig. 4.1) which lies 159 cm^{-1} below the asymptotic value of the ABO potentials. Note that in the Hund's case (c) description local minima of the $\Omega = 0^-, 1$, and 2 potentials correspond to the $1^3\Pi_{u,\Omega}$ states. In Table 4.1 we also give the barriers to the inner well which supports the Herzberg states.

In Fig. 4.2 we show the r-dependent diagonal spin-orbit matrix element $A_\Omega(r) = \langle 1^3\Pi_{u,\Omega}|\hat{H}_{\rm SO}|1^3\Pi_{u,\Omega}\rangle$. In a Hund's case (a) description the multiplet splittings of the $1^3\Pi_{u,\Omega}$ components is determined by $A_\Omega(r) = A(r)\Lambda\Sigma = A(r)(\Omega - 1)$. If the dominant configuration of the $1^3\Pi_u$ state is $1s^4\ 2s^4\ 2p\sigma_g^2\ 2p\pi_u^4\ 2p\pi_g\ 2p\sigma_u$ one expects a regular multiplet, i.e. $A(r) > 0$ (see Table 30 in Ref. 2). Figure 4.2 shows that for $r < 3.8$ a$_0$ this is the case. However, for larger internuclear separations, which are relevant for the $1^3\Pi_u$ state ($r \approx 5.5$ a$_0$), the *ab initio* calculation shows that such a simple description no longer

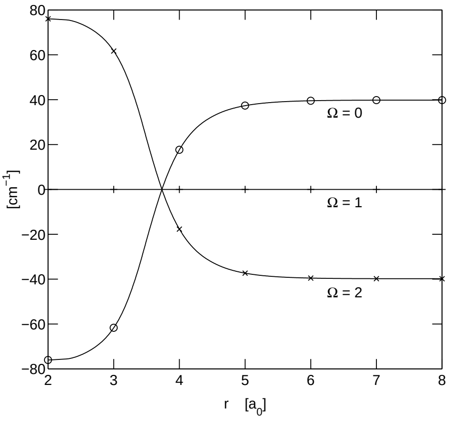

Figure 4.2: The diagonal spin-orbit matrix elements $\langle 1^3\Pi_{u,\Omega}|\hat{H}_{\rm SO}(r)|1^3\Pi_{u,\Omega}\rangle$, for Ω = 0, 1, and 2.

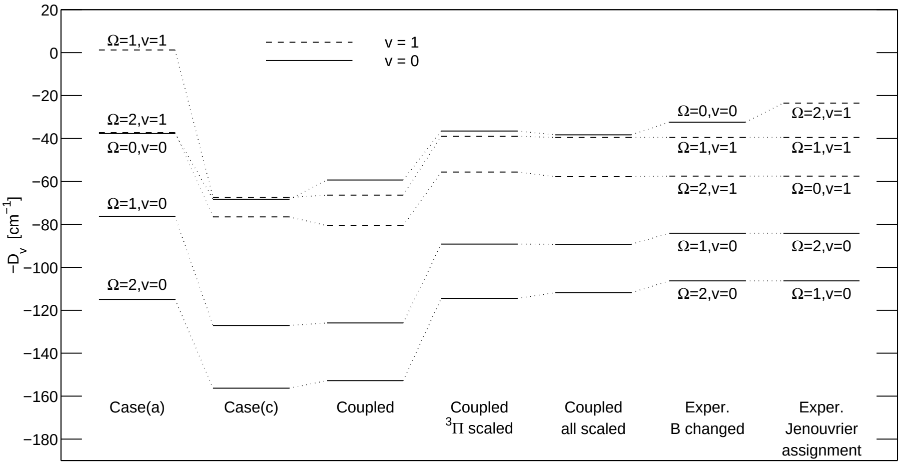

Figure 4.3: Bound state calculations for the $1^3\Pi_u$ vibrational levels where the rotational part of the Hamiltonian was ignored. From left to right approximate Hund's case (a), approximate Hund's case (c), full coupled calculation, coupled calculation with scaled $1^3\Pi_u$ potential, coupled calculation where both the $1^3\Pi_u$ and Herzberg potentials are scaled, experimental results, with our model rotational constant for the highest level (see text) and our new assignment, and original experimental results with original assignment.

applies.

4.3.2 Rotationless levels

In Fig. 4.3 we show the results of all our bound state calculations in which the rotational part of the Hamiltonian was ignored. At the right hand side of the figure we show the levels observed by Jenouvrier *et al.* and the original assignment.

case (a) When we treat the $1^3\Pi_u$ state in the Hund's case (a) approximation described in the theory section we find the levels shown in the first column of Fig. 4.3. Note that the zero of energy in this plot corresponds to the $O(^3P_2)$ + $O(^3P_2)$ dissociation limit and hence these approximate Hund's case (a) "bound" levels may have a positive energy up to 159 cm^{-1}. As expected, we find an inverted multiplet in the Hund's case (a) approximation.

case (c) We also approximated the bound levels by solving one-dimensional vibrational problems employing the Hund's case (c) potentials. The results are shown in the second column in Fig. 4.3. Note that the Ω components

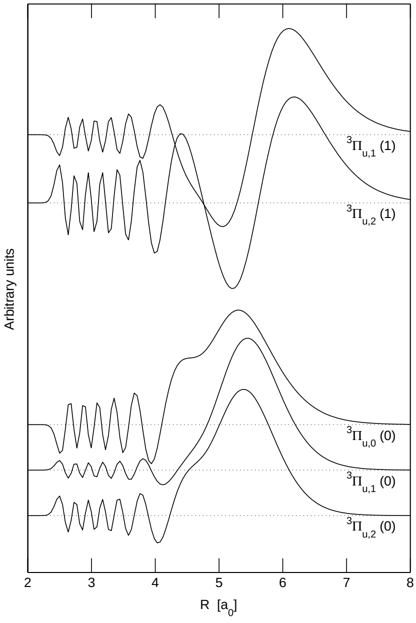

Figure 4.4: Vibrational wave functions for the $1^3\Pi_{u,\Omega}(v)$ *levels calculated in the Hund's case (c) approximation.*

of the $1^3\Pi_{u,\Omega}$ are not equally spaced, in contrast with the Hund's case (a) description. In the Hund's case (c) description the $1^3\Pi_u(v)$ states can mix with the Herzberg states by tunneling through the barrier between the inner and outer wells in the potentials. In Fig. 4.4 we plot the vibrational wave functions corresponding to the five case (c) energy levels shown in Fig. 4.3. Clearly the $v = 0$ states are sufficiently well localized in the outer well to allow an unambiguous assignment. The $1^3\Pi_{u,1}(1)$ level lies also below the ($\Omega = 1$) barrier. The $\Omega = 2$ barrier is lower and the $1^3\Pi_{u,2}(1)$ level lies above this barrier, and is rather strongly mixed with the $A'\ ^3\Delta_{u,2}(12)$ level.

Coupled calculation In the third column of Fig. 4.3 we show the results of a fully coupled calculation. Since we still left out the rotational part of the Hamiltonian, Ω is a good quantum number. These levels are computed by taking all electronic Hund's case (a) basis functions for a specific value of Ω [see Eqs. (4.2) and (4.3)], combining them with the sinc-DVR basis functions [Eq. (4.11)] to describe the vibrational motion [Eq. (4.12)] and diagonalizing $\hat{H}_{\text{Coul}} + \hat{H}_{\text{SO}} + \hat{H}_{\text{vib}}$ in this basis. Again, mixing with the Herzberg states occurs, so we had to inspect the wave functions to assign the levels. Compared to the case (c) approximation only small shifts occur. In particular, the $v =$

0, $\Omega = 0$ level shifts from 0.8 cm^{-1} below the $v = 1$, $\Omega = 1$ level to 7 cm^{-1} above it.

4.3.3 New assignment

We are now in a position to make a first comparison between our computed levels and the experimentally observed levels. Although Jenouvrier *et al.* assumed a regular Hund's case (a) they had to assign the lowest observed perturbations to a $\Omega \neq 0$ $1^3\Pi_u(0)$ level because the A' $^3\Delta_{u,2}(12)$ state was involved (and $^3\Delta_2$ does not couple with $^3\Pi_0$). Hence we assume that our lowest two levels, with $v = 0$ and $\Omega = 2{,}1$ correspond to the lowest two observed states. In Sec. 4.3.6 we will show that reversing the ($v = 0$) $\Omega = 1$ and $\Omega = 2$ assignment is not at all inconsistent with the observations. The next two observed $1^3\Pi_u$ levels had a distinctly smaller rotational constant and were assigned $v = 1$, which is consistent with the ordering of the computed levels. However, we find that the lowest $v = 1$ $1^3\Pi_u$ level has $\Omega = 2$ instead of $\Omega = 0$. In the experiment, the lowest $v = 1$ level causes perturbations in both the F_{1f} and F_{2e} components of the $A^3\Sigma^+_{u,1}(11)$ states, which is consistent with our $\Omega = 2$ assignment.

For the highest observed $1^3\Pi_u$ level, which was assigned $v = 1$, $\Omega = 2$ by Jenouvrier *et al.*, only one perturbation [of the $J = 14$ F_{3f} $A^3\Sigma^+_u(11)$ level] was observed, and hence no direct determination of its rotational constant was possible. The assignment is only logical if one assumes a regular Hund's case (a) for the $v = 1$ state. As we will see below, this observed ($J = 14$) perturbation can be very well explained by our $v = 0$, $\Omega = 0$ level which lies just above the $v = 1$, $\Omega = 1$ level. Assigning this $J = 14$ perturbation to a $v = 0$ level instead of a $v = 1$ level results in a different ($J = 0$) term value because the rotational constants of $v = 0$ and $v = 1$ states are different. In Sec. 4.3.6 we will show how this new assignment leads to a new "observed" term value for the $1^3\Pi_{u,0^-}(0)$ level. In column 6 of Fig. 4.3 we show the experimental data with the adapted $1^3\Pi_{u,0^-}$ level.

4.3.4 Adjusting the $1^3\Pi_u$ curve

In the experiment information about the $1^3\Pi_u$ levels is obtained from a characteristic pattern of perturbations in a plot of the term values of the observed (Herzberg) levels as a function of $J(J+1)$ (see Fig. 4 in Ref. 19). In order to validate our assignment we construct in Section 4.3.6 a similar plot using computed RVE levels (Fig. 4.5). In order to allow a meaningful comparison between experiment and theory it is important that the perturbations between the highly vibrationally excited Herzberg states and the $1^3\Pi_u$ states occur at (approximately) the same value of J. Clearly, such a near perfect agreement between *ab initio* results and experiment is very difficult to achieve. Therefore, before we include the rotational part of the problem, we adjust the potentials slightly in order to shift the vibrational levels closer to the observed positions.

Table 4.2: Position of the $1^3\Pi_{u,\Omega}(v)$ levels with different combinations of α and r_0 in the adapted $1^3\Pi_u$ potential energy curve. Experimental data for $1^3\Pi_{u,0}(0)$ is given between parentheses because it depends on the erroneous experimental assignment as v = 1.

		D_v				
α	r_0	$1^3\Pi_{u,2}(0)$	$1^3\Pi_{u,1}(0)$	$1^3\Pi_{u,2}(1)$	$1^3\Pi_{u,1}(1)$	$1^3\Pi_{u,0^-}(0)$
Experiment		106.3	84.1	57.5	39.5	(23.5)
1.5655	0.00	119.7	94.7	59.5	42.1	37.1
1.5655	0.13	114.4	89.2	55.6	39.0	36.5
1.5655	0.26	101.5	83.0	51.3	35.6	35.8
1.3246	−0.693	101.0	82.5	51.0	35.4	35.1
Original curve		152.8	125.9	80.6	66.4	59.3

First, since our calculated $1^3\Pi_u$ levels lie somewhat too deep and the $v = 0$ / $v = 1$ separation is somewhat too large, we add a simple two-parameter repulsive term $\exp[-\alpha(r - r_0)]$ to the $1^3\Pi_u$ ABO potential. In Table 4.2 we show the energies of the $1^3\Pi_{u,\Omega}(v)$ levels for four combinations of α and r_0, together with the experimental results and the results for the unadjusted potential (which were already shown in Fig. 4.3). Since the result with $\alpha = 1.5655$ and $r_0 = 0.13$ gives agreement with all experimental data to within a few cm^{-1} we did not attempt further optimization of the parameters. The results with $(\alpha, r_0) = (1.5655, 0.26)$ and $(1.3246, -0.693)$ show that similar results can be obtained with different combinations of α and r_0. We chose to use $\alpha = 1.5655$ above $\alpha = 1.3246$ because a larger α yields a smaller relative change in the short-range part of the potential when inducing an equal change in position of the bound levels. Note furthermore that for the $1^3\Pi_{u,0}(0)$ level the difference between calculated and experimental level position is 36.5 − 23.5 = 13 cm^{-1} if we take the original data from the Jenouvrier paper. However, using our model to derive the $J = 0$ level from the observed $J = 14$ level the agreement becomes much better: 36.5 − 32.4 = 4.1 cm^{-1}.

4.3.5 Scaling the Herzberg curves

In the next step we adjusted the three Herzberg ABO potentials ($A'\,{}^3\Delta_u$, $A^3\Sigma_u^+$, $c^1\Sigma_u^-$) according to

$$V^{\text{new}}(r) = f_{\text{vert}} V[r_0 + (r - r_0) f_{\text{hor}}]. \tag{4.19}$$

Since the computed rotational constants of the lowest Herzberg vibrational levels were already in very good agreement with experiment (better than 0.7

Table 4.3: Term values with respect to the dissociation limit, D_v, for the high-lying Herzberg vibrational levels. Calculated levels are coupled state calculation, where rotation has been neglected.

	Calculated			
Level	Orig. curve	$1^3\Pi_u$ scaled	All scaled	Exper.[19]
$A'\ ^3\Delta_{u,2}(12)$	111.3	104.9	168.7	175.3
$A'\ ^3\Delta_{u,2}(11)$	321.8	321.3	404.8	397.9
$A'\ ^3\Delta_{u,1}(11)$	211.3	210.8	292.1	279.8
$A^3\Sigma^+_{u,1}(11)$	54.0	56.4	112.2	108.5
$A^3\Sigma^+_{u,0^-}(11)$	39.8	42.2	97.5	95.6
$c^1\Sigma^-_{u,0^-}(19)$	40.4	36.5	61.0	67.0
$c^1\Sigma^-_{u,0^-}(18)$	95.4	82.9	123.5	130.2
$c^1\Sigma^-_{u,0^-}(17)$	170.8	163.9	240.3	242.6

%, see Paper I) we took, for each curve, r_0 equal to the expectation value of r for the lowest vibrational level. This ensures that the scaling has a negligible effect on these rotational constants. The vertical scaling f_{vert} was chosen to get exact agreement with experiment for D_e in the Hund's case (c) approximation. Finally, f_{hor} was varied until the highest vibrational levels were in agreement with experiment to within 6 cm^{-1}. In Table 4.3 we report the D_v for several high lying Herzberg vibrational levels for the original curves as well as the adjusted curves, together with the experimental data (taken from Ref. 19). Note the influence of the scaling of the $1^3\Pi_u$ ABO curve on the Herzberg levels: the $A'\ ^3\Delta_u$ and $c^1\Sigma^-_u$ levels go up and the $A^3\Sigma^+_u$ levels go down, resulting in a reversal of $A^3\Sigma^+_{u,0^-}(11)$ and $c^1\Sigma^-_{u,0^-}(19)$. The parameters are given in Table 4.4. Because of the mixing of the Herzberg states with the $1^3\Pi_u$ states the latter are slightly altered by the change in the Herzberg potentials, as shown in the fifth column of Fig. 4.3.

Table 4.4: Parameter values used in the adaptation of the Herzberg Coulombic potential energy curves to experiment, according to Eq. (4.19).

State	f_{vert}	r_0	f_{hor}
$A'\ ^3\Delta_u$	1.01906	2.878636	0.9855
$A^3\Sigma^+_u$	1.01751	2.892466	0.9845
$c^1\Sigma^-_u$	1.02091	2.8880295	0.9800

4.3.6 Rotational energy levels

In Fig. 4.5 we plot the RVE energy levels as a function of $J(J+1)$. The levels were calculated with the two-step procedure described in Sec. 4.2.2, employing the scaled $1^3\Pi_u$ and Herzberg ABO potentials and taking into account the rotational Hamiltonian of Eq. (4.5). The threshold for selecting basis functions in the second step of the calculation was set to $E_{\text{thresh}} = 24.2$ cm^{-1} above the O($^3P_2$) + O($^3P_2$) dissociation limit. The dimension of the resulting basis ranges from 59 for $J = 0$ (only $\Omega = 0$ states) via 275 for $J = 3$ (all Ω components) to 205 for $J = 19$. In changing E_{thresh} from 19.2 cm^{-1} to 24.2 cm^{-1}, 2, 15, and 19 extra basis functions were selected for $J = 0$, 3, and 19, and all bound level positions changed less than 0.028 cm^{-1}, so we expect to be at least converged up to 0.02 cm^{-1}. To reduce the slopes of the lines $0.15J(J+1)$ has been subtracted from all term values in Fig. 4.5 (exactly as in Fig. 4 of Ref. 19). The dissociation limit is represented by the dotted line.

There is good agreement between Fig. 4.5 and the experimental results (Fig. 4 in Ref. 19). Our calculated $c^1\Sigma_u^-(18{,}19)$ levels are about 7 cm^{-1} too high and the $1^3\Pi_u(0)$ levels are about 6 cm^{-1} too deep. As a result the calculated perturbations of the Herzberg levels occur at values of the rotational quantum number J that differ at most about 2 with experiment.

The selection rule for spin-orbit coupling is $\Delta\Omega = 0$. We observe that perturbations between same-Ω states are larger than for states with different Ω quantum number. The latter are — in our Hamiltonian — only coupled via $\hat{H}_{\text{rot}}^{(JS)}$ [Eq. (4.7)]. Note that the most visible effect is to shift down the F_{1f} component of the $A^3\Sigma_{u,1}^+$ (11) level via first order coupling with the $A^3\Sigma_{u,0^-}^+$ (11) F_{3f} levels. A similar shift does not occur for the $A^3\Sigma_{u,1}^+$ F_{2e} level since there is no $A^3\Sigma_{u,0}^+$ state of e parity (compare the two dash-dot lines in Fig. 4.5).

A $\Delta\Omega = 0$ perturbation occurs at $J = 14$, 15 (16, 17 in the experiment) between the $1^3\Pi_{u,2}(0)$ and $A'\ {}^3\Delta_{u,2}(12)$ states. In the original assignment of Jenouvrier *et al.* this was a $\Delta\Omega = 1$ perturbation [$1^3\Pi_{u,1}(0)$ — $A'\ {}^3\Delta_{u,2}(12)$]. In Fig. 4.5, however, we find that the perturbation between $A'\ {}^3\Delta_{u,2}(12)$ and $1^3\Pi_{u,1}(0)$ (around $J = 17$) is negligible. Similarly, the perturbation between $A^3\Sigma_{u,1}^+(11)$ and $1^3\Pi_{u,1}(0)$ around $J = 9$, 10 (11, 12 in the experiment) was a $\Delta\Omega = 1$ perturbation in the original assignment.

The solid lines in Fig. 4.5 represent fits for the J-dependent term values of the 5 perturbing $1^3\Pi_u$ levels:

$$T_{v,\Omega}(J) = -D_{v,\Omega} + B_{v,\Omega}J(J+1) - \tilde{D}_{v,\Omega}[J(J+1)]^2. \tag{4.20}$$

The dashed lines represent similar fits for the Herzberg levels. The parameters are given in Table 4.5, together with the experimental results. Centrifugal distortion parameters $\tilde{D}_{v,\Omega}$ were not reported in Ref. 19, probably since the observed range of J values for each state was too limited to extract a reliable

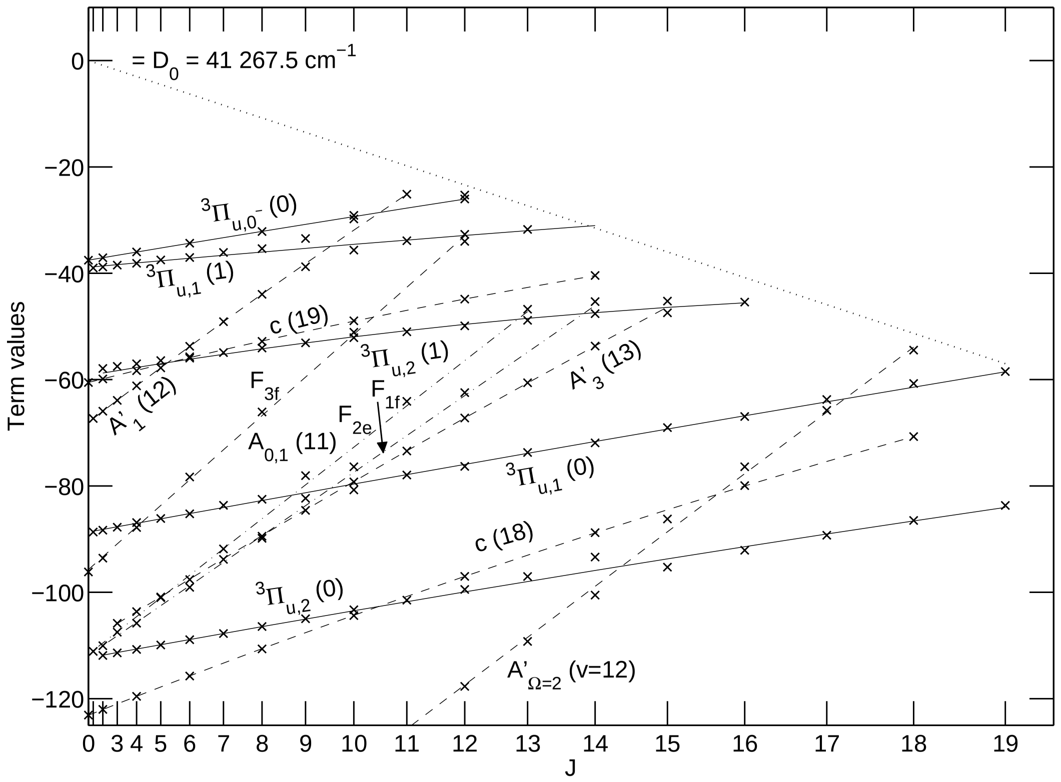

Figure 4.5: Calculated RVE energy levels (× marks) lying less than 120 cm^{-1} below the dissociation limit (dotted line). For clarity, $0.15J(J+1)$ cm^{-1} was subtracted from the term values. Solid lines are fitted values $T_{v,\Omega}(J) = -D_{v,\Omega} + B_{v,\Omega}J(J+1) - \tilde{D}_{v,\Omega}[J(J+1)]^2$ for the $1^3\Pi_u$ levels, and dashed lines are the same fits for the Herzberg levels.

Table 4.5: Spectroscopic parameters for $1^3\Pi_u$ bound states. Experimental data for the $1^3\Pi_{u,0^-}$ (0) level is given between parentheses because this data depends on the erroneous experimental assignment of this level as $v = 1$.

Level	$D_{v,\Omega}$			$B_{v,\Omega}$		$B^{\mathrm{eff}}_{v,\Omega}(J)$	J	$\tilde{D}_{v,\Omega}$
	Calc.	Exp.	Lit.[a]	Calc.	Exp.			$10^{-5}\mathrm{cm}^{-1}$
$1^3\Pi_{u,2}(0)$	112.6	106.3	96.9	0.2329	0.221	0.2268	16	2.23
$1^3\Pi_{u,1}(0)$	89.0	84.1	76.9	0.2333	0.226	0.2319	11	1.05
$1^3\Pi_{u,2}(1)$	59.5	57.5	54.7	0.2267	0.165	0.2090	13	9.71
$1^3\Pi_{u,1}(1)$	39.2	39.5	38.0	0.1911	0.170	0.1863	16	1.78
$1^3\Pi_{u,0}(0)$	37.8	(23.5)	30.2	0.2265	(0.175)	0.2215	14	1.84

---

[a] For $1^3\Pi_u$ potential from Ref. 18.

value. Note that the $D_{0,\Omega=1,2}$ dissociation energies agree to within 6 cm^{-1} with experiment and that for $v = 1$ the agreement is even better. For the $1^3\Pi_{u,0^-}(0)$ level there seems to be a discrepancy of 14.3 cm^{-1}. In our calculation the crossing of the $1^3\Pi_{u,0^-}(0)$ with $A^3\Sigma^+_{u,0^-}(11)$ F_{3f} level occurs at $J \approx 13$. Jenouvrier *et al.* observed a perturbation of the $J = 14, F_{3f}$ component of the $A^3\Sigma^+_{u,0^-}(11)$ level. They assigned this perturbation to the $1^3\Pi_{u,2}(1)$ level. However, no further perturbations arising from this "$1^3\Pi_{u,2}(1)$" state were observed and hence the reported rotational constant of 0.175 cm^{-1} was derived from observations of other $v = 1$ $1^3\Pi_u$ states via the Hund's case (a) model [Eq. (31) in Ref. 19]. Furthermore the reported dissociation energy of 23.5 cm^{-1} was derived by extrapolating the observed $J = 14$ term value using the rotational constant of 0.175 cm^{-1}. However, with our assignment of the perturbation to the $1^3\Pi_{u,0^-}(0)$ level, extrapolating to $J = 0$ using our rotational constant $B_{0,0} = 0.2265$ cm^{-1} and distortion constant $\tilde{D}_{0,0} = 1.84 \cdot 10^{-5}$ cm^{-1} we arrive at an experimental $D_{0,0}$ of 32.4 cm^{-1}, which is in good agreement with our calculated value of 37.8 cm^{-1}.

Our calculated rotational constants are somewhat too large. However, in the experiment the centrifugal distortion constants were neglected. Therefore, we also computed effective rotational constants (Table 4.5)

$$B^{\mathrm{eff}}_{v,\Omega}(J) = B_{v,\Omega} - \tilde{D}_{v,\Omega} J(J+1) \tag{4.21}$$

for J values in the region of the dominant perturbations. The agreement with these effective rotational constants is within about 2 to 3 standard deviations, again with the exception of the $1^3\Pi_{u,0}$ (0) level.

In Table 4.5 we also report (in the column marked "Lit.") results of a calculation employing a literature[18] potential energy curve for the $1^3\Pi_u$state (and all other potentials and couplings from our own scaled results). Since this is a calculation where the rotational Hamiltonian was neglected, we have no rotational and distortion constants in this case. We see that the vibrational

Table 4.6: Spectroscopic parameters for the three ab initio ABO potential energy curves under comparison.

Curve	$R_e(a_0)$	$\omega_e(\mathrm{cm}^{-1})$	$D_e(\mathrm{cm}^{-1})$
Literature (Ref. 18)	5.6426	65.4072	191.9923
From Paper I	5.3328	92.5180	279.5888
Present, adjusted	5.4991	85.2712	223.6329

levels lie too high, from 9.6 cm^{-1} for $1^3\Pi_{u,2}(0)$ to 1.5 cm^{-1} for $1^3\Pi_{u,1}(1)$, an accuracy comparable with our adjusted $1^3\Pi_u$ potential energy curve. In Table 4.6 we give spectroscopic parameters for the three $1^3\Pi_u$ ABO potential energy curves. We see that the parameters for the literature curve and the present adjusted curve differ by a fairly large amount, though the final level positions are of a reasonably good quality for both curves. This indicates the importance of the spin-orbit coupling in this recoupling region. In paper I we showed that the original unscaled ABO states yield better spectroscopic results for the Herzberg states than the literature curves from Ref. 18. We would therefore expect the original curve to be better for the $1^3\Pi_u$ state also, but it is not. The original curve was calculated employing an equally good (in the long range, $r \geq 7.5$ a$_0$) or better (in the short range, $r \leq 6.5$ a$_0$) one-electron basis than the literature curve, and both curves were calculated on the multireference configuration interaction (MRCI) plus size consistency correction level of theory. Therefore we tentatively suggest that the internal contraction scheme of the MOLPRO MRCI program, employed in the calculation in paper I, is not as good as uncontracted MRCI for this weakly bound Van der Waals-like state, though in general the internal contraction scheme gives good results for chemically bound systems.

4.4 Summary and conclusions

In addition to the three Herzberg states, there are five ungerade states in O_2 that correlate with the O(^3P) + O(^3P) dissociation limit. We calculated all rotational-vibrational-electronic bound states up to $J = 19$ supported by these potentials, taking into account spin-orbit and rotational couplings. We neglect the homogeneous spin-electronic ($\hat{L}^{\pm}\hat{S}^{\mp}/2\mu r^2$) and the L-uncoupling operator ($\hat{L}^{\pm}\hat{J}^{\mp}/2\mu r^2$), but we kept the S-uncoupling ($\hat{S}^{\pm}\hat{J}^{\mp}/2\mu r^2$). *Ab initio* potentials and SO couplings were available from our previous study.

In a recent spectroscopic study of the Herzberg bands perturbations were found in the $A^3\Sigma_u^+(v = 11)$, $c^1\Sigma_u^-(18, 19)$, and $A'\ ^3\Delta_u(12)$ levels. Assuming a regular Hund's case (a) multiplet for the $1^3\Pi_u$ state, these perturbations were assigned to the $1^3\Pi_{u,1}(0)$, $1^3\Pi_{u,2}(0)$, $1^3\Pi_{u,0}(1)$, $1^3\Pi_{u,1}(1)$ and $1^3\Pi_{u,2}(1)$ levels. Our calculations yield a new assignment of the perturbing levels, namely $1^3\Pi_{u,2}(0)$, $1^3\Pi_{u,1}(0)$, $1^3\Pi_{u,2}(1)$, $1^3\Pi_{u,1}(1)$, and $1^3\Pi_{u,0^-}(0)$. This new assignment is consistent with the experimental data, and better than the original assignment, because all the large perturbations are now explained by large $\Delta\Omega = 0$ spin-orbit couplings, and the smaller perturbations by smaller $\Delta\Omega = \pm 1$ spin-rotation couplings. The calculated diagonal $1^3\Pi_u$ SO coupling is negative for $r \geq 4$ a$_0$ so one expects to find an inverted multiplet for the $1^3\Pi_u$ state, which has an $r_e \approx 5.3$ a$_0$. In this region the SO couplings are comparable in size to the Coulomb splittings between the eight ungerade states and a pure Hund's case description is not possible. An approximate Hund's case (c) description is in reasonable agreement with the more exact calculations.

We also slightly scaled the Herzberg potentials and adjusted the $1^3\Pi_u$ potential by adding a small repulsive term. In this way we achieved agreement with the experimentally observed perturbing levels to within 7 cm^{-1}. Replacing the *ab initio* potential from Ref. 12 by the potential from Ref. 18 gave a similar good agreement (in combination with the scaled Herzberg potentials).

Our calculated rotational constants of the $1^3\Pi_u$ levels are slightly too large, but still agree with experiment within 2-3 standard deviations (see Table 4.5), except for the level we assigned as $1^3\Pi_{u,0^-}(0)$. This level was originally assigned as $1^3\Pi_{u,2}(1)$ and we show that the reported rotational constant is an artifact of this incorrect assignment. We also compute rotational distortion constants and show that they are not negligible for the higher rotational levels that were observed experimentally.

Appendix: Basis functions and rotational Hamiltonian

The recipes for computing rotational Hamiltonian matrix elements for Hund's case (a) and (c) basis functions can be found in several text books.[21, 23, 24] The rules can be derived taking into account the normal and anomalous commutation relations of the appropriate rigid rotor angular momentum operators. This method was introduced by Van Vleck[25] for non-linear molecules. For linear molecules the derivation is more difficult since two-angle embedded rotation operators have complicated commutation relations.[20, 26] The problem arises because a linear molecule only uniquely defines a BF z-axis. It was shown by Hougen[20] that the familiar results can be obtained by the introduction of an extraneous rotation angle. This leads to an isomorphic Hamiltonian, for which only some of the eigenvalues and eigenfunctions correspond to the physical solutions. An analogous problem occurs in the study of Van der Waals complexes when a two-angle embedded BF frame is chosen. In an effort to avoid the isomorphic Hamiltonian in that case alternative derivations were presented, one starting with Cartesian coordinates and applying the chain rule[27] and one employing the Podolsky form of the Laplacian.[28] Both derivations require a somewhat *ad hoc* rewriting of the Hamiltonian in terms of angular momentum operators to arrive at the familiar results and electron spin was not considered.

Here we present a new derivation which only requires elementary angular momentum theory and which does not involve the isomorphic Hamiltonian. Although we take the present O_2 system as an illustration, our derivation is also completely rigorous for half-integer spin and the application to Van der Waals complexes should be transparent. Furthermore we present a compact and rigorous derivation of the inversion symmetry behavior of the basis functions. Because several phase conventions have been used in the literature[29] great care is required when applying text book formulas in combination with *ab initio* data.

The present approach was inspired by the discussion of angular momentum theory in Chap. 3 of the book by Biedenharn and Louck.[30]

4.5.1 Basis Functions

The coordinates of the unit vectors that define the BF axes with respect to the space fixed (SF) frame are given by [Eq. (2.37) in Ref. 30]

$$\begin{aligned}[\underline{e}_x^{BF}\,\underline{e}_y^{BF}\,\underline{e}_z^{BF}] &\equiv \boldsymbol{R}(\alpha,\beta,0) = \boldsymbol{R}_Z(\alpha)\boldsymbol{R}_Y(\beta)\\ &= \begin{bmatrix} \cos\alpha\cos\beta & -\sin\alpha & \cos\alpha\sin\beta \\ \sin\alpha\cos\beta & \cos\alpha & \sin\alpha\sin\beta \\ -\sin\beta & 0 & \cos\beta \end{bmatrix}, \end{aligned} \tag{4.22}$$

where α and β are the spherical polar coordinates of the diatomic internuclear axis with respect to the SF frame. We define two-angle embedded Hund's case (a) basis functions as

$$|(L)\Lambda S\Sigma JM\Omega; r\rangle \equiv \sqrt{\frac{2J+1}{4\pi}} D^{(J)*}_{M\Omega}(\alpha,\beta,0)\hat{R}(\alpha,\beta,0)|(L)\Lambda S\Sigma; r\rangle_{\mathrm{SF}}, \tag{4.23}$$

where we introduced the rotation operator in the active convention

$$\hat{R}(\alpha,\beta,0) \equiv \hat{R}_Z(\alpha)\hat{R}_Y(\beta) = \exp(-i\alpha\hat{J}^{SF}_{\mathrm{elec},Z})\exp(-i\beta\hat{J}^{SF}_{\mathrm{elec},Y}). \tag{4.24}$$

The total electronic angular momentum operator is defined as $\underline{\hat{J}}^{SF}_{\mathrm{elec}} = \underline{\hat{L}}^{SF} + \underline{\hat{S}}^{SF}$. The electronic wave functions calculated in paper I for the O atoms on the SF Z-axis are denoted here as $|(L)\Lambda S\Sigma; r\rangle_{\mathrm{SF}}$. Applying the rotation operator to these functions yields the BF electronic wave functions. The nuclear rotational part of the wave function is given by the Wigner D-matrix, which is also defined in the active convention.[30, 31] From here on we will write $D^{(J)*}_{M\Omega}\hat{R}$ instead of $D^{(J)*}_{M\Omega}(\alpha,\beta,0)\hat{R}(\alpha,\beta,0)$ and suppress the parametric r dependence of the electronic wave functions for compactness.

4.5.2 Action of SF angular momentum operators on basis functions

The space fixed electronic angular momentum operators transform under nuclear rotation as [see Eq. (3.42) of Ref. 30]

$$\hat{R}(\alpha,\beta,0)\underline{\hat{J}}^{SF}_{\text{elec}}\hat{R}^{\dagger}(\alpha,\beta,0) = \boldsymbol{R}^T(\alpha,\beta,0)\underline{\hat{J}}^{SF}_{\text{elec}} = \underline{\hat{J}}^{BF}_{\text{elec}}. \tag{4.25}$$

We have $[\hat{L}^{SF}_i, \hat{S}^{SF}_j] = 0$, $[\hat{J}^{SF}_{\text{elec},i}, D^{(J)*}(\alpha,\beta,0)] = 0$, and $[\hat{A}^{SF}_i, \hat{A}^{SF}_j] = i\epsilon_{ijk}$ $\hat{A}^{SF}_k$ for all SF angular momentum operators, where ϵ_{ijk} is the Levi-Civita tensor and summation over repeated indices is assumed. From these commutation relations and Eqs. (4.25) and (4.22) we obtain

$$\hat{J}^{SF}_{\text{elec},Z}D^{(J)*}_{M\Omega}\hat{R} = D^{(J)*}_{M\Omega}\hat{R}\left[-\sin\beta\hat{J}^{SF}_{\text{elec},X} + \cos\beta\hat{J}^{SF}_{\text{elec},Z}\right], \tag{4.26}$$

$$\hat{J}^{SF}_{\text{elec},\pm}D^{(J)*}_{M\Omega}\hat{R} = D^{(J)*}_{M\Omega}\hat{R}e^{\pm i\alpha}\left[\cos\beta\hat{J}^{SF}_{\text{elec},X} \pm i\hat{J}^{SF}_{\text{elec},Y} + \sin\beta\hat{J}^{SF}_{\text{elec},Z}\right], \tag{4.27}$$

and similarly for $\underline{\hat{L}}^{SF}$ and $\underline{\hat{S}}^{SF}$. Throughout this paper we define raising/lowering operators as $\hat{A}_{\pm} \equiv \hat{A}_X \pm i\hat{A}_Y$.

The angular momentum operator $\underline{\hat{l}}^{SF}$ associated with the rotation of the nuclei is the usual one-particle angular momentum operator acting on the polar angles α and β, as defined in Eq. (3.106) of Ref. 30. Its action on $D^{(J)*}_{M\Omega}(\alpha,\beta,0)$ can be derived using the action of standard rigid rotor rotational operators $\hat{\mathcal{L}}(\alpha,\beta,\gamma)$ [Eq. (3.101) of Ref. 30] on a three-angle D-matrix $D^{(J)*}_{M\Omega}(\alpha,\beta,\gamma)$ and the relations

$$D^{(J)*}_{M\Omega}(\alpha,\beta,0) = D^{(J)*}_{M\Omega}(\alpha,\beta,\gamma)e^{-i\Omega\gamma} \tag{4.28}$$

$$\hat{l}^{SF}_X = \hat{\mathcal{L}}^{SF}_X + i\frac{\cos\alpha}{\sin\beta}\frac{\partial}{\partial\gamma} \tag{4.29}$$

$$\hat{l}^{SF}_Y = \hat{\mathcal{L}}^{SF}_Y + i\frac{\sin\alpha}{\sin\beta}\frac{\partial}{\partial\gamma} \tag{4.30}$$

$$\hat{l}^{SF}_Z = \hat{\mathcal{L}}^{SF}_Z. \tag{4.31}$$

The result is

$$[\hat{l}^{SF}_Z, D^{(J)*}_{M\Omega}(\alpha,\beta,0)] = MD^{(J)*}_{M\Omega}(\alpha,\beta,0) \tag{4.32}$$

$$[\hat{l}^{SF}_{\pm}, D^{(J)*}_{M\Omega}(\alpha,\beta,0)] = c_{\pm}(J,M)D^{(J)*}_{M\pm1,\Omega}(\alpha,\beta,0) - \Omega\frac{e^{\pm i\alpha}}{\sin\beta}D^{(J)*}_{M\Omega}(\alpha,\beta,0), \tag{4.33}$$

where $c_{\pm}(J,M) = [J(J+1) - M(M\pm1)]^{1/2}$. The action of $\underline{\hat{l}}^{SF}$ on the rotation operator $\hat{R}(\alpha,\beta,0)$ follows from differentiation of $\hat{R}(\alpha,\beta,0)$ with respect to α

and β

$$[\hat{l}^{SF}_Z, \hat{R}(\alpha,\beta,0)] = \hat{R}(\alpha,\beta,0)\left[\sin\beta\,\hat{J}^{SF}_{\mathrm{elec},X} - \cos\beta\,\hat{J}^{SF}_{\mathrm{elec},Z}\right], \tag{4.34}$$

$$[\hat{l}^{SF}_\pm, \hat{R}(\alpha,\beta,0)] = \hat{R}(\alpha,\beta,0)e^{\pm i\alpha}\left[-\cos\beta\,\hat{J}^{SF}_{\mathrm{elec},X} \mp i\hat{J}^{SF}_{\mathrm{elec},Y} + \frac{\cos^2\beta}{\sin\beta}\hat{J}^{SF}_{\mathrm{elec},Z}\right]. \tag{4.35}$$

This yields

$$[\hat{l}^{SF}_Z, D^{(J)*}_{M\Omega}\hat{R}] = MD^{(J)*}_{M\Omega}\hat{R} + D^{(J)*}_{M\Omega}\hat{R}\left[\sin\beta\,\hat{J}^{SF}_{\mathrm{elec},X} - \cos\beta\,\hat{J}^{SF}_{\mathrm{elec},Z}\right] \tag{4.36}$$

$$\begin{aligned}[\hat{l}^{SF}_\pm, D^{(J)*}_{M\Omega}\hat{R}] &= c_\pm(J,M)D^{(J)*}_{M\pm1,\Omega}\hat{R} \\ &+ D^{(J)*}_{M\Omega}\hat{R}e^{\pm i\alpha}\left[-\frac{\Omega}{\sin\beta} - \cos\beta\,\hat{J}^{SF}_{\mathrm{elec},X} \mp i\hat{J}^{SF}_{\mathrm{elec},Y} + \frac{\cos^2\beta}{\sin\beta}\hat{J}^{SF}_{\mathrm{elec},Z}\right].\end{aligned} \tag{4.37}$$

Combining $\underline{\hat{J}}^{SF} = \underline{\hat{l}}^{SF} + \underline{\hat{J}}^{SF}_{\mathrm{elec}}$ yields

$$\hat{J}^{SF}_Z D^{(J)*}_{M\Omega}\hat{R}|(L)\Lambda S\Sigma\rangle_{\mathrm{SF}} = MD^{(J)*}_{M\Omega}\hat{R}|(L)\Lambda S\Sigma\rangle_{\mathrm{SF}} \tag{4.38}$$

$$\begin{aligned}&\hat{J}^{SF}_\pm D^{(J)*}_{M\Omega}\hat{R}|(L)\Lambda S\Sigma\rangle_{\mathrm{SF}} = \\ &\qquad\left\{c_\pm(J,M)D^{(J)*}_{M\pm1,\Omega}\hat{R} + D^{(J)*}_{M\Omega}\hat{R}\frac{e^{\pm i\alpha}}{\sin\beta}\left[\hat{J}^{SF}_{\mathrm{elec},Z} - \Omega\right]\right\}|(L)\Lambda S\Sigma\rangle_{\mathrm{SF}}.\end{aligned} \tag{4.39}$$

Thus the familiar standard results are only obtained when all $|(L)\Lambda S\Sigma\rangle_{\mathrm{SF}}$ are eigenfunctions of $\hat{J}^{SF}_{\mathrm{elec},Z}$ with eigenvalue $\Lambda + \Sigma$ equal to Ω, so that the second term in Eq. (4.39) vanishes. We chose our basis functions to have this property, and hence we have

$$\hat{J}^{SF}_Z|(L)\Lambda S\Sigma JM\Omega\rangle = M|(L)\Lambda S\Sigma JM\Omega\rangle \tag{4.40}$$

$$(\hat{J}^{SF})^2|(L)\Lambda S\Sigma JM\Omega\rangle = J(J+1)|(L)\Lambda S\Sigma JM\Omega\rangle. \tag{4.41}$$

4.5.3 Action of BF angular momentum operators on basis functions

To derive the matrix elements for the nuclear rotational kinetic energy, we will have to look at the action of BF operators on the basis functions. We define BF operators $\underline{\hat{J}}^{BF}$, $\underline{\hat{l}}^{BF}$, $\underline{\hat{L}}^{BF}$, and $\underline{\hat{S}}^{BF}$ by

$$\underline{\hat{A}}^{BF} \equiv \boldsymbol{R}^T(\alpha,\beta,0)\underline{\hat{A}}^{SF}. \tag{4.42}$$

From the transformation property (4.25) we have

$$\underline{\hat{L}}^{BF}\hat{R}(\alpha,\beta,0)=\hat{R}(\alpha,\beta,0)\underline{\hat{L}}^{SF} \quad \text{and} \quad \underline{\hat{S}}^{BF}\hat{R}(\alpha,\beta,0)=\hat{R}(\alpha,\beta,0)\underline{\hat{S}}^{SF}, \tag{4.43}$$

and, using $[\hat{L}_i^{BF}, D_{M\Omega}^{(J)*}]=[\hat{S}_i^{BF}, D_{M\Omega}^{(J)*}]=0$ we find

$$\hat{L}_Z^{BF}|(L)\Lambda S\Sigma JM\Omega\rangle = \Lambda|(L)\Lambda S\Sigma JM\Omega\rangle, \tag{4.44}$$

$$\hat{S}_Z^{BF}|(L)\Lambda S\Sigma JM\Omega\rangle = \Sigma|(L)\Lambda S\Sigma JM\Omega\rangle, \tag{4.45}$$

$$\hat{S}_\pm^{BF}|(L)\Lambda S\Sigma JM\Omega\rangle = c_\pm(S,\Sigma)|(L)\Lambda S\Sigma\pm 1 JM\Omega\rangle. \tag{4.46}$$

Even though the electronic states are not eigenfunctions of $(\hat{L}^{BF})^2$ we still have $\hat{L}_\pm^{BF}|(L)\Lambda S\Sigma JM\Omega\rangle = D_{M\Omega}^{(J)*}\hat{R}\hat{L}_\pm^{SF}|(L)\Lambda S\Sigma\rangle_{\mathrm{SF}}$. Substituting the expressions for $\underline{\hat{l}}^{SF}$ into Eq. (4.42) gives $\hat{l}_Z^{BF}=0$ and

$$\hat{l}_\pm^{BF} = \frac{i}{\sin\beta}\frac{\partial}{\partial\alpha} \pm \frac{\partial}{\partial\beta}. \tag{4.47}$$

Using the relations between $\hat{l}_\pm^{BF}$ and the rigid rotor BF operators [Eq. (3.122) in Ref. 30], and Eq. (4.28) we find

$$\hat{l}_\pm^{BF} D_{M\Omega}^{(J)*}(\alpha,\beta,0) = c_\mp(J,\Omega) D_{M,\Omega\mp 1}^{(J)*}(\alpha,\beta,0) - \Omega\cot\beta D_{M\Omega}^{(J)*}(\alpha,\beta,0), \tag{4.48}$$

$$\hat{l}_\pm^{BF}\hat{R}(\alpha,\beta,0) = \hat{R}(\alpha,\beta,0)\left[-\hat{J}_{\mathrm{elec},\pm}^{SF} + \cot\beta\hat{J}_{\mathrm{elec},Z}^{SF}\right], \tag{4.49}$$

yielding

$$\hat{l}_\pm^{BF} D_{M\Omega}^{(J)*}\hat{R} = c_\mp(J,\Omega) D_{M,\Omega\mp 1}^{(J)*}\hat{R} + D_{M\Omega}^{(J)*}\hat{R}\left\{-\hat{J}_{\mathrm{elec},\pm}^{SF} + \cot\beta\left[\hat{J}_{\mathrm{elec},Z}^{SF} - \Omega\right]\right\}. \tag{4.50}$$

We finally obtain

$$\hat{J}_Z^{BF}|(L)\Lambda S\Sigma JM\Omega\rangle = \Omega|(L)\Lambda S\Sigma JM\Omega\rangle \tag{4.51}$$

$$\hat{J}_\pm^{BF}|(L)\Lambda S\Sigma JM\Omega\rangle = c_\mp(J,\Omega)|(L)\Lambda S\Sigma JM\Omega\mp 1\rangle. \tag{4.52}$$

4.5.4 Rotational Hamiltonian

The Hamiltonian for the nuclear rotational kinetic energy is

$$\hat{H}_{\mathrm{rot}} = \frac{1}{2\mu r^2}\left(\hat{l}^{SF}\right)^2 = \frac{1}{2\mu r^2}\left[\left(\hat{J}^{SF}\right)^2 + \left(\hat{L}^{SF}\right)^2 + \left(\hat{S}^{SF}\right)^2 \right.$$
$$\left. -2\underline{\hat{L}}^{SF}\cdot\underline{\hat{J}}^{SF} - 2\underline{\hat{S}}^{SF}\cdot\underline{\hat{J}}^{SF} + 2\underline{\hat{L}}^{SF}\cdot\underline{\hat{S}}^{SF}\right]. \tag{4.53}$$

Using the orthogonality of $\boldsymbol{R}(\alpha,\beta,0)$ we can derive that $[\hat{L}_i^{BF}, \hat{L}_j^{BF}] = i\epsilon_{ijk}$ $\hat{L}_k^{BF}$ and $[\hat{S}_i^{BF}, \hat{S}_j^{BF}] = i\epsilon_{ijk}\hat{S}_k^{BF}$. Furthermore

$$[R_{ij}(\alpha,\beta,0), \hat{L}_k^{BF}] = [R_{ij}(\alpha,\beta,0), \hat{S}_k^{BF}] = 0,$$

and thus

$$\underline{\hat{A}}^{SF}\cdot\underline{\hat{B}}^{SF}=\underline{\hat{A}}^{BF}\cdot\underline{\hat{B}}^{BF}=\frac{1}{2}\left(\hat{A}_{+}^{BF}\hat{B}_{-}^{BF}+\hat{A}_{-}^{BF}\hat{B}_{+}^{BF}\right)+\hat{A}_{z}^{BF}\hat{B}_{z}^{BF}\qquad(4.54)$$

for the inner products $\left(\hat{S}^{SF}\right)^2$, $\underline{\hat{L}}^{SF}\cdot\underline{\hat{J}}^{SF}$, $\underline{\hat{S}}^{SF}\cdot\underline{\hat{J}}^{SF}$, and $\underline{\hat{L}}^{SF}\cdot\underline{\hat{S}}^{SF}$. Since $\hat{l}_Z^{BF}=0$ we have $\hat{J}_Z^{BF}=\hat{L}_Z^{BF}+\hat{S}_Z^{BF}$, and we can rewrite the rotational Hamiltonian as Eq. (4.4), where we dropped the BF label on the BF operators, and used small z, and superscript ± for BF components, in accordance to the notation of Lefebvre-Brion.[21]

4.5.5 Parity label

The space fixed inversion operator $\hat{\imath}$ acts on both nuclear and electronic coordinates. It commutes with all SF angular momentum operators, it has the properties $\hat{\imath}^\dagger\hat{\imath}=1$ and $\hat{\imath}=\hat{\imath}^\dagger$, and its action on the polar angles α and β is given by $\hat{\imath}\alpha\hat{\imath}^\dagger=\alpha+\pi$ and $\hat{\imath}\beta\hat{\imath}^\dagger=\pi-\beta$. Its action on the Wigner D-matrix is given by

$$\hat{\imath}D_{M\Omega}^{(J)*}(\alpha,\beta,0)\hat{\imath}^\dagger=\exp[iM(\alpha+\pi)]d_{M\Omega}^{J}(\pi-\beta)=\exp(-i\pi J)D_{M,-\Omega}^{(J)*}(\alpha,\beta,0),\qquad(4.55)$$

where we used Eqs. (3.67) and (3.75) of Ref. 31 in the second step. To derive the action of $\hat{\imath}$ on the rotation operator we first observe that from Eq. (4.25) we have

$$\hat{R}_Z(\pi)\hat{J}_Y\hat{R}_Z^\dagger(\pi)=-\hat{J}_Y\qquad(4.56)$$

and hence

$$\hat{R}_Z(\pi)\hat{R}_Y(-\beta)\hat{R}_Z^\dagger(\pi)=\hat{R}_Y(\beta).\qquad(4.57)$$

Using this relation one can show that

$$\hat{\imath}\hat{R}(\alpha,\beta,0)\hat{\imath}^\dagger=\hat{R}_Z(\alpha)\hat{R}_Z(\pi)\hat{R}_Y(-\beta)\hat{R}_Y(\pi)=\hat{R}(\alpha,\beta,0)\hat{R}_Y(\pi)\hat{R}_Z(-\pi).\qquad(4.58)$$

With the use of

$$\hat{R}_Z(-\pi)|(L)\Lambda S\Sigma\rangle_{\mathrm{SF}}=\exp[i\pi(\Lambda+\Sigma)]|(L)\Lambda S\Sigma\rangle_{\mathrm{SF}}$$

and $[\hat{R}_Z(-\pi),\hat{\imath}]=0$ we derive

$$\hat{\imath}|(L)\Lambda S\Sigma JM\Omega\rangle=\\\exp[-i\pi(J-\Omega)]D_{M,-\Omega}^{(J)*}(\alpha,\beta,0)\hat{R}(\alpha,\beta,0)\hat{R}_Y(\pi)\hat{\imath}|(L)\Lambda S\Sigma\rangle_{\mathrm{SF}}.\qquad(4.59)$$

Thus, to work out this expression we only have to apply $\hat{R}_Y(\pi)\hat{\imath}$ to $|(L)\Lambda S\Sigma\rangle_{\mathrm{SF}}$, which is the electronic wave function in the space-fixed frame as obtained from the *ab initio* calculation. Since $[\hat{\imath},\hat{L}_Z]=[\hat{\imath},\hat{S}_Z]=0$, we find that $\hat{\imath}$ does not change the value of Ω in the ket $|(L)\Lambda S\Sigma\rangle_{\mathrm{SF}}$. SF inversion does not act on spin coordinates, i.e., $\hat{\imath}|S\Sigma\rangle_{\mathrm{SF}} = |S\Sigma\rangle_{\mathrm{SF}}$, and kets can be rotated with a Wigner D-matrix, so $\hat{R}_Y(\pi)\hat{\imath}|S\Sigma\rangle_{\mathrm{SF}} = \sum_{\Sigma'} |S\Sigma'\rangle_{\mathrm{SF}} D^{(S)}_{\Sigma'\Sigma}(0,\pi,0) = (-1)^{S-\Sigma}|S{-}\Sigma\rangle_{\mathrm{SF}}$. For the spatial part we have $\hat{R}_Y(\pi)\hat{\imath}|(L)\Lambda\rangle_{\mathrm{SF}} = \hat{\sigma}_v(XZ)|(L)\Lambda\rangle_{\mathrm{SF}}$, where $\hat{\sigma}_v$ (XZ) denotes reflection in the SF XZ plane. For one-electron orbitals described by a spherical harmonic we have $\hat{\sigma}_v(XZ)|l\lambda\rangle = (-1)^{\lambda}|l-\lambda\rangle$, and for a many-electron ket $|(l_i)L\Lambda\rangle$ consisting of Clebsch-Gordan coupled one-electron kets we find $\hat{\sigma}_v(XZ)|(l_i)L\Lambda\rangle = (-1)^{\sum_i l_i + L + \Lambda}|(l_i)L-\Lambda\rangle$. For a diatomic molecule L is not a good quantum number, but a state that is asymptotically $\Sigma^{\pm}$, will be $\Sigma^{\pm}$ for finite R also. All our states are asymptotically O(^3P) + O(^3P), with four p and four s electrons per atom. Thus $\hat{\sigma}_v(XZ)|(L)\Lambda\rangle_{\mathrm{SF}} = (-1)^{L+\Lambda}|(L){-}\Lambda\rangle_{\mathrm{SF}}$, yielding

$$\hat{R}_Y(\pi)\hat{\imath}|(L)\Lambda S\Sigma\rangle_{\mathrm{SF}} = (-1)^{S-\Sigma+L+\Lambda}|(L){-}\Lambda S{-}\Sigma\rangle_{\mathrm{SF}},$$

and finally

$$\hat{\imath}|(L)\Lambda S\Sigma JM\Omega\rangle = (-1)^{J+L-S}|(L){-}\Lambda S{-}\Sigma JM{-}\Omega\rangle. \tag{4.60}$$

For our ungerade states $(-1)^{L-S}$ is odd.[14]

The ^{16}O isotope has nuclear spin $I = 0$. Hence, from the Pauli principle for bosons, it follows that the spatial part of the nuclear wave function must be symmetric under space fixed inversion. Thus, for the ungerade electronic states of ^{16}O ^{16}O only odd parity wave functions are allowed.

Acknowledgments

We thank Ad van der Avoird and Paul E. S. Wormer for useful discussions and for carefully reading the manuscript. This research has been financially supported by the Council for Chemical Sciences of the Netherlands Organization for Scientific Research (CW-NWO).

Bibliography

[1] G. Herzberg, Naturwissenschaften **20**, 577 (1932).

[2] G. Herzberg, Can. J. Phys. **30**, 185 (1952).

[3] G. Herzberg, Can. J. Phys. **31**, 657 (1953).

[4] D. A. Ramsay, Can. J. Phys. **64**, 717 (1986).

[5] P. M. Borrell, P. Borrell, and D. A. Ramsay, Can. J. Phys. **64**, 721 (1986).

[6] B. Coquart and D. A. Ramsay, Can. J. Phys. **64**, 726 (1986).

[7] T. G. Slanger and P. C. Cosby, J. Phys. Chem. **92**, 267 (1988).

[8] T. G. Slanger, D. L. Huestis, P. C. Cosby, H. Naus, and G. Meijer, J. Chem. Phys. **105**, 9393 (1996).

[9] K. Yoshino, J. R. Esmond, J. E. Murray, W. H. Parkinson, A. P. Thorne, R. C. M. Learner, and G. Cox, J. Chem. Phys. **103**, 1243 (1995).

[10] K. Yoshino, J. R. Esmond, W. H. Parkinson, A. P. Thorne, R. C. M. Learner, and G. Cox, J. Chem. Phys. **111**, 2960 (1999).

[11] K. Yoshino, J. R. Esmond, W. H. Parkinson, A. P. Thorne, R. C. M. Learner, G. Cox, and A. S.-C. Cheung, J. Chem. Phys. **112**, 9791 (2000).

[12] M. C. G. N. van Vroonhoven and G. C. Groenenboom, J. Chem. Phys. **116**, 1954 (2002), Chapter 2 of this thesis.

[13] M. C. G. N. van Vroonhoven and G. C. Groenenboom, J. Chem. Phys. **116**, 1965 (2002), Chapter 3 of this thesis.

[14] B. Zygelman, A. Dalgarno, and R. D. Sharma, Phys. Rev. A **49**, 2587 (1994).

[15] B. Zygelman, A. Dalgarno, and R. D. Sharma, Phys. Rev. A **50**, 3920 (1994).

[16] D. R. Bates, Proc. Phys. Soc. London, Sect. B **64**, 805 (1951).

[17] R. P. Saxon and B. Liu, J. Chem. Phys. **67**, 5432 (1977).

[18] H. Partridge, C. W. Bauschlicher, Jr., S. R. Langhoff, and P. R. Taylor, J. Chem. Phys. **95**, 8292 (1991).

[19] A. Jenouvrier, M.-F. Mérienne, B. Coquart, M. Carleer, S. Fally, A. C. Vandaele, C. Hermans, and R. Colin, J. Mol. Spectrosc. **198**, 136 (1999).

[20] J. T. Hougen, J. Chem. Phys. **36**, 519 (1962).

[21] H. Lefebvre-Brion and R. W. Field, *Perturbations in the spectra of diatomic molecules*, Academic Press, New York, 1986.

[22] G. C. Groenenboom and D. T. Colbert, J. Chem. Phys. **99**, 9681 (1993), note the mistake in the signs between the two terms in the first and second part of Eq. (48). See also D. T. Colbert and W. H. Miller, J. Chem. Phys. **96**, 1982 (1992).

[23] M. Mizushima, *The Theory of Rotating Diatomic Molecules*, Wiley, New York, 1975.

[24] J. T. Hougen, *The calculation of rotational energy levels and rotational line intensities in diatomic molecules*, NBS Monograph 115, National Bureau of Standards, 1970, available online at http://physics.nist.gov/Pubs/Mono115/.

[25] J. H. van Vleck, Rev. Mod. Phys. **23**, 213 (1951).

[26] J. K. G. Watson, Mol. Phys. **19**, 465 (1970).

[27] G. Brocks, A. van der Avoird, B. T. Sutcliffe, and J. Tennyson, Mol. Phys. **50**, 1025 (1983).

[28] A. van der Avoird, P. E. S. Wormer, and R. Moszynski, Chem. Rev **94**, 1931 (1994).

[29] M. Larsson, Phys. Scripta **23**, 835 (1981).

[30] L. C. Biedenharn and J. D. Louck, *Angular Momentum in Quantum Physics*, volume 8 of *Encyclopedia of Mathematics*, Addison-Wesley, Reading, 1981.

[31] R. N. Zare, *Angular momentum*, Wiley, New York, 1988.

Chapter 5

Ab initio calculation of the intensities of the Herzberg I, II, and III bands of O_2

Abstract

We present an excitation mechanism for three spectroscopic systems of oxygen, the electric dipole-forbidden transitions Herzberg I: $A^3\Sigma_u^+ \longleftarrow X^3\Sigma_g^-$, Herzberg II: $c^1\Sigma_u^- \longleftarrow X^3\Sigma_g^-$, and Herzberg III: $A'\,^3\Delta_u \longleftarrow X^3\Sigma_g^-$, which are of atmospheric interest. The mechanism is based on *ab initio* potential energy curves, spin-orbit couplings, and orbit-rotation couplings. Pathways through several intermediate states are included: $^3\Sigma_g^+$ (1 state), $^3\Pi_g$, $^1\Pi_g$, $^3\Sigma_u^-$ (2 states of each symmetry), and $^3\Pi_u$ (3 states). The calculations are tested against experimental results [M.-F. Mérienne *et al.*, J. Mol. Spectr. **202**, 171 (2000)] for integrated line cross-sections of the Herzberg bands, for J up to 20. The intensity of the Herzberg I system originates from positive interference of $^3\Pi_g$ and $^3\Pi_u$ intermediates with further positive interference from $^3\Sigma_u^-$ for the stronger branches, and negative interference for the weaker ones. The agreement for the (2-0) band is almost perfect. The Herzberg II system involves destructive interference between $^1\Pi_g$ and $^3\Pi_u$ intermediates, the larger contribution is from $^1\Pi_g$. For this system the agreement with experiment is very good for low vibrational bands [(4-0)], but calculated intensities are too low for high $v'(\approx 10-17)$, probably due to a too repulsive inner wing of the Herzberg potentials. The intensity of the Herzberg III system is caused by $^3\Pi_u$ and $^3\Pi_g$ intermediate states. The agreement between experimental and calculated intensities is reasonably good for most branches, but not for branches where orbit-rotation interaction through $^3\Pi_g$ is important. An extra intermediate state of $^3\Pi_g$ symmetry might be needed to describe the Herzberg III intensity mechanism better.

5.1 Introduction

The O_2 molecule has six bound electronic states below its first dissociation limit. They are, in order of increasing energy, the ground state $X^3\Sigma_g^-$, two more gerade states $a^1\Delta_g$ and $b^1\Sigma_g^+$, and three ungerade states, $c^1\Sigma_u^-$, $A'\ ^3\Delta_u$, and $A^3\Sigma_u^+$. All transitions between these six states are forbidden in the electric dipole approximation. Transitions from the ground state to the three ungerade states become allowed when spin-orbit and orbit-rotation interactions with other (intermediate) states are taken into account. These transitions are known as the Herzberg transitions, they are numbered according to their intensity. Herzberg I, II, and III correspond to $A^3\Sigma_u^+ \longleftarrow X^3\Sigma_g^-$, $c^1\Sigma_u^- \longleftarrow X^3\Sigma_g^-$, and $A'\ ^3\Delta_u \longleftarrow X^3\Sigma_g^-$ respectively.

Exact knowledge of the mechanisms by which these transitions obtain their intensity is important in atmospheric photochemistry, where there is still discussion on the total Herzberg continuum cross-section.[1,2] Buijsse *et al.*[1] calculated continuum cross-sections using the effective transition moments adopted by them. These were based on experimental line oscillator strengths, extrapolated into the continuum and partly on *ab initio* calculations by Klotz and Peyerimhoff.[3] These cross-sections are consistent with the corresponding discrete oscillator strength densities, as is required by the principle of continuity across a dissociation limit.[4] However, the total Herzberg continuum cross-section measured by Amoruso[5] is ≈ 13 % lower than the Herzberg I cross-section of Buijsse, based on extrapolation of the discrete spectrum.

The excitation mechanism is also important for a correct description of oxygen photodissociation. The photofragment fine structure branching ratio, angular distribution and alignment depend on and thus give indirect information on the excitation mechanism. Branching ratios and angular distributions were measured by Buijsse *et al.*[1] In previous work[6] we calculated these, employing *ab initio* potentials and couplings, semiclassical dynamics, and the semi-empirical excitation model of Buijsse. The agreement between theory and experiment is not yet perfect. A full quantum dynamical scattering calculation of the photodissociation of O_2 in the Herzberg continuum, employing our potentials and couplings and the *ab initio* excitation mechanism from this chapter is in progress.

Our excitation model consists of several pathways. Each pathway is an electric dipole allowed transition from the ground state to the Herzberg state via an intermediate state that is a perturber of either the ground or the Herzberg state through spin-orbit or orbit-rotation coupling. Electric dipole transitions between perturbers of ground and Herzberg states have not been considered. Klotz and Peyerimhoff[3] performed *ab initio* calculations of electronic transition moments for the Herzberg transitions. They did not include orbit-rotation interactions, which means they do not have a pathway for the $\Omega = 3$ subband of the Herzberg III system. Furthermore they do not give separate transition dipole moment matrix elements and spin-orbit coupling matrix elements, but only the R-dependent electronic transition moments (which are the absolute values of products of spin-orbit coupling and transition dipole). Therefore the information on the relative phases of the pathways is lost. This phase information is needed in the calculation of photofragment angular distributions and alignment. Our electronic transition moments compare very well with those of Klotz and Peyerimhoff, when we include the same intermediate states. However, we will show that orbit-rotation interactions and at least one more intermediate state of $^3\Pi_u$ symmetry is needed to describe the intensity in the Herzberg systems.

To test our *ab initio* excitation model, we calculate intensities for the bound-bound transitions in the Herzberg bands. Many studies of the intensities of these bands have been performed, photographic measurements, and also with modern techniques as cavity-ringdown spectroscopy and Fourier transform spectroscopy (FTS). We compare our calculated results with the most recent FTS results. Yoshino and coworkers performed FTS, and presented integrated line cross-sections on the (4,0) – (11,0) bands of Herzberg I,[7] the (7,0) – (16,0) bands of Herzberg II,[8] and on the (6,0) – (10,0) $\Omega = 1$ subbands and (5,0) – (11,0) $\Omega = 2$ subbands of Herzberg III.[9] Mérienne *et al.*[10] present extended FTS measurements of integrated line cross-sections on the Herzberg I (0,0) – (11,0), Herzberg II (2,0) – (19,0), and Herzberg III (2,0) – (12,0) bands. They present data for higher rotational quantum numbers, and on more branches. They also present data on the $\Omega = 3$ subband of Herzberg III.

The outline of this chapter is as follows. In the next section we explain the theory used to calculate *ab initio* integrated line cross-sections. Sec. 5.3 gives all computational details. The results are presented and discussed in Sec. 5.4, where we also compare them with experiment, and finally a conclusion is given in Sec. 5.5.

5.2 Theory

5.2.1 Excitation model

As has been explained in the introduction, the excitation model consists of several intermediate states, of different symmetries: $^3\Sigma_g^+$ (1 state), $^3\Pi_g$, $^1\Pi_g$, $^3\Sigma_u^-$ (2 states of each symmetry), and $^3\Pi_u$ (3 states). The gerade intermediate states couple with the ground state, through spin-orbit or orbit-rotation interactions, and have an electric-dipole allowed transition to one or more Herzberg states. There is a dipole transition from the ground state to the ungerade intermediate states, which perturb the Herzberg states, again through spin-orbit and orbit-rotation couplings. Bellary and Balasubramanian[11] found that thirteen independent moments are needed to describe a general $^3\Sigma^\pm \longleftarrow {}^3\Sigma^\mp$ transition. In the case of Herzberg I, England *et al.*[12] were able to repro-

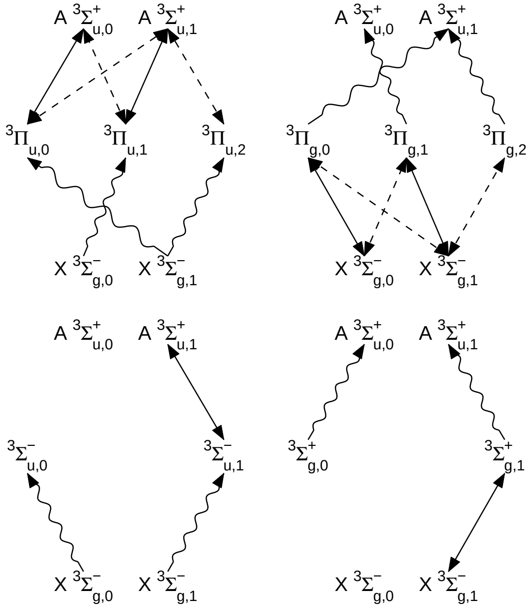
A $^3\Sigma^+_{u,0}$
A $^3\Sigma^+_{u,1}$
$^3\Pi_{u,0}$
$^3\Pi_{u,1}$
$^3\Pi_{u,2}$
X $^3\Sigma^-_{g,0}$
X $^3\Sigma^-_{g,1}$
A $^3\Sigma^+_{u,0}$
A $^3\Sigma^+_{u,1}$
$^3\Pi_{g,0}$
$^3\Pi_{g,1}$
$^3\Pi_{g,2}$
X $^3\Sigma^-_{g,0}$
X $^3\Sigma^-_{g,1}$
A $^3\Sigma^+_{u,0}$
A $^3\Sigma^+_{u,1}$
$^3\Sigma^-_{u,0}$
$^3\Sigma^-_{u,1}$
X $^3\Sigma^-_{g,0}$
X $^3\Sigma^-_{g,1}$
A $^3\Sigma^+_{u,0}$
A $^3\Sigma^+_{u,1}$
$^3\Sigma^+_{g,0}$
$^3\Sigma^+_{g,1}$
X $^3\Sigma^-_{g,0}$
X $^3\Sigma^-_{g,1}$

Figure 5.1: Pathways included in the present excitation mechanism for the Herzberg I transition. All Ω components are listed, wiggly arrows indicate an allowed electric dipole transition, solid double-headed arrows indicate spin-orbit coupling, and dashed double headed arrows indicate orbit-rotation coupling.

duce the measured line strengths with only six independent moments, with the main sources of intensity from $^3\Sigma^-_u$, $^3\Pi_g$, and $^3\Pi_u$ intermediates. The electronic pathways in our excitation mechanism for the Herzberg I transition are shown in Fig. 5.1. The pathways have been split per intermediate state symmetry. There are no direct pathways from the ground state to Herzberg I through the $^1\Pi_g$ intermediate state, this state has only direct pathways to $c^1\Sigma^-_u$ and contributes only indirectly through the spin-orbit coupling between $A^3\Sigma^+_u$ and $c^1\Sigma^-_u$. Watson showed in a general treatment of $^1\Sigma \longleftarrow {}^3\Sigma$ transitions that only one moment suffices to describe the intensity of the Herzberg II system, and that the intermediate states are of $^1\Pi_g$ and $^3\Pi_u$ symmetry. The number of pathways from the ground state to $c^1\Sigma^-_u$ is much smaller than for the Herzberg I transition, see Fig. 5.2. Only $^1\Pi_{g,1}$ and $^3\Pi_{u,0}$ intermediate states contribute directly to the intensity of Herzberg II, with spin-orbit coupling. Other pathways can only contribute through spin-orbit coupling of $c^1\Sigma^-_u$ with $A^3\Sigma^+_u$. In general six moments are needed to describe the intensity in a $^3\Delta \longleftarrow {}^3\Sigma$ transition,[13] one parallel and five perpendicular, where the parallel moment is zero in first order. The perpendicular moments arise

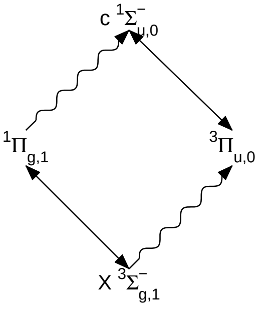
c $^1\Sigma^-_{u,0}$
$^1\Pi_{g,1}$
$^3\Pi_{u,0}$
X $^3\Sigma^-_{g,1}$

Figure 5.2: Pathways included in the present excitation mechanism for the Herzberg II transition. Dipole transitions and couplings are coded in the same way as in Fig. 5.1

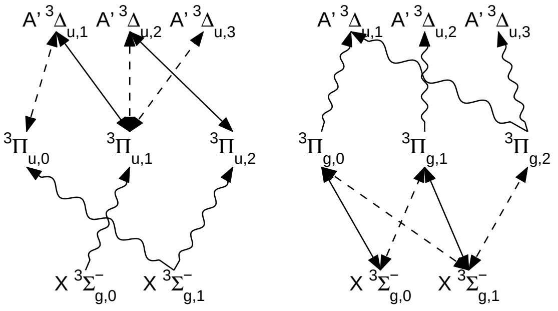
A' $^3\Delta_{u,1}$
A' $^3\Delta_{u,2}$
A' $^3\Delta_{u,3}$
$^3\Pi_{u,0}$
$^3\Pi_{u,1}$
$^3\Pi_{u,2}$
X $^3\Sigma^-_{g,0}$
X $^3\Sigma^-_{g,1}$
A' $^3\Delta_{u,1}$
A' $^3\Delta_{u,2}$
A' $^3\Delta_{u,3}$
$^3\Pi_{g,0}$
$^3\Pi_{g,1}$
$^3\Pi_{g,2}$
X $^3\Sigma^-_{g,0}$
X $^3\Sigma^-_{g,1}$

Figure 5.3: Pathways included in the present excitation mechanism for the Herzberg III transition. Dipole transitions and couplings are coded in the same way as in Fig. 5.1

from interactions with $^3\Pi_g$ and $^3\Pi_u$ intermediates. Huestis *et al.*[14] found that the Herzberg III transition is $\sim$ 99% perpendicular, which justifies our first-order description. The direct pathways for the Herzberg III transition taken into account in the present excitation mechanism are all through $^3\Pi_g$ and $^3\Pi_u$ intermediate states. They are shown in Fig. 5.3.

5.2.2 Integrated line cross-section

Assuming zero population of the excited states, the integrated line cross-section for an absorption from initial state i to final state f is given by Eq. (14-3) of Bunker and Jensen[15]

$$\sigma = \frac{4\pi^2\omega_{fi}}{c}\frac{e^{-E_i/kT}}{Z}|M_{fi}|^2. \tag{5.1}$$

Here ω_{fi} is the energy difference between initial and final state, c is the speed of light, E_i the energy of the initial state, k the Boltzmann constant, T the temperature, Z the total partition function of the ground state, $\exp(-E_i/kT)/Z$ the Boltzmann factor of the initial state, and M_{fi} the transition dipole matrix element between initial and final state. The total angular momentum quantum number J and its space-fixed projection M are good quantum numbers in both initial and final state and we have [Eq. (14-5) of Ref. 15]:

$$|M_{fi}|^2 = \frac{1}{3} \sum_{MM'm} |\langle J'M'f|\hat{\mu}_m^{\mathrm{SF}}|JMi\rangle|^2. \tag{5.2}$$

The three components $m = -1, 0, 1$ of the transition dipole moment matrix element are related by the Wigner-Eckart theorem. Using the orthogonality of $3j$ symbols,[16] we can write

$$|M_{fi}|^2 = \sum_{MM'} |\langle J'M'f|\hat{\mu}_0^{\mathrm{SF}}|JMi\rangle|^2. \tag{5.3}$$

The partition function is given by

$$Z = \sum_{v,J,N} (2J+1)e^{-E_{v,J,N}/kT}, \tag{5.4}$$

where the summation runs over all vibrational levels v and rotational levels (J, N), with rotational angular momentum quantum number N. The factor $2J + 1$ accounts for the degeneracy of the levels with total angular momentum J. Nuclear spin statistics for ^{16}O (a boson with nuclear spin $I = 0$) dictate that the total wave function is even under exchange of the nuclei P_{AB}, where $P_{\mathrm{AB}} = \hat{\pi} \cdot \hat{\imath}$, and $\hat{\pi}$ is electronic inversion, and $\hat{\imath}$ is total (electrons and nuclei) space-fixed inversion. The rotational and vibrational part of the wave function do not depend on the electronic coordinates, the phase of a wave function under $\hat{\pi}$ is given by the gerade/ungerade label, this phase is $+1$ for $X^3\Sigma_g^-$. The vibrational wave function depends only on the distance R, and is thus even under $\hat{\imath}$. The parity of the rotational part of the wave function is $(-1)^N$ and space-fixed inversion amounts to body-fixed reflection in the xz-plane for the electronic part, which has a phase of -1 for a Σ^- state (and $+1$ for Σ^+). The phase of the total wave function under P_{AB} is thus equal to the parity for gerade states. The parity of a rotational level (J, N) in the $X^3\Sigma_g^-$ ground state is given by $p = (-1)^{N+1}$, and all odd-parity ($p = -1$) levels are missing. Thus only odd N levels exist, and for each J, N may have the values $J - 1$, J, or $J + 1$. These three components are usually labeled[17] F_1, F_2, and F_3. The parity of a component is designated with a subscript e/f, with e meaning $+$ parity at $J = 0$, and f for $-$ parity at $J = 0$. Thus we have F_{1e} and F_{3e} components for even J and F_{2f} for odd J.

5.2.3 Hamiltonian

To evaluate the transition dipole matrix element needed in the calculation of integrated line cross-sections, we have to calculate the wave functions for the initial and final bound states. These wave functions are eigenfunctions of the total unperturbed, time-independent Hamiltonian

$$\hat{H} = \hat{H}_{\text{Coul}} + \hat{H}_{\text{SO}} + \hat{H}_{\text{vib}} + \hat{H}_{\text{rot}}, \tag{5.5}$$

where $\hat{H}_{\text{Coul}}$ is the usual Coulombic Hamiltonian in the clamped nuclei approximation and $\hat{H}_{\text{SO}}$ is the Breit-Pauli spin-orbit Hamiltonian.[18,19] The nuclear radial kinetic energy is

$$\hat{H}_{\text{vib}} = -\frac{\hbar^2}{2\mu}\frac{1}{R}\frac{\partial^2}{\partial R^2}R, \tag{5.6}$$

with μ the reduced mass and R the internuclear distance. The nuclear rotational Hamiltonian is expressed in two angle embedded body fixed operators, as in our previous work,[20]

$$\begin{aligned}\hat{H}_{\text{rot}} = \frac{1}{2\mu R}&[(\hat{J}^2 - \hat{J}_z^2) + (\hat{L}^2 - \hat{L}_z^2) + (\hat{S}^2 - \hat{S}_z^2)\\ &+ (\hat{L}^+\hat{S}^- + \hat{L}^-\hat{S}^+) - (\hat{L}^+\hat{J}^- + \hat{L}^-\hat{J}^+) - (\hat{S}^+\hat{J}^- + \hat{S}^-\hat{J}^+)],\end{aligned} \tag{5.7}$$

where $\underline{\hat{J}} = \underline{\hat{N}} + \underline{\hat{L}} + \underline{\hat{S}}$, $\underline{\hat{N}}$ is the angular momentum associated with the nuclear end-over-end rotation, $\underline{\hat{L}}$ is the electronic orbital angular momentum, and $\underline{\hat{S}}$ is the electron spin. In a diatomic molecule L is not a good quantum number, but generally the expectation value of $\hat{L}^2$ is only weakly R-dependent for a given electronic state.[21] Thus the $\hat{L}^2$ term induces only a shift in the electronic energy of a given electronic state of the order of $L(L+1)/2\mu R^2$, which is very small compared to the difference in electronic energies of the ground and final Herzberg states. We neglect this contribution. The spin-rotation term $(\hat{S}^{\pm}\hat{J}^{\mp})$ gives rise to intra-state coupling, needed to describe the F_1 and F_3 components of the states $X^3\Sigma_g^-$ and $A^3\Sigma_u^+$ correctly. The orbit-rotation term $(\hat{L}^{\pm}\hat{J}^{\mp})$ is one of the interactions giving intensity to the Herzberg bands, the intensity of the $\Omega = 3$ subband of the Herzberg III transition comes in first order solely from orbit-rotation interactions. The $\hat{L}^{\pm}\hat{S}^{\mp}$ rotational terms couple states that are also coupled by spin-orbit coupling. Although these rotational terms are smaller than the spin-orbit coupling, they are included in the present work.

To reproduce the ground state energies exactly, i.e. within 0.1 cm^{-1} for J up to 30, we included also the phenomenological spin-spin and spin-rotation Hamiltonian[22] for the ground $X^3\Sigma_g^-$ state,

$$\hat{H}_{\text{SS}} = \frac{2}{3}\lambda_0(3\hat{S}_z^2 - \hat{S}^2), \tag{5.8}$$

$$\hat{H}_{\text{NS}} = \mu_0\underline{\hat{N}} \cdot \underline{\hat{S}} = \mu_0\left[\hat{J}_z\hat{S}_z + \frac{1}{2}(\hat{S}^+\hat{J}^- + \hat{S}^-\hat{J}^+) - \hat{S}^2\right], \tag{5.9}$$

with $\lambda_0 = 1.98475070$ cm^{-1} and $\mu_0 = -8.425368 \times 10^{-3}$ cm^{-1}.

5.2.4 Bound state wave functions

In accordance with the variational principle wave functions are obtained by diagonalization of Eq. (5.5) in a basis. For a basis we use two angle embedded parity adapted electronic-rotation Hund's case (a) functions with parity p as defined in our previous work[20]

$$\begin{aligned} |m\Lambda S\Sigma JM\Omega p; R\rangle \equiv \frac{1}{\sqrt{2(1+\delta_{\Lambda,0}\delta_{\Sigma,0})}} \big[&|m\Lambda S\Sigma JM\Omega; R\rangle \\ &\pm p(-1)^J |m -\Lambda S -\Sigma JM -\Omega; R\rangle \big]. \end{aligned} \tag{5.10}$$

The + combination applies to basis functions for gerade electronic states, and the − to ungerade functions. We have

$$|m\Lambda S\Sigma JM\Omega; R\rangle \equiv \sqrt{\frac{2J+1}{4\pi}} D^{(J)*}_{M\Omega}(\alpha,\beta,0)|m\Lambda S\Sigma; R\rangle_{\mathrm{BF}}, \tag{5.11}$$

where α and β are the polar angles of the diatomic internuclear axis with respect to the space fixed frame, $D^{(J)*}_{M\Omega}(\alpha,\beta,0)$ is a rotational wave function for total angular momentum J and projections M and Ω of $\underline{\hat{J}}$ on the space fixed and body fixed z axis, respectively. The body fixed electronic wave functions are given by $|m\Lambda S\Sigma; R\rangle_{\mathrm{BF}} \equiv \hat{R}(\alpha,\beta,0)|m\Lambda S\Sigma; R\rangle_{\mathrm{SF}}$, where $|m\Lambda S\Sigma; R\rangle_{\mathrm{SF}}$ are the *ab initio* calculated eigenfunctions of $\hat{H}_{\mathrm{Coul}}$ and $\hat{R}(\alpha,\beta,0) \equiv e^{-i\alpha\hat{J}_z}e^{-i\beta\hat{J}_y}$ is the rotation operator that transforms the space fixed functions into body fixed functions. The m label is used to distinguish between different Hund's case (a) states with the same Λ and S.

The vibrational motion is treated by a sinc-function discrete variable representation (sinc-DVR).[23] The orthonormal radial basis functions $\phi_n(R) = \langle R|n\rangle = (1/\sqrt{\Delta})\mathrm{sinc}[\pi(R-R_n)/\Delta]$ are localized on the grid points $R_n = R_0 + n\Delta$, where $\mathrm{sinc}(x) \equiv \sin(x)/x$. The rotational-vibrational-electronic (RVE) basis functions used in the expansion of the bound state wave functions are products:

$$|m\Lambda S\Sigma JM\Omega pn\rangle \equiv |m\Lambda S\Sigma JM\Omega p; R\rangle\phi_n(R). \tag{5.12}$$

The functions $|m\Lambda S\Sigma JM\Omega; R\rangle$ are eigenfunctions of the body fixed angular momentum operators $\hat{J}^2, \hat{J}_z, \hat{S}^2, \hat{S}_z$, and $\hat{L}_z$, with eigenvalues $J(J+1)$, Ω, $S(S+1)$, Σ, and Λ respectively. In the evaluation of rotational Hamiltonian matrix elements we also use $\langle n|(2\mu R^2)^{-1}|n'\rangle = \delta_{n,n'}/(2\mu R_n^2)$. Matrix elements for the step up/step down angular momentum operators follow from

$$\hat{S}^{\pm}\hat{J}^{\mp}|m\Lambda S\Sigma JM\Omega;R\rangle = c_{\pm}(S,\Sigma)c_{\pm}(J,\Omega)|m\Lambda S\Sigma\pm 1JM\Omega\pm 1;R\rangle, \quad (5.13)$$

$$\hat{L}^{\pm}\hat{J}^{\mp}|m\Lambda S\Sigma JM\Omega;R\rangle = \sum_{m'} c_{\pm}(J,\Omega)\mathbf{L}^{\pm}_{m'\Lambda\pm 1S\Sigma;m\Lambda S\Sigma}(R)|m'\Lambda\pm 1S\Sigma JM\Omega\pm 1;R\rangle, \quad (5.14)$$

$$\hat{L}^{\pm}\hat{S}^{\mp}|m\Lambda S\Sigma JM\Omega;R\rangle = \sum_{m'} c_{\mp}(S,\Sigma)\mathbf{L}^{\pm}_{m'\Lambda\pm 1S\Sigma;m\Lambda S\Sigma}(R)|m'\Lambda\pm 1S\Sigma\mp 1JM\Omega;R\rangle, \quad (5.15)$$

where

$$\mathbf{L}^{\pm}_{m'\Lambda\pm 1S\Sigma;m\Lambda S\Sigma}(R) = {}_{\mathrm{SF}}\langle m'\Lambda\pm 1S\Sigma;R|\hat{L}^{\pm}|m\Lambda S\Sigma;R\rangle_{\mathrm{SF}} \quad (5.16)$$

is the *ab initio* calculated R dependent $\hat{L}^{\pm}$ matrix element and $c_{\pm}(j,m) = \sqrt{j(j+1)-m(m\pm 1)}$.

Bound eigenstates of the total Hamiltonian are calculated in three steps. In the first step we diagonalize $\hat{H}_{\mathrm{Coul}}+\hat{H}_{\mathrm{SO}}+\hat{H}_{\mathrm{rot}}$ in a basis of parity adapted electronic-rotation functions [Eq. (5.10)]. This diagonalization is performed for each point of the radial grid that is required for the calculation of vibrational wave functions, yielding Hund's case (c) potential energy curves and electronic eigenfunctions for each grid point. For the gerade (ground) state, the radial grid runs from $R = 1.42$ to 3.4, with a spacing of 0.045 $\mathrm{a_0}$; the grid for the ungerade (Herzberg) states starts at $R = 1.6$ $\mathrm{a_0}$, ends at 12 $\mathrm{a_0}$, also with a spacing of 0.045 $\mathrm{a_0}$. Thus the first 41 points of the ungerade grid coincide with points 5 – 45 of the gerade grid.

In the second step $\hat{H}_{\mathrm{vib}}+V_i$ is diagonalized for each of the Hund's case (c) potentials V_i from step 1. This yields vibrational wave functions as linear combinations of sinc-functions. The total wave function for a bound level in the i-th Hund's case (c) potential (which may be the ground state, or one of the Herzberg potentials), with vibrational quantum number v, rotational state (J,M), and parity p may then be written as

$$\Psi^{ivJMp} = \sum_{n}\left[\sum_{m,\Lambda,S,\Sigma,\Omega} c^{iJp}_{m\Lambda S\Sigma\Omega}(R_n)|m\Lambda S\Sigma JM\Omega p;R\rangle\right]\chi^{iv}_{n}\phi_n(R), \quad (5.17)$$

where $c^{iJp}_{m\Lambda S\Sigma\Omega}(R_n)$ is the coefficient of the rotational-electronic basis function $|m\Lambda S\Sigma JM\Omega p;R\rangle$ in the i-th electronic eigenfunction at $R = R_n$, and χ^{iv}_{n} is the value of the vibrational wave function in this grid point.

The potential energy curves of and the spin-orbit and orbit-rotation couplings with the intermediate states have only been calculated for R between 2.0 and 2.6 $\mathrm{a_0}$, in steps of 0.1 $\mathrm{a_0}$, the region where the ground state vibrational wave function is localized. Extrapolation of these quantities for all sinc-grid points up to $R = 12$ a$_0$ is not possible, therefore we excluded the intermediate states from the calculation of the Hund's case (c) potentials. Vibrational wave functions calculated with sinc-DVR are zero outside the grid by definition. In the calculation of the transition dipole moment matrix element, only the grid points common to both sinc-grids have to be included. In the third step we recalculate the electronic eigenfunctions for these grid points, now including the intermediate states.

5.2.5 Transition dipole matrix elements

From Eq. (5.3) we have

$$|M_{fi}|^2 = \sum_{M''M'} |M_{fM';iM''}|^2 = \sum_{M''M'} |\langle \Psi^{fv'J'M'p'}|\hat{\mu}_0^{\mathrm{SF}}|\Psi^{iv''J''M''p''}\rangle|^2 \quad (5.18)$$

Substituting Eq. (5.17) for the initial and final state wave functions, and employing the orthonormality of the sinc-DVR basis functions yields

$$\begin{aligned} M_{fM';iM''} = &\sum_n \sum_{\substack{m''\Lambda''S''\\ \Sigma''\Omega''}} \sum_{\substack{m'\Lambda'S'\\ \Sigma'\Omega'}} \chi_n^{fv'} c_{m'\Lambda'S'\Sigma'\Omega'}^{fJ'p'}(R_n) \\ &\times \langle m'\Lambda'S'\Sigma'J'M'\Omega'p';R_n|\hat{\mu}_0^{\mathrm{SF}}(R_n)|m''\Lambda''S''\Sigma''J''M''\Omega''p'';R_n\rangle \\ &\qquad\qquad\qquad \times \chi_n^{iv''} c_{m''\Lambda''S''\Sigma''\Omega''}^{iJ''p''}(R_n). \end{aligned} \quad (5.19)$$

The space fixed dipole operator $\hat{\mu}_0^{\mathrm{SF}}$ is given in body fixed operators by

$$\hat{\mu}_0^{\mathrm{SF}} = \sum_k \hat{\mu}_k^{\mathrm{BF}} D_{0k}^{(1)*}(\alpha,\beta,0). \quad (5.20)$$

The electronic transition dipole moment can be evaluated from the parity unadapted basis functions

$$\begin{aligned} \langle \Psi'|\hat{\mu}_0^{\mathrm{SF}}|\Psi''\rangle \equiv\ & \langle m'\Lambda'S'\Sigma'J'M'\Omega';R_n|\hat{\mu}_0^{\mathrm{SF}}(R_n)|m''\Lambda''S''\Sigma''J''M''\Omega'';R_n\rangle \\ = &\sum_k \frac{\sqrt{(2J'+1)(2J''+1)}}{4\pi} \\ &\times \int_{\alpha=0}^{2\pi}\int_{\beta=0}^{\pi} D_{M'\Omega'}^{(J')}(\alpha,\beta,0) D_{0k}^{(1)*}(\alpha,\beta,0) D_{M''\Omega''}^{(J'')*}(\alpha,\beta,0)\sin\beta d\alpha d\beta \\ &\times\ {}_{\mathrm{BF}}\langle m'\Lambda'S'\Sigma'|\hat{\mu}_k^{\mathrm{BF}}(R_n)|m''\Lambda''S''\Sigma''\rangle_{\mathrm{BF}}. \end{aligned} \quad (5.21)$$

From the electronic part we have a selection rule $\Lambda' = k + \Lambda''$ and $\Sigma' = \Sigma''$. Thus we have $-\Omega' + k + \Omega = 0$, and we may write

$$\int_{\alpha=0}^{2\pi}\int_{\beta=0}^{\pi} D^{(J')}_{M'\Omega'}(\alpha,\beta,0)D^{(1)*}_{0k}(\alpha,\beta,0)D^{(J'')*}_{M''\Omega''}(\alpha,\beta,0)\sin\beta d\alpha d\beta$$
$$= \frac{1}{2\pi}\int_{\alpha=0}^{2\pi}\int_{\beta=0}^{\pi}\int_{\gamma=0}^{2\pi} D^{(J')}_{M'\Omega'}(\alpha,\beta,\gamma)D^{(1)*}_{0k}(\alpha,\beta,\gamma)D^{(J'')*}_{M''\Omega''}(\alpha,\beta,\gamma)\sin\beta d\alpha d\beta d\gamma$$
$$= 4\pi(-1)^{M'-\Omega'}\begin{pmatrix} J' & 1 & J'' \\ -\Omega' & k & \Omega'' \end{pmatrix}\begin{pmatrix} J' & 1 & J'' \\ -M' & 0 & M'' \end{pmatrix}, \tag{5.22}$$

where we used Appendix V of Brink and Satchler[24] in the last step. This results in

$$\langle\Psi'|\hat{\mu}_0^{\mathrm{SF}}|\Psi''\rangle = (-1)^{J'+M'}\begin{pmatrix} J' & 1 & J'' \\ -M' & 0 & M'' \end{pmatrix}\widetilde{M}_{\Psi',\Psi''} \tag{5.23}$$

where the M-independent part of $\langle\Psi'|\hat{\mu}_0^{\mathrm{SF}}|\Psi''\rangle$ is given by

$$\widetilde{M}_{\Psi',\Psi''} = \sum_k \sqrt{(2J'+1)(2J''+1)}(-1)^{J'+\Omega'}\begin{pmatrix} J' & 1 & J'' \\ -\Omega' & k & \Omega'' \end{pmatrix}$$
$$\times \ {}_{\mathrm{BF}}\langle m'\Lambda'S'\Sigma'|\hat{\mu}_k^{\mathrm{BF}}(R_n)|m''\Lambda''S''\Sigma''\rangle_{\mathrm{BF}}. \tag{5.24}$$

All rotational-electronic basis states involved in a particular bound state have the same J and M value, and the M-dependence is thus equal for all terms in the summation in Eq. (5.19). This M-dependence can be taken out of the summation, to yield

$$|M_{fi}|^2 = \left[\sum_{M''M'}\begin{pmatrix} J' & 1 & J'' \\ -M' & 0 & M'' \end{pmatrix}^2\right]$$
$$\times\left[\sum_n \chi_n^{iv}\chi_n^{fv'}\sum_{\substack{m''\Lambda''S'' \\ \Sigma''\Omega''}}\sum_{\substack{m'\Lambda'S' \\ \Sigma'\Omega'}} c^{fJ'p'}_{m'\Lambda'S'\Sigma'\Omega'}(R_n)c^{iJ''p''}_{m''\Lambda''S''\Sigma''\Omega''}(R_n)\widetilde{M}_{\Psi',\Psi''}\right]^2. \tag{5.25}$$

Basically, the transition dipole moment matrix element is an integral over R of the product of initial and final state vibrational wave functions times the R-dependent electronic transition dipole moment matrix element. Due to the use of sinc-function DVR for the radial basis, the integral becomes a summation over the part of the radial grid that is included in both initial and final state vibrational calculation. The orthogonality of $3j$ symbols [Appendix I of Ref. 24] can be used to find

$$\sum_{M''M'} \begin{pmatrix} J' & 1 & J'' \\ -M' & 0 & M'' \end{pmatrix}^2 = \frac{1}{3}. \tag{5.26}$$

5.3 Calculations

5.3.1 *Ab initio* potential energy curves

All *ab initio* calculations have been performed with the MOLPRO computer program package.[25] We calculated potential energies for the intermediate states in the range of R from 2.0 a_0 to 2.6 a_0, with a spacing of 0.1 a_0. Potential energies were calculated on the complete active space self consistent field plus internally contracted multireference configuration interaction (CASSCF+MRCI) level of theory, with a one-electron basis consisting of the uncontracted s, p, d, and f orbitals from the augmented correlation consistent polarized valence quadruple zeta (aug-cc-pVQZ) basis.[26] The calculation of the properties was by the use of the same one-electron basis. The spin-orbit integrals module can only handle uncontracted gaussian basis functions with $l \leq 3$.

The orbitals were optimized with the state-averaged CASSCF[27, 28] method, and adapted to $D_{\infty h}$ symmetry using the LQUANT option from MOLPRO. A separate state-averaged calculation was performed for each intermediate state symmetry, with equal weights for all states included. Each calculation included the ground state, all intermediate states of the symmetry under consideration, and the Herzberg states which have excitation pathways through the present intermediate state symmetry. The active space was selected to include the O_2 valence space, and one (σ-type) or two (π^x, π^y-type) extra (diffuse) orbitals, to describe the Rydberg intermediate states. The symmetry of the extra orbitals depends on the symmetry of the intermediate state. The $1s$ orbitals were fully optimized, but kept doubly occupied in all configurations. Table 5.1 lists all details for all calculations. There are two calculations for the ${}^3\Pi_g$ intermediates, one for the excitation pathways through $\langle A^3\Sigma_u^+|\hat{\mu}|{}^3\Pi_g\rangle$ and one for pathways via $\langle A'\ {}^3\Delta_u|\hat{\mu}|{}^3\Pi_g\rangle$. The difference in absolute energies of the ${}^3\Pi_g$ states between the two calculations is less than 30 cm^{-1}, except at the crossing of Rydberg and valence state, which is somewhat sharper in the calculation with $A^3\Sigma_u^+$. Orbitals for the ${}^3\Pi_g$ intermediates have been taken from the calculation with $A^3\Sigma_u^+$. These orbitals were subsequently used in an internally contracted MRCI calculation of the potential energies, including single and double excitations from all CAS configurations. We applied the Pople size consistency correction.[29]

Table 5.1: Details of the orbital optimization for intermediate state potential energies. The active space consists of the O_2 *valence orbitals, plus one orbital of the mentioned symmetries. The Herzberg states included in the state-averaging are listed, as well as the included number of intermediate states and their major electronic configurations.*

Intermediate	Number of states	Extra orbital	Herzberg states	Major configuration	
$^3\Pi_u$	3	σ_u	$A^3\Sigma_u^+$	Valence:	$2\sigma_g^2\ 2\sigma_u^2\ 3\sigma_g^2\ 1\pi_u^4\ 1\pi_g\ 3\sigma_u$
			$c^1\Sigma_u^-$		$2\sigma_g^2\ 2\sigma_u^2\ 3\sigma_g\ 1\pi_u^3\ 1\pi_g^4$
			$A'\ ^3\Delta_u$		$2\sigma_g^2\ 2\sigma_u\ 3\sigma_g^2\ 1\pi_u^4\ 1\pi_g^3$
				Rydberg:	$2\sigma_g^2\ 2\sigma_u^2\ 3\sigma_g^2\ 1\pi_u^4\ 1\pi_g\ 4\sigma_u$
$^3\Sigma_u^-$	2	π_u^x, π_u^y	$A^3\Sigma_u^+$	Valence:	$2\sigma_g^2\ 2\sigma_u^2\ 3\sigma_g^2\ 1\pi_u^3\ 1\pi_g^3$
				Rydberg:	$2\sigma_g^2\ 2\sigma_u^2\ 3\sigma_g^2\ 1\pi_u^4\ 1\pi_g\ 2\pi_u$
$^3\Sigma_g^+$	1	π_u^x, π_u^y	$A^3\Sigma_u^+$	Valence:	$2\sigma_g^2\ 2\sigma_u^2\ 3\sigma_g^2\ 1\pi_u^3\ 1\pi_g^2\ 2\pi_u$
$^3\Pi_g$	2	σ_g	$A^3\Sigma_u^+$	Valence:	$2\sigma_g^2\ 2\sigma_u^2\ 3\sigma_g\ 1\pi_u^4\ 1\pi_g^3$
				Rydberg:	$2\sigma_g^2\ 2\sigma_u^2\ 3\sigma_g^2\ 1\pi_u^4\ 1\pi_g\ 4\sigma_g$
$^3\Pi_g$	2	σ_g	$A'\ ^3\Delta_u$	Valence:	$2\sigma_g^2\ 2\sigma_u^2\ 3\sigma_g\ 1\pi_u^4\ 1\pi_g^3$
				Rydberg:	$2\sigma_g^2\ 2\sigma_u^2\ 3\sigma_g^2\ 1\pi_u^4\ 1\pi_g\ 4\sigma_g$
$^1\Pi_g$	2	σ_g	$c^1\Sigma_u^-$	Valence:	$2\sigma_g^2\ 2\sigma_u^2\ 3\sigma_g\ 1\pi_u^4\ 1\pi_g^3$
				Rydberg:	$2\sigma_g^2\ 2\sigma_u^2\ 3\sigma_g^2\ 1\pi_u^4\ 1\pi_g\ 4\sigma_g$

5.3.2 *Ab initio property matrix elements*

Spin-orbit ($\hat{H}_{\mathrm{SO}}$), electronic orbital angular momentum step up/down ($\hat{L}^{\pm}$), and transition dipole moment matrix elements are calculated from wave functions on the state averaged CASSCF level of theory. The one-electron basis and the states taken in the averaging are the same as for the energy calculations. The active space is again the O_2 valence space plus one extra orbital of the symmetries mentioned in Table 5.1. For the calculation of properties we enlarged the active space with four orbitals of $\delta_{g,u}$ symmetry, to include the most important dynamic correlation effects.

Fortran routines for the evaluation of property matrix elements are available upon request.[30] For the spin-orbit coupling we supply a routine to evaluate the fits for the reduced spin-orbit matrix elements ${}_{\mathrm{SF}}\langle m\Lambda S\Sigma; R||\hat{H}_{\mathrm{SO}}(R)|| m'\Lambda'S'\Sigma'; R\rangle_{\mathrm{SF}}$. Using the Wigner-Eckart theorem, the matrix elements are given in terms of these reduced matrix elements as

$$\begin{aligned}&{}_{\mathrm{SF}}\langle m\Lambda S\Sigma; R|\hat{H}_{\mathrm{SO}}(R)|m'\Lambda'S'\Sigma'; R\rangle_{\mathrm{SF}} = \\ &\quad (-1)^{S-\Sigma}\begin{pmatrix} S & 1 & S' \\ -\Sigma & k & \Sigma' \end{pmatrix} {}_{\mathrm{SF}}\langle m\Lambda S\Sigma; R||\hat{H}_{\mathrm{SO}}(R)||m'\Lambda'S'\Sigma'; R\rangle_{\mathrm{SF}}, \qquad (5.27)\end{aligned}$$

where $k = \Sigma - \Sigma'$. We define only reduced matrix elements for states with $\Lambda \geq 0$. In Ref. 31 we presented a relation for reduced spin-orbit matrix elements for states with negative Λ in the case where the asymptotic L quantum number is known:

$$\langle (L) - \Lambda S || \hat{H}_{\mathrm{SO}} || (L') - \Lambda' S' \rangle = (-1)^{L+L'+1} \langle (L) \Lambda S || \hat{H}_{\mathrm{SO}} || (L') \Lambda' S' \rangle. \quad (5.28)$$

This relation can also be used in the present case, also for the states where we do not have an asymptotic L quantum number. The phase relation between the negative-Λ and positive-Λ component has been chosen so that the above relation holds, for the asymptotic L values given in Table 5.2.

5.3.3 Diabatization

Potential energy curves and properties have been calculated at different levels of theory. The crossing point of Rydberg and valence intermediate states may shift between CASSCF and MRCI. To obtain smooth potentials and properties as function of R we diabatized the intermediate states. We have only one (valence character) $^3\Sigma_g^+$ intermediate state, so in this case the diabatic state is by definition equal to the adiabatic one.

For $^3\Sigma_u^-$, $^3\Pi_g$, and $^1\Pi_g$ we have two states, one of Rydberg and one of valence character. In these cases the diabatic states are defined by a 2×2 orthogonal transformation of the adiabatic states

$$\begin{bmatrix} \Psi_1 \\ \Psi_2 \end{bmatrix}_{\mathrm{diab}} = \begin{pmatrix} \cos\phi & -\sin\phi \\ \sin\phi & \cos\phi \end{pmatrix} \begin{bmatrix} \Psi_1 \\ \Psi_2 \end{bmatrix}_{\mathrm{adiab}}, \quad (5.29)$$

where the diabatization angle ϕ depends on R. The diabatization angle is optimized so that the resulting diabatic potential energies can be fitted with a minimal residue to Morse curves (the diagonal potentials) and straight lines (for the off-diagonal diabatic potentials). The diabatization procedure is

1. Calculate initial diabatization angle in all grid points by diagonalization of the second moments of the electron density ($\sum_i x_i^2 + y_i^2$, where i runs over all electrons) on the basis $\{\Psi_1, \Psi_2\}_{\mathrm{adiab}}$.

2. Calculate initial diabatic energies in all grid points.

3. Fit Morse curve / straight line to diabatic energies by (non)linear least squares procedure, this yields the initial residue.

4. Calculate a new diabatization angle in the grid points by diagonalization of the fitted diabatic potentials. This gives the inverse transformation of Eq. (5.29).

5. Calculate new diabatic energies from the *ab initio* adiabatic energies and the new diabatization angle.

6. Fit new diabatic potentials, yielding a new residue.
7. Repeat steps 4 – 6 until the residue is at minimum.

This procedure was applied to both the CASSCF and MRCI states. The MRCI diabatic energies were fitted as potentials. The CASSCF diabatization angle was used to transform the property matrix elements, which were calculated at the CASSCF level, into diabatic properties. To illustrate the diabatization procedure we plot in Fig. 5.4 the diabatization angle [panel (a)] and off-diagonal potential energy [panel (b)] for the diabatization of the two $^3\Sigma_u^-$ intermediate states. The optimization procedure for the diabatization angle does not change the R-dependence of this angle very much. The off-diagonal potential becomes a smoother function of R. There is some difference between the CASSCF and CI results. The avoided crossing (in the adiabatic calculation) is sharper at

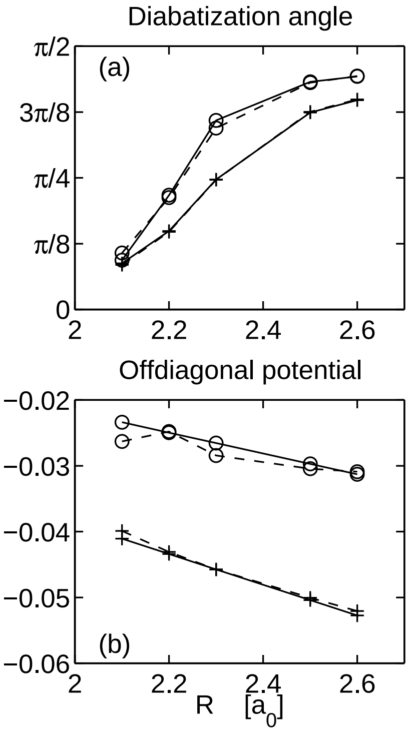

Figure 5.4: The diabatization angle ϕ in panel (a) and off-diagonal potential [panel (b)] for the diabatization of the two intermediate states of $^3\Sigma_u^-$ symmetry. Dashed lines: initial values from diagonalization of second moments, solid lines: final optimized values. CASSCF results are marked $+$, CI results have $\circ$ marks.

the CI level of theory. This is reflected in the diabatization angle, which goes faster from 0 to $\pi/2$ as a function of R, and in the off-diagonal potential, which is smaller. The crossing is localized where the derivative of the diabatization angle is maximal, this is at a smaller value of R for the CI results.

We have taken three ${}^3\Pi_u$ intermediate states into account. One of them, the lowest at $R = 2.0$ a$_0$, is clearly of Rydberg character. This state crosses with the lowest valence state. The third ${}^3\Pi_u$ state that we calculated has valence character in the $2 - 2.6$ a$_0$ region and does not cross the other ${}^3\Pi_u$ states. The potential and properties involving this third ${}^3\Pi_u$ state are rather smooth as a function of R, and the ${}^3\Pi_u$ states are diabatized by choosing the third diabatic state equal to the third adiabatic state, and diabatizing the first and second ${}^3\Pi_u$ state using the procedure described above.

5.3.4 Fitting

To calculate bound states and transition intensities, we need to interpolate the calculated diabatic potential energies for the intermediate states, the transition dipole matrix elements, and the spin-orbit and $\hat{L}$ interaction matrix elements. Therefore, we fitted the diagonal diabatic energies to Morse curves

$$V(R) = D_e \left\{1 - \exp[-\beta(R - R_0)]\right\}^2 + V_\infty \tag{5.30}$$

in a nonlinear least squares fit, with equal weights for all grid points. In this fitting procedure, the dissociation energy D_e and the potential energy for $R \to \infty$, V_∞, are treated as linear parameters. The exponent β and the minimum R_0 are non-linear parameters.

The diagonal potential energy for the third diabatic ${}^3\Pi_u$ state yielded unphysical results (negative β) when fitted with the functional form of the Morse curve, as it looks more like a straight line. We fitted it with a second degree polynomial in R. The off-diagonal diabatic potentials were fitted with a linear function of R, as mentioned above. The property matrix elements (reduced spin-orbit, transition dipole and $\hat{L}$ matrix elements) were also fitted with a first or second degree polynomial in R.

5.3.5 Fortran implementation of *ab initio* results

We supply a fortran implementation (available upon request[30]) of the fits of the diabatized potential energy curves (diagonal and off-diagonal), reduced spin-orbit matrix elements, orbit-rotation matrix elements, and transition dipole matrix elements. The routines for the potential energy curves are

```
subroutine diabatic_potentials (R, i, E)
subroutine diabatic_offdiag_potentials (R, i, j, E)
```

with input parameters the internuclear distance (`real*8 R`) and the state sequence number (`integer i` for the diagonal potential energies, and `integer`

Table 5.2: State sequence numbers and asymptotic values for the L quantum number.

State	Seq. no.	Asymptotic L value
$X^3\Sigma_g^-$ (ground)	14	1
$c^1\Sigma_u^-$ (Herzberg II)	2	1
$A'\ {}^3\Delta_u$ (Herzberg III)	3	2
$A^3\Sigma_u^+$ (Herzberg I)	5	0
$1\ {}^3\Pi_u$	9	2
$2\ {}^3\Pi_u$	10	2
$3\ {}^3\Pi_u$	11	2
Rydberg ${}^3\Sigma_u^-$	12	
Valence ${}^3\Sigma_u^-$	13	
${}^3\Sigma_g^+$	15	
Rydberg ${}^3\Pi_g$	16	1
Valence ${}^3\Pi_g$	17	1
Rydberg ${}^1\Pi_g$	18	2
Valence ${}^1\Pi_g$	19	2

`i,j` for bra and ket state in the off-diagonal routine). All electronic states have been given sequence numbers, which are specified in Table 5.2. The energy (in atomic units) is returned in the output parameter `real*8 E`. The diagonal potentials routine yields for sequence numbers 1 to 8 the potential energy curves calculated in Ref. 31, with the original numbering of states. For the ground state (number 14) the routine yields the potential energy curve from Babb *et al.*[32, 33]

The calling sequence to the spin-orbit routine is

```
subroutine spinorbit (R, i, j, A)
```

where `real*8 R` is again the internuclear distance and `integer i, j` are the bra and ket state sequence numbers. The value of the reduced matrix element $\langle i||\hat{H}_{\mathrm{SO}}(R)||j\rangle$ is returned in the output parameter `real*8 A`. For bra and ket state sequence numbers ≤ 8, this routine yields the reduced spin-orbit matrix elements from Ref. 31.

For the evaluation of $\mathbf{L}_{i,j}^{\pm} = \langle i|\hat{L}^{\pm}|j\rangle$ we have three routines

```
subroutine Lplus (i, j, Lambda_i, Lambda_j, or_number)
subroutine Lminus (i, j, Lambda_i, Lambda_j, or_number)
subroutine orbit_rotation_polynomials (R, or_number, A)
```

The first two have as input parameters the sequence numbers of bra and ket states (`integer i, j`) and the Λ quantum numbers of bra and ket (`integer Lambda_i, Lambda_j`), and yield the number of the R-dependent orbit-rotation matrix element (`integer or_number`) that has to be evaluated. The third routine evaluates this matrix element, at given internuclear distance R (`real *8 R`). The result is returned in `real*8 A`.

For the transition dipole matrix elements

$$\mu_{i\Lambda_i,j\Lambda_j} \equiv {}_{\mathrm{BF}}\langle i\Lambda_i| \sum_k \hat{\mu}_k^{\mathrm{BF}} |j\Lambda_j\rangle_{\mathrm{BF}} \tag{5.31}$$

we have again two routines:

```
      subroutine dipole_moments
     +    (i, j, Lambda_i, Lambda_j, dip_num, factor)
      subroutine dipole_polynomials (R, dip_num, A)
```

The first (setup) routine calculates the sequence number of the R-dependent transition dipole matrix element (`integer dip_num`) to be evaluated, given the bra and ket sequence numbers and Λ quantum numbers. It also calculates the factor (`real*8 factor`) with which the R-dependent matrix element has to be multiplied to yield $\mu_{i\Lambda_i,j\Lambda_j}$. The second routine calculates the R-dependent transition dipole matrix elements.

5.3.6 Bound state and intensity calculations

The diabatized fitted *ab initio* results have been used subsequently in a MATLAB program to evaluate the integrated line cross-sections. The program starts with the calculation of Hund's case (c) potential energy curves, performs sinc-DVR to calculate vibrational wave functions, and calculates electronic eigenfunctions for the sinc-DVR grid points common to initial and final states. The partition function Z for the ground state formally includes a sum over all rotation-vibration levels. The contribution of a level decreases exponentially when the energy of the level increases. We included only $v = 0$ and 1, and $J = 0$ up to 50 in the numerical calculation of Z. The transition dipole moment matrix elements and integrated line cross-sections are evaluated from the bound state wave functions.

5.4 Results and discussion

5.4.1 *Ab initio* potential energy curves

In Fig. 5.5 we show all diabatized potential energy curves used in the present calculations. Thin solid lines drawn over the full range of R represent the ground and Herzberg states. The ground state $v = 0$ and the $v = 6$ Herzberg II vibrational wave functions are also indicated. The intermediate states are only drawn in the region where they were calculated, which coincides with the region where the ground state vibrational wave function is localized. The

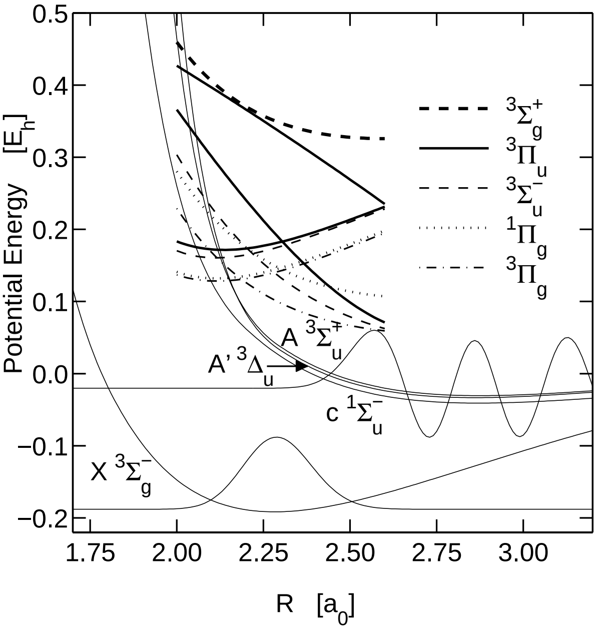

Figure 5.5: Diabatized potential energy curves for all electronic states included in the intensity calculations. The ground and Herzberg states are marked with their names, the intermediate states are only shown between 2.0 and 2.6 a$_0$. *The* $v = 0$ $X^3\Sigma_g^-$ *and* $v = 6$ $c^1\Sigma_u^-$ *vibrational wave functions are also plotted.*

Herzberg potential energy curves cross the intermediate state curves at $R < 2.2$ a$_0$. As we did not diabatize the electronic-rotational basis states after inclusion of all electronic-rotational couplings, the electronic eigenfunction coefficients $c^{iJp}_{m\Lambda S\Sigma\Omega}(R_n)$ may vary rapidly as a function of R at the crossings, after inclusion of the couplings with the intermediate states in the third step of the bound state calculation. The R-dependent electronic transition dipole moment matrix element will also vary rapidly with R in this region. The transition dipole moment matrix element is an integral over the product of both vibrational wave functions, multiplied by the R-dependent electronic transition dipole moment [the summation over n in Eq. (5.19)]. Since the Herzberg state vibrational wave functions are localized at larger R, and are almost zero for these small R values, this adiabatic approximation does not affect the calculated total transition dipole matrix elements and integrated line cross-sections, as we will show later.

In Fig. 5.6 we show the results of the diabatization process for the two states of $^3\Sigma_u^-$ symmetry. In the upper panel (a), we show the adiabatic energies (× marks) and the resulting diabatic potential energy curves (solid lines). For

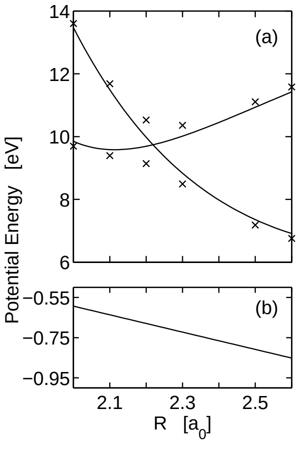

Figure 5.6: Diabatization of the two $^3\Sigma_u^-$ *intermediate states. The upper panel (a) plots the adiabatic energies with* × *marks, and the diabatic diagonal potentials as solid lines. The lower panel (b) gives the offdiagonal potential*

easier comparison with literature semi-empirical results,[34] the zero point of energy is at the minimum of the ground state potential, the energy units are electron volt. The lower panel (b) shows the off-diagonal diabatic potential energy curve. Li *et al.*[35] performed in 1992 *ab initio* MRD-CI calculations in a smaller one-electron basis, with 17 reference configurations, they diabatized their states by diagonalization of $\sum_i x_i^2 + y_i^2$, two components of the electric quadrupole tensor, in the same way as the initial guess for the diabatization in the present work has been constructed. Their diagonal diabatic potentials are shown in Fig. 1 of Ref. 35, they do not present the off-diagonal potential curve. Lewis *et al.* give semi-empirical potential energy curves in Fig. 1 of Ref. 34. They report a constant off-diagonal potential matrix element of 0.500 eV between the valence and lowest Rydberg state.

In Tables 5.3 and 5.4 we compare some features of our potentials with literature results. The R values of the minimum in the Rydberg curve and of the Rydberg-valence crossing are in good agreement. The excitation energies in the present calculation are about 0.3 eV (3 %) larger than in the semi-empirical results. The excitation energies calculated by Li are about 0.5 eV larger than the semi-empirical results at $R = 2.0$ a$_0$, but they agree very well at $R = 2.6$ a$_0$. Thus the shape of our present potentials resembles the shape of the semi-empirical results, whereas the calculation by Li gave a different shape. The separation between the two adiabatic potentials at the Rydberg-valence crossing is equal to twice the absolute value of the off-diagonal potential between the diabatic states at the crossing. The sign of the off-diagonal potential depends on the sign of the wave functions, which is arbitrary.

Table 5.3: Features of the Rydberg minimum and the Rydberg-Valence crossing of $^3\Sigma_u^-$ *potentials. Comparison of our present curves with ab initio results from Li et al.*[35] *and semi-empirical results from Lewis et al.*[34] *R values are in* a_0 *and energies in eV.*

	Minimum in Rydberg		Rydberg-Valence crossing		
	R	V	Adiabatic separation	R	V
Li	2.15	9.54	1.12	2.25	9.68
Present	2.11	9.58	1.39	2.22	9.74
Lewis	2.19	9.3	1.0	2.23	9.45

The diabatization process for the states of $^3\Pi_u$ symmetry is shown in Fig. 5.7. The potential energies are again in electron volt, with respect to the minimum in the ground state potential. Since the third diabatic state was chosen to be equal to the third adiabatic state, there is only one off-diagonal potential matrix element, between the first and the second diabatic $^3\Pi_u$ state. After comparison of our first two diabatic states with the semi-empirical results in Fig. 3 of Ref. 34, we see that our excitation energies differ again by about 3 % from the semi-empirical results. Our off-diagonal potential matrix element is again about 30 % larger. Diabatization of the $^1\Pi_g$ and $^3\Pi_g$ yields similar results, for these symmetries no experimental results are available.

5.4.2 *Ab initio properties*

The reduced spin-orbit matrix elements $\langle i||\hat{H}_{\text{SO}}(R)||j\rangle$ are shown in Fig. 5.8, labeled with (i,j), where i and j are the state sequence numbers from Table 5.2. In panel (a) we show matrix elements between $A^3\Sigma_u^+(j=5)$ and ungerade intermediate states, panel (b) presents matrix elements between the ungerade intermediate states and $A'\,^3\Delta_u$ or $c^1\Sigma_u^-(j=2 \text{ or } 3)$, panel (c) lists matrix elements between $^3\Pi_u(i,j=9,10,11)$ and $^3\Pi_g\ (i,j=16,17)$ intermediate states and the matrix elements between the ground state $X^3\Sigma_g^-(i=14)$ and

Table 5.4: Values for $^3\Sigma_u^-$ *potentials*

	$R=2.0$		$R=2.6$	
	Rydberg	Valence	Rydberg	Valence
Li	10.0	14.2	11.1	7.0
Present	9.85	13.47	11.42	6.91
Lewis	9.45	≈ 13	11.1	≈ 6.8

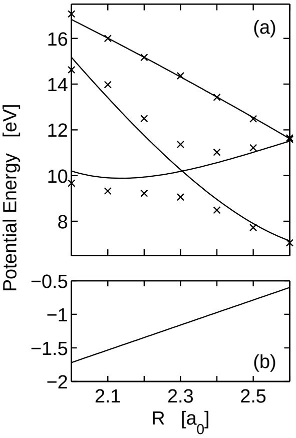

Figure 5.7: Diabatization of the $^3\Pi_u$ intermediate states. See the caption of Fig. 5.6 for an explanation.

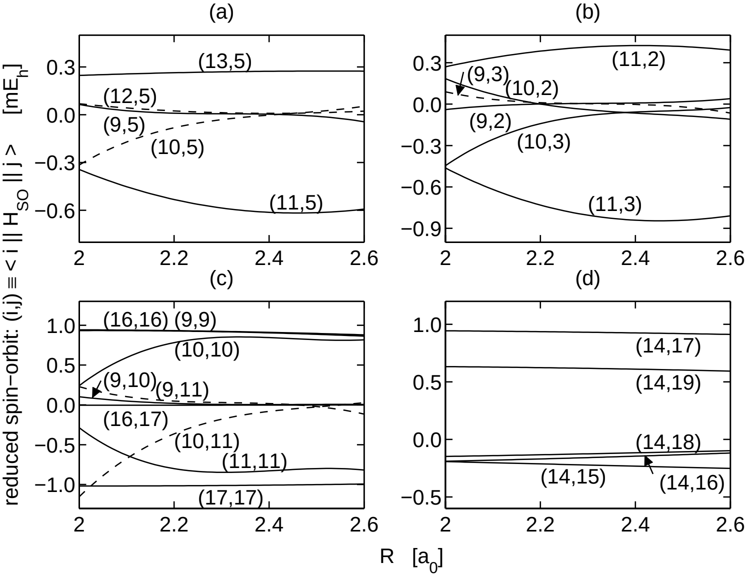

Figure 5.8: Reduced spin-orbit matrix elements $\langle i||\hat{H}_{\text{SO}}(R)||j\rangle$ are labeled as (i, j), where i and j are the state sequence numbers from Table 5.2. The energy units are mE_h.

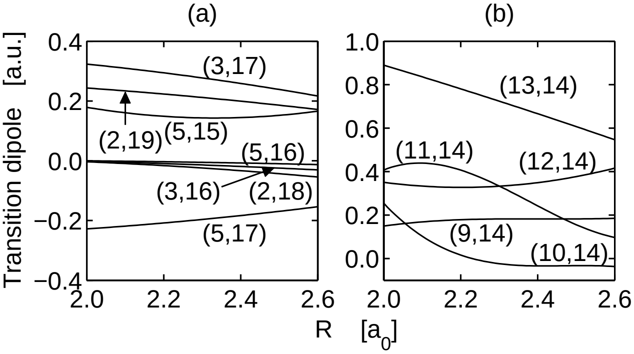

Figure 5.9: Transition dipole matrix elements $(i,j) \equiv \mu_{i\Lambda_i,j\Lambda_j}$ *with* $\Lambda_i, \Lambda_j \geq 0$ *in atomic units.*

gerade intermediate states are shown in panel (d). It can be noted that spin-orbit matrix elements involving an intermediate state of Rydberg character (numbers 9, 12, 16, and 18) and a valence (ground or Herzberg) state are always small. Spin-orbit matrix elements between ground/Herzberg states and valence-character intermediate states are much larger. Furthermore we note that the spin-orbit matrix elements of the third diabatic $^3\Pi_u$ state (nr 11) are larger than the matrix elements of the second diabatic state, nr 12. The diagonal matrix elements $\langle i^3\Pi||\hat{H}_{\rm SO}(R)||i^3\Pi\rangle$ in panel (c) are large, whereas the off-diagonal matrix elements $\langle i^3\Pi||\hat{H}_{\rm SO}(R)||j^3\Pi\rangle$ are generally almost zero, indicating the success of Rydberg - valence separation in the diabatization. The only large matrix element of this type is between the second [seq. number 10] and third [number 11] diabatic $^3\Pi_u$ state, which have both a valence character. This is caused by the choice of the third diabatic state being equal to the third adiabatic state. At small R the second and third adiabatic $^3\Pi_u$ states have only a small energy separation, and this choice does not yield a perfect diabatization. This causes a large off-diagonal spin-orbit matrix element, and a strong R-dependence of the spin-orbit matrix elements involving the second or third diabatic $^3\Pi_u$ state.

The diabatized transition dipole matrix elements are shown in Fig. 5.9. The matrix element $\mu_{i\Lambda_i,j\Lambda_j}$ with $\Lambda_i, \Lambda_j \geq 0$ is labeled as (i,j). In the left panel [(a)] the transition dipole matrix elements from gerade intermediate states to the Herzberg states are plotted, and in the right panel [(b)] the matrix elements between the ground state and the ungerade intermediate states. Transition dipole matrix elements involving the Rydberg $^1\Pi_g$ and $^3\Pi_g$ states [numbers 18 and 16 respectively] are again small, but the matrix elements involving the Rydberg $^3\Pi_u$ and $^3\Sigma_u^-$ states [numbers 9 and 12] are comparatively large (0.18 and 0.34 a.u. at $R = 2.3$ a$_0$ respectively). These values are in good agreement with the semi-empirical results in the lower panels of Figs. 3 and 1 of Ref. 34,

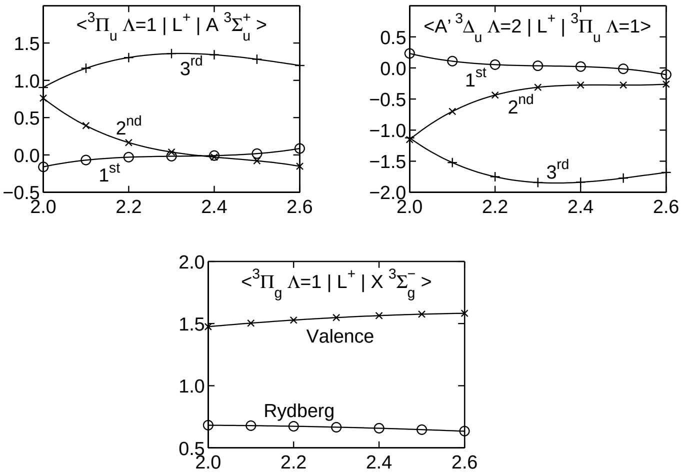

Figure 5.10: $\hat{L}^+$ matrix elements.

which yield approximately 0.2 and 0.3 respectively. The matrix elements for the transitions from the ground state [number 14] to the lowest valence $^3\Pi_u$ and $^3\Sigma_u^-$ states [numbers 10 and 13] compare also very well with the semi-empirical results: 0.03 and 0.72 in the present calculation, and 0.05 and 0.8 in Ref. 34, respectively.

Fig. 5.10 plots the calculated $\hat{L}^\pm$ matrix elements. The matrix elements for the first two diabatic $^3\Pi_u$ states are again small in the Franck-Condon region (around 2.5 a_0), and intensity through $^3\Pi_u$ intermediates comes from the third state, which has large matrix elements.

5.4.3 Effective electronic transition dipole moments

A previous *ab initio* study of the electronic excitation mechanism of the Herzberg systems was performed by Klotz and Peyerimhoff[3] (KP). To further test our calculations, we compare our results with theirs. They calculated effective electronic transition moments for the transitions between the three low-lying gerade electronic states of $O_2(X^3\Sigma_g^-, a^1\Delta_g$, and $b^1\Sigma_g^+)$ and the three ungerade Herzberg states. The initial and final states were obtained as a perturbation expansion of the eigenfunctions of $\hat{H}_{\text{Coul}} + \hat{H}_{\text{SO}}$, using MRD-CI wave functions as zero-order $\hat{H}_{\text{Coul}}$ solutions. The nuclear vibration and rotation were not taken into account. KP included intermediate states of the following symmetries: $^1\Pi_g(2)$, $^3\Pi_g(2)$, $^1\Delta_g$, $^3\Sigma_u^-$, $^1\Pi_u$ (2), $^3\Pi_u(2)$. Their effective electronic transition moments are given by the master equation

$$\mu_{a\to b} = \sum_k \frac{\langle a|\hat{H}_{\text{SO}}|k\rangle}{\Delta E_{ak}}\langle k|\hat{\mu}|b\rangle + \sum_{kl} \frac{\langle a|\hat{H}_{\text{SO}}|k\rangle}{\Delta E_{ak}}\langle k|\hat{\mu}|l\rangle\frac{\langle l|\hat{H}_{\text{SO}}|b\rangle}{\Delta E_{lb}}, \qquad (5.32)$$

Table 5.5: Effective electronic transition moments for spin-orbit transitions from the ground state to the Herzberg states, in 10^{-4} atomic units. Comparison between present results and results from KP.[3] *The column headed "all states" gives results where all intermediate states have been included, and the column headed "without 3 $^3\Pi_u$" presents the results when the third diabatic $^3\Pi_u$ intermediate state was omitted from the calculation.*

Transition	Present calculation		Ref. 3
	all states	without 3 $^3\Pi_u$	
U1: $c^1\Sigma^-_{u,0^-}$ — $X^3\Sigma^-_{g,\pm1}$	0.12	2.54	2.06
U3: $A'\ ^3\Delta_{u,2}$ — $X^3\Sigma^-_{g,\pm1}$	0.02	3.61	3.30
U5: $A'\ ^3\Delta_{u,1}$ — $X^3\Sigma^-_{g,0^+}$	0.04	3.60	3.35
U8: $A^3\Sigma^+_{u,\pm1}$ — $X^3\Sigma^-_{g,0^+}$	5.24	2.56	2.37
U9: $A^3\Sigma^+_{u,\pm1}$ — $X^3\Sigma^-_{g,\pm1}$	9.47	9.47	9.88
U12: $A^3\Sigma^+_{u,0^-}$ — $X^3\Sigma^-_{g,\pm1}$	5.32	2.50	2.44

where k, l runs over all states included in their calculation. All transitions from the ground state to the Herzberg states are listed in Table 5.5, with the numbering from KP. As the only mechanism for intensity in the $\Omega = 3$ subband of the Herzberg III transition is orbit-rotation interaction through $^3\Pi_2$ intermediate states, Klotz and Peyerimhoff do not have a transition from the $A'\ ^3\Delta_{u,3}$ to the ground state. Using our potential energy curves and spin-orbit matrix elements, we also calculated effective electronic transition moments for the KP transitions. We also ignored the nuclear rotation and vibration. Table 5.5 compares our results with results from Klotz and Peyerimhoff, who included only 2 intermediate states of $^3\Pi_u$ symmetry. Our transition moments compare very well with theirs if we include only the first (lowest) two diabatic $^3\Pi_u$ states. After inclusion of the third state we see an almost complete cancellation of the effective transition dipole moment for transitions U1, U3, and U5 to $c^1\Sigma^-_u$ and $A'\ ^3\Delta_u$. This cancellation is caused by destructive interference of different pathways contributing to the transitions. For transitions U8 and U12 we have positive interference, the transition moment becomes a factor of 2 larger. Intermediate states of $^3\Pi_u$ symmetry do not play a role in transition U9, which is mainly spin-orbit coupling via $^3\Sigma^-_u$, this transition moment does not change upon inclusion of 3 $^3\Pi_u$.

5.4.4 Intensities of the Herzberg I bands

In Fig. 5.11 we plot the calculated and experimental[10] intensities for all branches of the Herzberg I (2-0) band, versus the initial state rotational quantum number N''. The units of the integrated line cross-sections are 10^{-26} cm^2

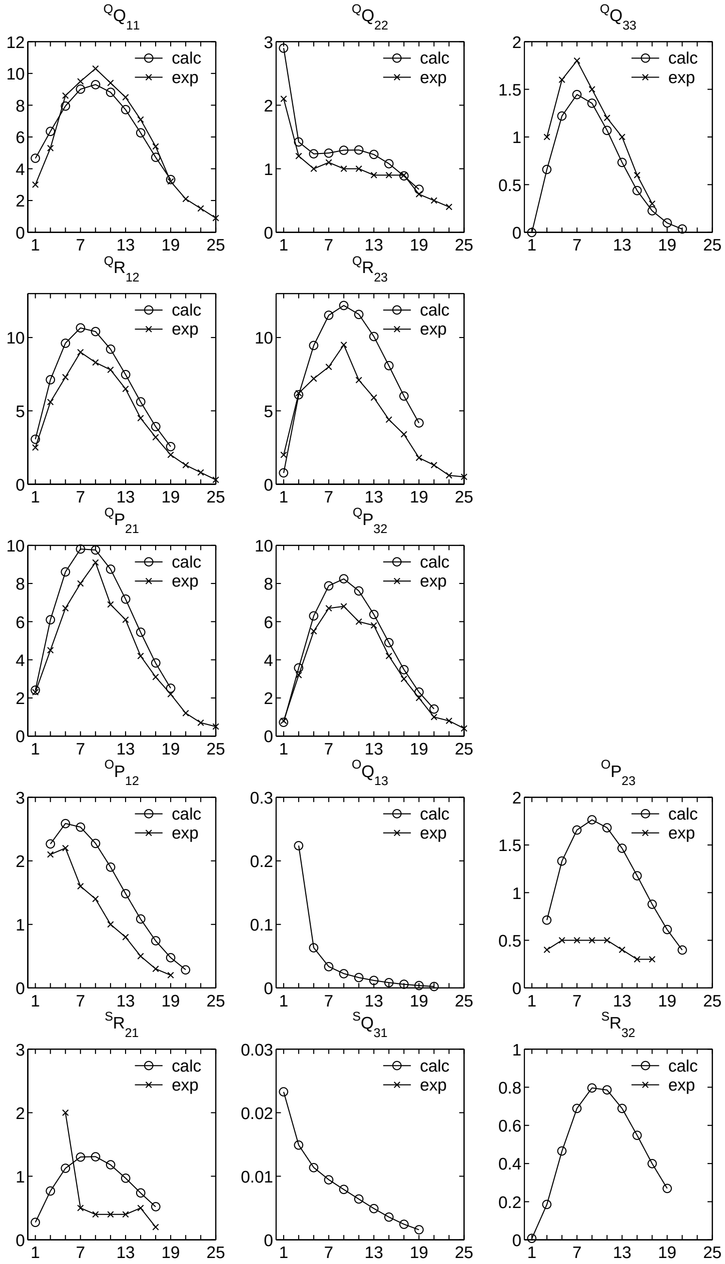

Figure 5.11: Integrated line cross-sections (in 10^{-26} cm^2 molecule^{-1} cm^{-1}) for all branches of the Herzberg I transition, (2-0) band, plotted versus initial state rotational quantum number N''.

molecule^{-1} cm^{-1}. The lower vibrational bands are so weak that the experimental data has only one significant digit. We will show later that the calculated wave functions for higher vibrational levels in the final state are localized at slightly too large R, resulting in line cross-sections that are too small. The branches are labeled ${}^{A}B_{ij}$, where A and B represent $\Delta N = N' - N''$ and $\Delta J = J' - J''$ respectively. A and B are letters, where O, P, Q, R, and S stand for ΔN, $\Delta J = -2, -1, 0, 1,$ or 2. The subscripts i and j represent the F component in final and initial state respectively. The experimental and theoretical results are in good agreement, only the weak branches ${}^{O}P_{23}$ and ${}^{S}R_{21}$ do not agree very well. The branches for which experimental data is not available (${}^{O}Q_{13}$, ${}^{S}Q_{31}$, and ${}^{S}R_{32}$) are predicted to be very weak, ${}^{O}Q_{31}$ and ${}^{S}Q_{31}$ weaker than detectable ($< 10^{-27}$ cm^2 molecule^{-1} cm^{-1}) in the current experimental setup. The line forms for the other branches are reproduced very well, note for instance the ${}^{O}P_{12}$, with a maximum at low $N'' = 5$, and the ${}^{Q}Q_{22}$ which looks strange at first sight. This branch seems to have two competing mechanisms contributing to its intensity, we will come back to this later.

For the $N'' = 9$ line of the ${}^{Q}Q_{11}$ branch, Fig. 5.12 plots the R-dependent electronic transition dipole moment matrix element in panel (a), the initial and final state vibrational wave functions $\chi^{i,v''}$ with $i = X^3\Sigma_g^-(F_{1e}), v'' = 0$ and $\chi^{f,v'}$ with $f = A^3\Sigma_u^+(F_{1f}), v' = 2$ in panel (b), and the product of vibrational wave functions and R-dependent electronic transition dipole moment matrix element in panel (c). In panel (c) all sinc-DVR grid points are plotted. The transition dipole moment matrix element $M_{f,i}$ with $f = A^3\Sigma_u^+(F_{1f}), v' = 2, J' = 10$ and $i = X^3\Sigma_g^-(F_{1e}), v'' = 0, J'' = 10$ is then given by the sum over all grid points of panel (c) [divided by $\sqrt{3}$ because of the summation over the M quantum numbers in Eq. (5.25)]. As has been pointed out before, the electronic transition dipole moment is a smooth function of R, except for small R where the Herzberg potentials cross the intermediate state potentials. At this small R, the final state vibrational wave function is almost zero, thus this has a negligible influence on the total transition dipole moment matrix element. The product of the vibrational wave functions is localized between $R = 2.35$ and 2.65 a$_0$, with a maximum at $R = 2.5$ a$_0$. We therefore analyze the electronic transition dipole moment matrix element at $R = 2.5$ a$_0$. All pathways contributing to the electronic transition dipole moments were visualized in Fig. 5.1. This showed that we expect the most important pathways to be through ${}^3\Pi_u$, ${}^3\Pi_g$, and ${}^3\Sigma_u^-$ intermediate states. In Table 5.6 we list all contributions $c^{fJ'p'}_{m'\Lambda'S'\Sigma'\Omega'}(R_n = 2.5)c^{iJ''p''}_{m''\Lambda''S''\Sigma''\Omega''}(R_n)\widetilde{M}_{\Psi',\Psi''}(R_n)$ [See Eq. 5.25] to this matrix element. The first column lists the electronic rotation basis function Ψ'' for the initial state ($J'' = 10$), the second column the final state basis function Ψ' (with $J' = 10$). The third column gives the coefficient $c^i_{''} \equiv c^{iJ''p''}_{m''\Lambda''S''\Sigma''\Omega''}(R_n = 2.5)$ of basis function Ψ'' in the initial state wave function, and the fourth column the coefficient $c^f_{'}$ of Ψ' in the final state.

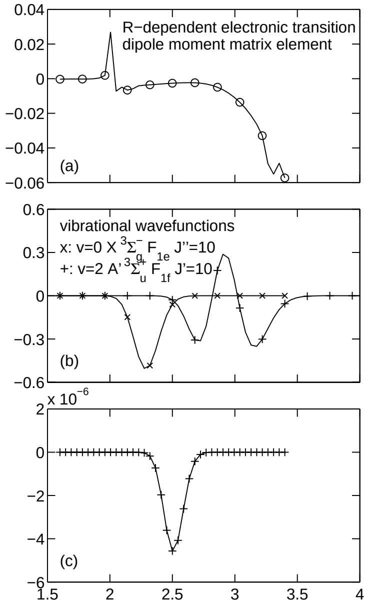

Figure 5.12: R-dependence of the components of the transition dipole matrix element M_{fi} with $f = A^3\Sigma_u^+(F_{1f}), v' = 2, J' = 10$ and $i = X^3\Sigma_g^-(F_{1e}), v'' = 0, J'' = 10$. In panel (a) the electronic transition dipole moment matrix element, in panel (b) the initial and final state vibrational wave functions, and in panel (c) the product of these three components.

The sixth column is the product of columns 3, 4, and 5: the contribution to the R-dependent electronic transition moment matrix element. The last column assigns all contributions to a pathway (intermediate state symmetry and coupling type). The table is sorted by pathway, and per pathway sorted by magnitude of the contribution. The F_1 component of the $^3\Sigma$ initial and final state is a mixture of both parity-adapted $\Omega = 0$ and $\Omega = \pm 1$ basis states, and thus all Ω components of initial, final, and intermediate states shown in Fig. 5.1 may contribute to the total line strength. In the case of $\Omega = 0$ or ± 1 $^3\Pi$ intermediate states (gerade and ungerade), both spin-orbit and orbit-rotation couplings contribute, the two mechanisms cannot be separated because of the mixed Ω in initial and final state. In the case of $^3\Pi_2$ intermediate states, the coupling mechanism must be orbit-rotation ($\Delta\Omega = 1$). The contribution of the $^3\Pi_2$ orbit-rotation pathways are about a factor five to ten smaller than the mixed spin-orbit and orbit-rotation contributions through the $\Omega = 0$ and 1 components. The spin-orbit coupling is thus probably dominant in these mixed pathways. The contribution of the Rydberg type intermediate states is generally one to two orders of magnitude smaller than the contributions via the

Table 5.6: All contributions to the electronic transition dipole moment matrix element for the $N'' = 9$ *line of the* ${}^QQ_{11}$ *branch of the (2-0) Herzberg I band, at* $R = 2.5$ a_0. *Powers of 10 have been indicated in parentheses:* 9.4(−4) *denotes* $9.4 \cdot 10^{-4}$.

Ψ''	Ψ'	$c^i_{''}$	$c^f_{'}$	$\langle\Psi'\lvert\mu_z^{\mathrm{SF}}\rvert\Psi''\rangle$	contrib.	pathway
$X^3\Sigma^-_{g,0}$	$3^3\Pi_{u,1}$	0.718	9.4(−4)	−0.71	−4.8(−4)	${}^3\Pi_u$(so,or)
$X^3\Sigma^-_{g,1}$	$3^3\Pi_{u,0}$	0.696	1.0(−3)	−0.50	−3.7(−4)	
$X^3\Sigma^-_{g,0}$	$2^3\Pi_{u,1}$	0.718	−9.6(−5)	0.15	−1.0(−5)	
$X^3\Sigma^-_{g,1}$	$2^3\Pi_{u,0}$	0.696	−1.3(−4)	0.11	−9.7(−6)	
$X^3\Sigma^-_{g,1}$	$1^3\Pi_{u,0}$	0.696	−1.3(−5)	−0.59	5.2(−6)	
$X^3\Sigma^-_{g,0}$	$1^3\Pi_{u,1}$	0.718	5.6(−6)	−0.84	−3.4(−6)	
$X^3\Sigma^-_{g,1}$	$3^3\Pi_{u,2}$	0.696	2.1(−4)	−0.50	−7.2(−5)	${}^3\Pi_u$(or)
$X^3\Sigma^-_{g,1}$	$2^3\Pi_{u,2}$	0.696	−3.3(−5)	0.10	−2.4(−6)	
$X^3\Sigma^-_{g,1}$	$1^3\Pi_{u,2}$	0.696	−7.0(−7)	−0.59	2.8(−7)	
$X^3\Sigma^-_{g,1}$	$\mathrm{Val}^3\Sigma^-_{u,1}$	0.696	−1.1(−3)	0.27	−1.9(−4)	${}^3\Sigma^-_u$(so)
$X^3\Sigma^-_{g,1}$	$\mathrm{Ryd}^3\Sigma^-_{u,1}$	0.696	−1.6(−4)	0.16	−1.8(−5)	
${}^3\Sigma^+_{g,1}$	$A^3\Sigma^+_{u,1}$	1.4(−4)	0.781	0.07	7.1(−6)	${}^3\Sigma^+_g$(so)
$\mathrm{Val}^3\Pi_{g,0}$	$A^3\Sigma^+_{u,1}$	1.8(−3)	0.781	−0.55	−7.8(−4)	${}^3\Pi_g$(so,or)
$\mathrm{Val}^3\Pi_{g,1}$	$A^3\Sigma^+_{u,0}$	1.4(−3)	0.624	−0.78	−7.0(−4)	
$\mathrm{Ryd}^3\Pi_{g,0}$	$A^3\Sigma^+_{u,1}$	−4.6(−5)	0.781	−0.03	1.2(−6)	
$\mathrm{Ryd}^3\Pi_{g,1}$	$A^3\Sigma^+_{u,0}$	1.5(−5)	0.624	−0.05	−4.2(−7)	
$\mathrm{Val}^3\Pi_{g,2}$	$A^3\Sigma^+_{u,1}$	2.6(−4)	0.781	−0.54	−1.1(−4)	${}^3\Pi_g$(or)
$\mathrm{Ryd}^3\Pi_{g,2}$	$A^3\Sigma^+_{u,1}$	7.5(−5)	0.781	−0.03	−1.9(−6)	
$\mathrm{Val}^3\Pi_{g,0}$	$A'\ {}^3\Delta_{u,1}$	1.8(−3)	1.3(−4)	−0.77	−1.9(−7)	${}^3\Pi_g$(so,or)
$\mathrm{Val}^3\Pi_{g,1}$	$A'\ {}^3\Delta_{u,2}$	1.4(−3)	3.9(−5)	−0.77	−4.3(−8)	
$\mathrm{Ryd}^3\Pi_{g,0}$	$A'\ {}^3\Delta_{u,1}$	−4.6(−5)	1.3(−4)	0.08	−4.8(−10)	
$\mathrm{Ryd}^3\Pi_{g,1}$	$A'\ {}^3\Delta_{u,2}$	1.5(−5)	3.9(−5)	0.08	4.6(−11)	
$\mathrm{Val}^3\Pi_{g,2}$	$A'\ {}^3\Delta_{u,3}$	2.6(−4)	3.6(−6)	−0.75	−7.1(−10)	${}^3\Pi_g$(or)
$\mathrm{Ryd}^3\Pi_{g,2}$	$A'\ {}^3\Delta_{u,3}$	7.5(−5)	3.6(−6)	0.08	2.1(−11)	
$\mathrm{Val}^1\Pi_{g,1}$	$c^1\Sigma^-_{u,0}$	−8.3(−4)	−3.7(−2)	0.85	2.6(−5)	${}^1\Pi_g$(so)
$\mathrm{Ryd}^1\Pi_{g,1}$	$c^1\Sigma^-_{u,0}$	1.2(−4)	−3.7(−2)	−0.20	8.6(−7)	

valence type intermediate states. This is expected, since all property matrix elements involving Rydberg states are smaller. Note that the electronic wave function for the final state contains also small components of the Herzberg II ($c^1\Sigma_u^-$) and III ($A'\,^3\Delta_u$) basis functions, these states also have a minor contribution to the transition dipole moment matrix element. Note also that all important contributions to the intensity in this $^QQ_{11}$ branch have positive interference: they are all negative, and thus add up to a negative transition dipole moment matrix element. The only positive contributions are weak and come from the $^3\Sigma_g^+$ intermediate state and the pathway through $^1\Pi_g$ (which has $c^1\Sigma_{u,0}^-$ as final state).

In Table 5.7 we show, for all thirteen branches predicted by Herzberg,[36] the contributions of the different pathways to the electronic transition dipole moment matrix element at $R = 2.5$ a$_0$. For each branch, the most intense calculated line has been selected. For some branches we present contributions for two lines, one at low and one at high rotational angular momentum quantum number. The most important pathways are through spin-orbit coupling of $A^3\Sigma_u^+$ with $^3\Sigma_u^-$, spin-orbit and orbit-rotation coupling of $A^3\Sigma_u^+$ with $^3\Pi_u$, and spin-orbit (and orbit-rotation) coupling of $X^3\Sigma_g^-$ with $^3\Pi_g$. The contributions of spin-orbit (and orbit-rotation) through $^3\Pi_u$ and $^3\Pi_g$ intermediate states have the same sign in all branches. In the strongest branches ($^QQ_{11}$, $^QR_{12}$, $^QP_{32}$, $^QR_{23}$, $^QP_{21}$) the contribution of spin-orbit coupling with $^3\Sigma_u^-$ has the same sign as the $^3\Pi$-intermediates contributions. In the weaker branches ($^QQ_{33}$, $^OP_{12}$, $^OP_{23}$, $^SR_{21}$, $^SR_{32}$, $^OQ_{13}$, $^SQ_{31}$) the $^3\Sigma_u^-$ pathway has destructive interference with the $^3\Pi$ pathways. The influence of rotation on the intensity mechanisms is clearly visible in the $^QQ_{22}$ branch, which has no spin-orbit contribution of $^3\Pi$ intermediates. The integrated line cross-section has a shoulder as function of rotational quantum number N'', indicating two competing mechanisms. At low rotation ($N'' = 1$) the dominant contribution is spin-orbit coupling of $A^3\Sigma_u^+$ with $^3\Sigma_u^-$. At higher rotation ($N'' = 11$) this spin-orbit coupling becomes less important, due to the $3j$ symbol $\begin{pmatrix} J' & 1 & J'' \\ -\Omega' & 0 & \Omega'' \end{pmatrix}$, which has a value of 0.4082 at $J'' = J' = 1$ and 0.0181 at $J'' = J' = 11$. However, the contribution of orbit-rotation coupling of $A^3\Sigma_u^+$ with $^3\Pi_u$ and $X^3\Sigma_g^-$ with $^3\Pi_g$ becomes much larger with increasing rotation. The intensity mechanism for the $^QQ_{22}$ branch thus changes from spin-orbit coupling at low N'' to orbit-rotation at high N''. The same effect is visible in the $^OQ_{13}$ and $^SQ_{31}$ branches. In these branches we have destructive interference between $^3\Pi$ spin-orbit and $^3\Sigma_u^-$ spin-orbit pathways at low rotation and between $^3\Pi$ spin-orbit and $^3\Pi$ orbit-rotation at high rotation.

The discrepancies between calculation and experiment for the Herzberg I system are largest for the weakest branches with experimental cross-sections $< 10^{-26}$ cm^2 cm^{-1} molecule^{-1}. The experimental uncertainty is also largest for the weakest lines.[10] Mérienne *et al.* estimate the uncertainty to be about 6% for intense lines (10^{-25} cm^2 cm^{-1} molecule^{-1}) to 30% for weak lines (10^{-27}

Table 5.7: Contributions of all pathways to the electronic transition dipole moment matrix element for all branches of the Herzberg I (2-0) band (in 10^{-5} a.u.).

Branch	$^QQ_{11}$	$^QQ_{22}$		$^QQ_{33}$	$^QR_{12}$	$^QP_{32}$	$^QR_{23}$	$^QP_{21}$	$^OP_{12}$	$^OP_{23}$	$^SR_{21}$	$^SR_{32}$	$^OQ_{13}$		$^SQ_{31}$	
$N'' =$	9	1	11	7	9	9	9	9	5	9	7	9	3	13	1	15
Path																
$^3\Pi_u$(so,or)	−86.9	0	0	42.6	−35.1	−33.4	31.8	31.2	−21.7	26.6	33.0	−29.8	−9.5	−10.8	−12.7	−24.0
$^3\Pi_u$(or)	−7.4	−0.7	−31.8	−2.7	8.5	−3.6	−1.1	−1.4	1.6	1.3	1.1	−6.8	0.7	9.8	0.3	12.4
$^3\Sigma_u^-$	−21.3	−110.1	−37.5	−20.8	−220.6	−162.4	192.9	197.2	168.6	−181.6	−186.1	177.0	56.8	19.8	21.2	14.4
$^3\Sigma_g^+$	0.7	3.6	1.2	0.7	7.3	5.4	−6.4	−6.5	−5.6	6.0	6.2	−5.9	−1.9	−0.7	−0.7	−0.5
$^3\Pi_g$(so,or)	−147.4	0	0	76.2	−48.3	−64.8	48.1	64.9	−32.6	40.2	66.7	−60.3	−17.5	−19.4	−20.6	−34.4
$^3\Pi_g$(or)	−11.1	−1.1	−47.1	−4.0	2.0	1.6	6.5	−11.4	−1.7	8.8	−6.3	−1.6	1.1	14.7	0.4	18.7
$^1\Pi_g$	2.7	0	0	−2.9	2.6	3.4	0	0	1.7	0	0	3.2	−0.9	−3.1	1.8	4.1
Total	−270.7	−108.2	−115.3	89.1	−283.6	−253.9	271.7	274.0	110.5	−98.8	−85.4	75.8	28.9	10.4	−10.3	−9.3

$\mathrm{cm}^2\ \mathrm{cm}^{-1}\ \mathrm{molecule}^{-1}$). The discrepancies are somewhat larger than the experimental uncertainty, but small enough to conclude that our *ab initio* calculations are of good quality, and that we elucidated the mechanism by which the Herzberg I system gains intensity. As all intermediate states contribute to all branches, it is not possible to attribute the observed discrepancies to one or several potential energy curves or coupling matrix elements.

5.4.5 Intensities of the Herzberg II bands

The experimental[10] and calculated integrated line cross sections for the $(v',0)$ Herzberg II bands (with $v' = 4, 10, 17$) are plotted in Fig. 5.13. Again the agreement between calculation and experiment is good, especially for low vibrational quantum number v'. For higher vibrational quantum numbers, the calculated intensities are too small compared to the experiment. All four calculated branches show a smooth dependence on the rotational quantum number N'', with a maximum at $N'' = 7$ or 9. The number of pathways from the ground state to $c^1\Sigma_u^-$ is much smaller than for the Herzberg I transition. In Fig. 5.2 we showed that only $^1\Pi_{g,1}$ and $^3\Pi_{u,0}$ intermediate states contribute directly to the intensity of Herzberg II. Table 5.8 lists the contributions to the electronic transition dipole moment matrix element, for the $N'' = 9$ lines of the branches of the (4-0) Herzberg II band. The intensity mechanism is generally equal for all four branches, destructive interference between spin-orbit coupling of $^1\Pi_g$ with $X^3\Sigma_g^-$ and spin-orbit coupling of $^3\Pi_u$ with $c^1\Sigma_u^-$. The pathway labeled $^3\Pi_u$(so,or) is dominantly the direct spin-orbit coupling of $^3\Pi_{u,0}$ with $c^1\Sigma_u^-$ and has also some small contributions of spin-orbit and orbit-rotation couplings of $^3\Pi_u$ with $A^3\Sigma_u^+$. These contributions cannot be separated, therefore the formal labeling is (so,or), but practically orbit-rotation does not play an important role in Herzberg II transition. There is also a small contribu-

Table 5.8: As Table 5.7 for all branches of the Herzberg II transition.

Branch	^RR	^RQ	^PQ	^PP
N'' =	9	9	9	9
Path				
$^1\Pi_g$	−68.5	−72.8	67.9	−72.2
$^3\Pi_u$(so,or)	37.0	38.2	−37.4	39.0
$^3\Pi_u$(or)	0.0	−0.0	0.0	0.0
$^3\Pi_g$(so,or)	−4.6	−6.7	3.3	−4.8
$^3\Pi_g$(or)	0.0	−0.0	0.0	−0.0
$^3\Sigma_u^-$	−0.1	−0.0	0.0	0.1
$^3\Sigma_g^+$	0.0	0.0	−0.0	−0.0
Total	−36.3	−41.4	33.7	−38.0

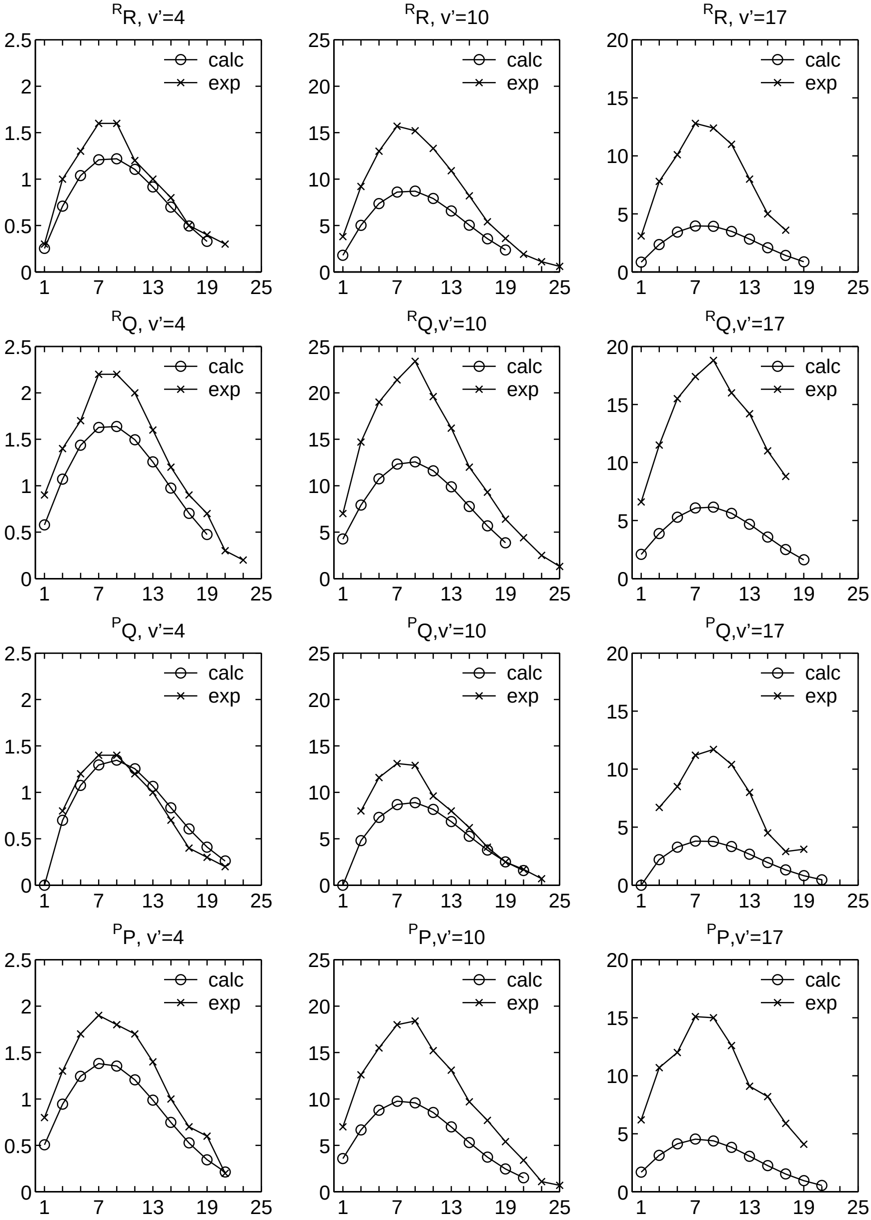

Figure 5.13: Integrated line cross-sections (in 10^{-26} *cm*^{2} *molecule*$^{-1}$ *cm*$^{-1}$*) for the four branches of the Herzberg II transition, (4-0), (10-0) and (17-0) bands, plotted versus initial state rotational quantum number* N''.

tion of a pathway of spin-orbit coupling of $X^3\Sigma_g^-$ with $^3\Pi_g$, and a subsequent perpendicular dipole transition to $A^3\Sigma_{u,0}^+$, which has a component of 0.06 in the electronic wave function. The R-dependent electronic transition dipole moment matrix elements are equal for all vibrational bands of the Herzberg II transition, because the R-dependent electronic wave functions are equal. Thus, the disagreement in the integrated line cross-sections for higher vibrational levels must be caused by the vibrational wave functions for these higher vibrational levels. The Franck-Condon overlap is between the outer tail of the ground state vibrational wave function and the inner tail of the Herzberg vibrational wave functions (Fig. 5.12). The calculated Franck-Condon overlap being too small for high v' means that the inner classical turning point is located at too large R, which is caused by a too repulsive inner limb of the Herzberg potential energy curves. A shift inwards over 1 sinc-DVR grid point (a distance of 0.045 a_0) of the Herzberg II vibrational wave functions for $v' = 10 - 17$ enlarges the Franck-Condon overlap with the ground state $v'' = 0$ wave function by a factor of 1.5, and thus enlarges the line cross-sections by a factor of $1.5^2 = 2.25$. Thus a relatively small change in the potential energy curve for the Herzberg states can yield much larger line cross-sections for high vibrational levels.

5.4.6 Intensities of the Herzberg III bands

The integrated line cross-sections for the (7-0) band of the Herzberg III transitions are plotted in Figs. 5.14 ($\Omega = 1$ subband), 5.15 ($\Omega = 2$ subband), and 5.16 ($\Omega = 3$ subband). The general agreement between calculation and experiment is slightly less good for the Herzberg III transition than for the Herzberg I and II. The $\Omega = 3$ subband of the Herzberg III transition is substantially less intense than the Herzberg I and II transition. Higher vibrational bands are more intense than lower bands, due to a more favorable Franck-Condon overlap. Therefore we analyze the (7-0) band in detail. In the previous section we concluded that the inner limbs of our Herzberg potential energy curves are somewhat too repulsive, causing our calculated integrated line cross-sections to be too small. The $v' = 7$ $A'\ {}^3\Delta_u$ vibrational level lies between the $v' = 10$ and $v' = 11$ levels of $c^1\Sigma_u^-$. The calculated integrated line cross-sections for the Herzberg II (10-0) band are about a factor of 1.5 to 2 too small. We can thus expect our calculated cross-sections for the Herzberg III (7-0) band to be too small by about the same amount. Most branches of the $\Omega = 1$ and 2 subbands are indeed slightly too weak, but all branches of the $\Omega = 3$ subband, and some of the $\Omega = 1$ subband are too weak by a much larger factor. To analyze this discrepancy between calculation and experiment, we list the contributions of the different pathways to the R-dependent electronic transition dipole moment matrix elements in Tables 5.9, 5.10, and 5.11. Our excitation mechanism for the Herzberg III transition is shown in Fig. 5.3. The major contributions come from the direct pathways through $^3\Pi$ intermediate states. The $^1\Pi_g$, $^3\Sigma_g^+$, and

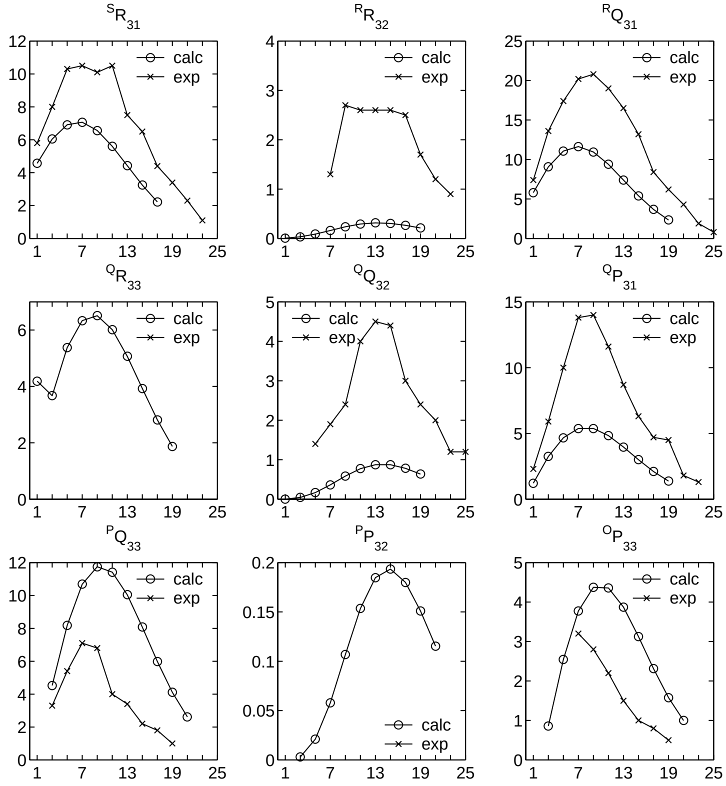

Figure 5.14: Integrated line cross-sections (in 10^{-26} cm^2 molecule^{-1} cm^{-1}) for the $\Omega = 1$ subband of the Herzberg III (7-0) band.

Table 5.9: As Table 5.7 for all branches of the $\Omega = 1$ subband of the Herzberg III transition.

Branch	$^SR_{31}$	$^RR_{32}$	$^RQ_{31}$	$^QR_{33}$	$^QQ_{32}$	$^QP_{31}$	$^PQ_{33}$	$^PP_{32}$	$^OP_{33}$
$N'' =$	7	13	7	9	13	7	9	15	9
Path									
$^3\Pi_u$(so,or)	−43.2	20.8	66.4	−41.5	0	−36.6	44.4	0.3	−35.2
$^3\Pi_u$(or)	−3.2	8.7	−3.5	3.3	−34.7	−3.7	3.7	−25.7	3.9
$^3\Pi_g$(so,or)	85.7	−16.9	−114.1	74.0	19.6	74.6	−95.3	13.7	60.4
$^3\Pi_g$(or)	0.1	−29.4	−0.1	−0.1	39.6	0.0	0.1	28.3	−0.0
$^3\Sigma_u^-$	0.0	0.0	0.0	−0.0	0.0	−0.0	−0.0	−0.0	0.0
$^3\Sigma_g^+$	−0.0	−0.0	−0.0	0.0	−0.0	0.0	0.0	0.0	−0.0
$^1\Pi_g$	0	0.0	0.0	0	0	0	−0.0	−0.0	0
Total	39.5	−16.7	−51.3	35.7	24.5	34.3	−47.2	16.5	29.1

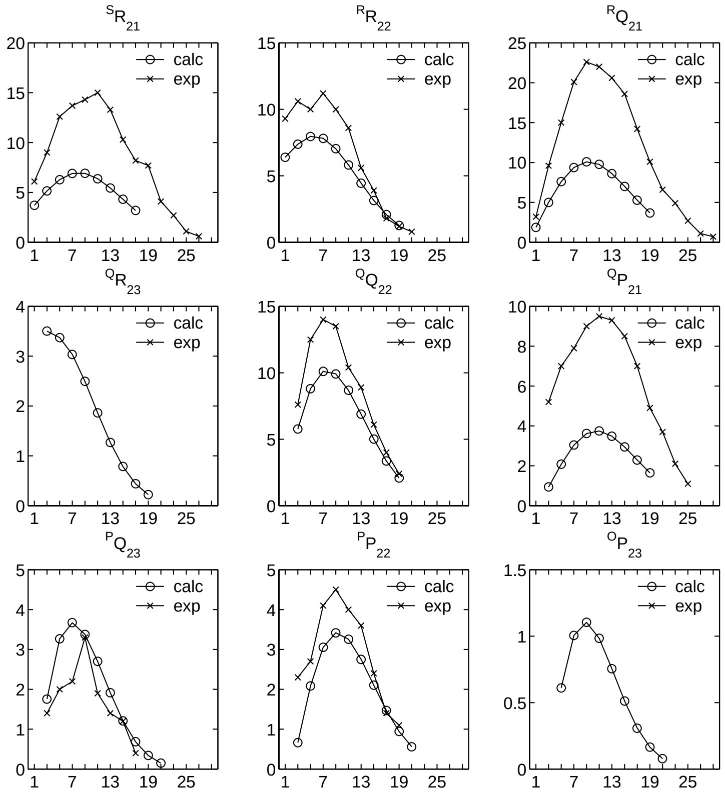

Figure 5.15: As Fig. 5.14, for the $\Omega = 2$ subband.

Table 5.10: As Table 5.7 for all branches of the $\Omega = 2$ subband of the Herzberg III transition.

Branch	$^{S}R_{21}$	$^{R}R_{22}$	$^{R}Q_{21}$	$^{Q}R_{23}$	$^{Q}Q_{22}$	$^{Q}P_{21}$	$^{P}Q_{23}$	$^{P}P_{22}$	$^{O}P_{23}$
$N'' =$	7	5	9	5	7	9	7	9	9
Path									
$^3\Pi_u$(so,or)	−15.9	0.4	26.8	−6.6	0	−15.0	11.2	1.0	−10.0
$^3\Pi_u$(or)	−33.0	−41.6	41.8	29.2	50.6	−25.7	−34.7	−33.5	22.8
$^3\Pi_g$(so,or)	89.7	79.3	−125.1	−44.7	−98.6	74.1	47.7	64.5	−27.1
$^3\Pi_g$(or)	−1.3	−1.3	2.0	0.3	2.5	−1.0	−0.6	−2.5	0.5
$^3\Sigma_u^-$	0.0	0.0	0.0	−0.0	0.0	−0.0	−0.0	−0.0	0.0
$^3\Sigma_g^+$	−0.0	−0.0	−0.0	0.0	−0.0	0.0	0.0	0.0	−0.0
$^1\Pi_g$	0	0.0	0.0	0	0	0	−0.0	0.0	0
Total	39.6	36.9	−54.4	−21.8	−45.5	32.4	23.7	29.6	−13.8

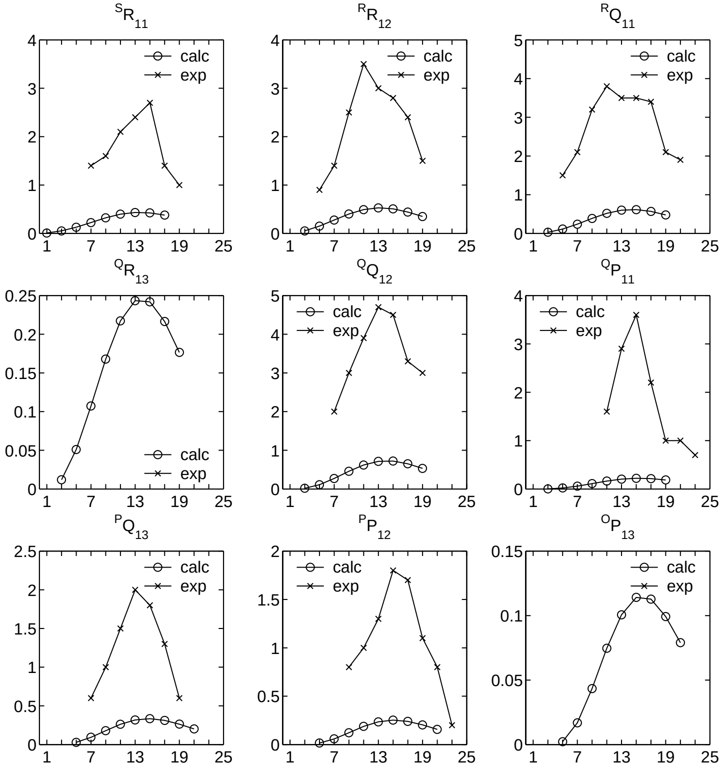

Figure 5.16: As Fig. 5.14, for the $\Omega = 3$ subband.

Table 5.11: As Table 5.7 for all branches of the $\Omega = 3$ subband of the Herzberg III transition.

Branch	$^SR_{11}$	$^RR_{12}$	$^RQ_{11}$	$^QR_{13}$	$^QQ_{12}$	$^QP_{11}$	$^PQ_{13}$	$^PP_{12}$	$^OP_{13}$
$N'' =$	13	13	15	13	13	15	15	15	15
Path									
$^3\Pi_u$(so,or)	−4.5	0.2	7.7	−3.1	0	−4.4	4.9	0.3	−3.0
$^3\Pi_u$(or)	−23.7	−30.6	33.6	19.9	35.2	−20.2	−28.3	−25.7	16.5
$^3\Pi_g$(so,or)	20.0	16.2	−30.1	−5.7	−18.9	17.9	7.1	13.7	−4.1
$^3\Pi_g$(or)	26.2	33.7	−37.5	−22.0	−39.1	22.3	31.5	28.3	−18.3
$^3\Sigma_u^-$	0.0	0.0	0.0	−0.0	0.0	−0.0	−0.0	−0.0	0.0
$^3\Sigma_g^+$	−0.0	−0.0	−0.0	0.0	−0.0	0.0	0.0	0.0	−0.0
$^1\Pi_g$	0	−0.0	−0.0	0	0	0	0.0	−0.0	0
Total	18.0	19.6	−26.3	−11.0	−22.8	15.7	15.3	16.5	−8.9

$^3\Sigma_u^-$ have only direct transitions to $A^3\Sigma_u^+$ and $c^1\Sigma_u^-$, these pathways hardly contribute. All branches have destructive interference between $^3\Pi_g$ and $^3\Pi_u$ pathways. The contribution of $^3\Pi_g$ is larger than the contribution from $^3\Pi_u$. The $^3\Pi_u$ (so,or) and $^3\Pi_u$ (or) pathways may have destructive or constructive interference. The contribution of $^3\Pi_g$ (so,or) is always large. In the branches where the calculation compares well with experiment, the contribution of $^3\Pi_g$ (or) is small. When the contribution of $^3\Pi_g$(or) is large, it has always positive interference with $^3\Pi_g$(so,or), and the calculated integrated line cross-section is too small by at least a factor of 5 in these branches. Since we need three intermediate states of $^3\Pi_u$ symmetry to explain the intensity mechanism of the Herzberg I and II transitions, we suspect that also at least one extra $^3\Pi_g$ state is needed to explain the mechanism of the Herzberg III transition. This extra state has probably a considerable $\hat{L}^{\pm}$ matrix element with $A^3\Sigma_u^+$ and $A'\,^3\Delta_u$. Its effect on the Herzberg II transition will be negligible. Its effect on the Herzberg I transition intensities will be smaller than on the Herzberg III transition, since Herzberg I has also major contributions from $^3\Sigma_u^-$, $^1\Pi_g$, $^3\Sigma_g^+$, and $^3\Pi_u$. The interference of $^3\Pi_g$ and $^3\Pi_u$ is constructive in the case of Herzberg I, thus one extra $^3\Pi_g$ intermediate state will have a much smaller relative effect there.

5.5 Conclusion

We presented an excitation mechanism for the Herzberg transitions in O_2. It is based on *ab initio* calculated potential energy curves, and spin-orbit and orbit-rotation coupling matrix elements. We included intermediate states of $^3\Sigma_u^-$, $^3\Pi_u$, $^1\Pi_g$, $^3\Pi_g$, and $^3\Sigma_g^+$ symmetry. A previous theoretical study[3] of these excitation mechanisms included only spin-orbit couplings, comparison of our spin-orbit results with these previous results shows good agreement when we include only two intermediate states of $^3\Pi_u$ symmetry. The test of our excitation mechanism on integrated line cross-sections of the Herzberg bands shows that a third $^3\Pi_u$ intermediate state is needed to account for the experimentally observed line strengths. The Herzberg I system is the most complicated of the three, it has thirteen branches, which vary in strength by more than one order of magnitude. It gains intensity by positive interference of $^3\Pi_g$ and $^3\Pi_u$ intermediates with constructive interference of $^3\Sigma_u^-$ in the stronger branches and destructive interference with $^3\Sigma_u^-$ in the weaker ones. The four branches of the Herzberg II system gain their intensity mainly through $^1\Pi_g$ intermediates, with destructive interference of $^3\Pi_u$ intermediate states. The intensity of the Herzberg III system is caused by $^3\Pi_u$ and $^3\Pi_g$ intermediates, which interfere destructively in this system. The agreement between theory and experiment is not as perfect for Herzberg III as it is for Herzberg I and II, especially for branches where orbit-rotation through $^3\Pi_g$ is important. An extra $^3\Pi_g$ intermediate state might be needed to complete the description of the excitation into the Herzberg III state.

Acknowledgments

The authors thank Ad van der Avoird and Paul E. S. Wormer for useful discussions and for carefully reading the paper. This research has been financially supported by the Council for Chemical Sciences of the Netherlands Organization for Scientific Research (CW-NWO).

Bibliography

[1] B. Buijsse, W. J. van der Zande, A. T. J. B. Eppink, D. H. Parker, B. R. Lewis, and S. T. Gibson, J. Chem. Phys. **108**, 7229 (1998).

[2] K. Yoshino, D. L. Huestis, and R. W. Nicholls, J. Quant. Spectrosc. Radiat. Transfer **60**, 1091 (1998).

[3] R. Klotz and S. D. Peyerimhoff, Mol. Phys. **57**, 573 (1986).

[4] A. C. Allison and A. Dalgarno, J. Chem. Phys. **55**, 4342 (1971).

[5] A. Amoruso, L. Crescentini, M. S. Cola, and G. Fiocco, J. Quant. Spectrosc. Radiat. Transfer **56**, 145 (1996).

[6] M. C. G. N. van Vroonhoven and G. C. Groenenboom, J. Chem. Phys. **116**, 1965 (2002), Chapter 3 of this thesis.

[7] K. Yoshino, J. R. Esmond, J. E. Murray, W. H. Parkinson, A. P. Thorne, R. C. M. Learner, and G. Cox, J. Chem. Phys. **103**, 1243 (1995).

[8] K. Yoshino, J. R. Esmond, W. H. Parkinson, A. P. Thorne, R. C. M. Learner, and G. Cox, J. Chem. Phys. **111**, 2960 (1999).

[9] K. Yoshino, J. R. Esmond, W. H. Parkinson, A. P. Thorne, R. C. M. Learner, G. Cox, and A. S.-C. Cheung, J. Chem. Phys. **112**, 9791 (2000).

[10] M.-F. Mérienne, A. Jenouvrier, B. Coquart, M. Carleer, S. Fally, R. Colin, A. C. Vandaele, and C. Hermans, J. Mol. Spectrosc. **202**, 171 (2000).

[11] V. P. Bellary and T. K. Balasubramanian, J. Quant. Spectrosc. Radiat. Transfer **45**, 283 (1991).

[12] J. P. England, B. R. Lewis, and S. T. Gibson, Can. J. Phys. **74**, 185 (1996).

[13] C. M. L. Kerr and J. K. G. Watson, Can. J. Phys. **64**, 36 (1986).

[14] D. L. Huestis, R. A. Copeland, K. Knutsen, T. G. Slanger, R. T. Jongma, M. G. H. Boogaarts, and G. Meijer, Can. J. Phys. **72**, 1109 (1994).

[15] P. R. Bunker and P. Jensen, *Molecular Symmetry and Spectroscopy*, NRC Research Press, Ottawa, 2nd edition, 1998.

[16] R. N. Zare, *Angular momentum*, Wiley, New York, 1988.

[17] G. Herzberg, *Molecular Spectra and Molecular Structure*, volume I – Spectra of Diatomic Molecules, Krieger, Malabar Florida, 2nd edition, 1950.

[18] R. McWeeny, *Methods of molecular quantum mechanics*, Academic, London, 2nd edition, 1988.

[19] A. Berning, M. Schweizer, H.-J. Werner, P. J. Knowles, and P. Palmieri, Mol. Phys. **98**, 1823 (2000).

[20] M. C. G. N. van Vroonhoven and G. C. Groenenboom, J. Chem. Phys. **117**, 5240 (2002), Chapter 4 of this thesis.

[21] H. Lefebvre-Brion and R. W. Field, *Perturbations in the spectra of diatomic molecules*, Academic Press, New York, 1986.

[22] C. Amiot and J. Verges, Can. J. Phys. **59**, 1391 (1981).

[23] G. C. Groenenboom and D. T. Colbert, J. Chem. Phys. **99**, 9681 (1993), note the mistake in the signs between the two terms in the first and second part of Eq. (48). See also D. T. Colbert and W. H. Miller, J. Chem. Phys. **96**, 1982 (1992).

[24] D. M. Brink and G. R. Satchler, *Angular Momentum*, Clarendon, Oxford, third edition, 1993.

[25] MOLPRO is a package of ab initio programs written by H.-J. Werner and P. J. Knowles, with contributions from J. Almlöf *et al.*

[26] T. H. Dunning, Jr., J. Chem. Phys. **90**, 1007 (1989).

[27] H.-J. Werner and P. J. Knowles, J. Chem. Phys. **82**, 5053 (1985).

[28] P. J. Knowles and H.-J. Werner, Chem. Phys. Lett. **115**, 259 (1985).

[29] J. A. Pople, R. Seeger, and R. Krishnan, Int. J. Quantum Chem., Quantum Chem. Symp. **11**, 149 (1977).

[30] Please e-mail Dr. G. C. Groenenboom at gerritg@theochem.kun.nl to obtain the Fortran routines.

[31] M. C. G. N. van Vroonhoven and G. C. Groenenboom, J. Chem. Phys. **116**, 1954 (2002), Chapter 2 of this thesis.

[32] J. F. Babb and A. Dalgarno, Phys. Rev. A **51**, 3021 (1995).

[33] R. S. Friedman, J. Quant. Spectrosc. Radiat. Transfer **43**, 225 (1990).

[34] B. R. Lewis, J. P. England, S. T. Gibson, M. J. Brunger, and M. Allan, Phys. Rev. A **63**, 022707 (2001).

[35] Y. Li, M. Honigmann, K. Bhanuprakash, G. Hirsch, R. J. Buenker, M. A. Dillon, and M. Kimura, J. Chem. Phys. **96**, 8314 (1992).

[36] G. Herzberg, Can. J. Phys. **30**, 185 (1952).

Summary

The atmosphere consists for about 20 % of oxygen molecules. These molecules protect us from harmful solar ultra-violet radiation through several mechanisms. Absorption of light by oxygen in the 240 − 200 nm spectral region is known as the Herzberg continuum, associated with the excitation of ground state oxygen to the three states $A^3\Sigma_u^+$, $c^1\Sigma_u^-$, and $A'\ ^3\Delta_u$. In the lower stratosphere 90 % of the photodissociation of oxygen molecules is caused by these Herzberg transitions. The oxygen atoms produced in this way may react with other O_2 molecules and form ozone, which also protects us from UV radiation.

The excitation of O_2 in the Herzberg continuum, which is electric dipole forbidden, is a complicated process, since many electronically excited states and spin-orbit and orbit-rotation couplings amongst them are involved. The subsequent photodissociation process that determines the fine structure distribution and polarization of the atomic fragments also involves many states and couplings, in particular for large O–O distances. In 1998 a photoabsorption model was constructed by Buijsse *et al.* that can be used to calculate the photoabsorption cross sections in the Herzberg continuum as a function of wavelength. This model was validated by advanced experiments in which so called fine structure resolved anisotropy parameters were determined. The model used by Buijsse *et al.* to describe the experiments was based on a simplified description of the mechanisms.

In this thesis we provide a comprehensive theoretical description and high level *ab initio* and dynamical calculations of the relevant mechanisms. Since several of the electronically excited states involved support bound states for which spectroscopic data is available we used all the available opportunities to check the correctness of our models and the quality of our calculations.

In Chapter 2 we present the calculated potential energy curves for a set of O_2 excited states, spin-orbit couplings, and the radial derivative couplings that are required in the description of the photodissociation mechanism of O_2 in the Herzberg continuum. The potentials and couplings in the bound region of the Herzberg states are tested by computation of vibrational energies, rotational constants and multiplet splittings and comparison with spectroscopic data. The potentials are accurate to better than 1 % and the errors in the spin-orbit couplings are not more than a few percent.

In Chapter 3 these potentials and couplings are used in a semiclassical calculation of the photodissociation process. We find good agreement with experimental results for the atomic fine structure distribution but only qualitative agreement for the angular distribution. We find that fragment polarization, ignored by Buijsse *et al.*, may affect the results. Also details of long range Coulomb and spin-orbit interactions are important.

In this long range region, at an internuclear separation of about 5.5 a_0, one of the electronic states involved, the $1^3\Pi_u$ state, has a shallow minimum (≈ 200 cm^{-1}), that supports two bound vibrational levels. These levels cause perturbations in the Herzberg rotational-vibrational-electronic states that have been observed. In Chapter 4 we employ our potentials and spin-orbit couplings to compute these perturbations. We find that the $1^3\Pi_u$ state is highly mixed and we provide a new assignment of the perturbing $1^3\Pi_u$ levels.

In Chapter 5 we present a fully *ab initio* study of the excitation mechanism. We present *ab initio* calculations of ten electronically excited intermediate states and couplings that give intensity to the Herzberg transitions. We test our results against experimental data on the Herzberg bands. We calculate integrated line cross-sections for all branches in the Herzberg transitions, and compare these results with experiment. The agreement is very good, especially for the Herzberg I and II transitions.

In this thesis we studied almost all aspects of the Herzberg transitions, both in the bands and in the continuum. Only possible coherence effects in the photodissociation were not investigated. This would require a full quantum scattering calculation, for which all ingredients are presented in this thesis.

Samenvatting

De atmosfeer bestaat voor ongeveer 20 % uit zuurstofmoleculen. Deze moleculen beschermen ons op verschillende manieren tegen gevaarlijke ultraviolette straling. Absorbtie van UV-licht met een golflengte van 240 tot 200 nm door zuurstof staat bekend als het Herzberg-continuum. Deze absorptie veroorzaakt de excitatie (overgang) van grondtoestand O_2 naar de drie toestanden $A^3\Sigma_u^+$, $c^1\Sigma_u^-$ en $A'\ ^3\Delta_u$. In de onderste laag van de stratosfeer wordt 90 % van de fotodissociatie van zuurstofmoleculen veroorzaakt door deze Herzberg-overgangen. De zuurstofatomen die op deze manier ontstaan kunnen met andere O_2 moleculen reageren tot ozon, dat ons ook beschermt tegen UV-straling.

De excitatie van O_2 in het Herzberg-continuum, verboden in de elektrische dipool-benadering, is een gecompliceerd proces. Deze complexiteit komt doordat er veel elektronisch aangeslagen toestanden met veel onderlinge spin-baan- en baan-rotatiekoppelingen bij betrokken zijn. Het fotodissociatieproces dat volgt op de excitatie bepaalt de verdeling over de fijnstructuurniveaus en de polarisatie van de atomaire fragmenten. Bij de fotodissociatie zijn ook weer veel andere toestanden en koppelingen betrokken, in het bijzonder voor grote O–O afstanden. In 1998 hebben Buijsse *et al.* een fotoabsorptiemodel geconstrueerd, dat gebruikt kan worden om de fotoabsorptiedoorsneden in het Herzberg-continuum te berekenen als functie van de golflengte. Zij hebben dit model gevalideerd met geavanceerde experimenten, waarin ze zogeheten fijnstructuur-opgeloste anisotropie-parameters bepaald hebben. Het model dat Buijsse *et al.* gebruikten om de experimenten te beschrijven, was gebaseerd op een vereenvoudigde beschrijving van de mechanismen achter de excitatie en de dissociatie.

In dit proefschrift geven we een uitgebreide theoretische beschrijving van de relevante mechanismen en presenteren we *ab initio* elektronenstructuur- en dynamicaberekeningen van zeer hoog niveau. Enkele van de elektronische potentialen die een rol spelen in al deze mechanismen bevatten gebonden rotatie-vibratieniveaus waarvoor experimentele spectroscopische gegevens beschikbaar zijn. We hebben deze gegevens waar mogelijk gebruikt om de correctheid van onze modellen en de kwaliteit van onze berekeningen te toetsen.

In Hoofdstuk 2 presenteren we berekende potentiaalcurven voor een aantal aangeslagen O_2 toestanden, spin-baankoppelingen en het radiële afgeleide koppelingsmatrix-element. Deze grootheden zijn nodig in de beschrijving van het fotodissociatiemechanisme van O_2 in het Herzberg-continuum. De potentialen en koppelingen worden in het gebonden gebied van de Herzberg-toestanden getest door vibratie-energieën, rotatieconstanten en multipletsplitsingen te berekenen en te vergelijken met spectroscopische metingen. De onnauwkeurigheid van de potentialen is minder dan 1 %; de fouten in de spin-baankoppelingen zijn niet groter dan een paar procent.

In Hoofdstuk 3 worden deze potentialen en koppelingen gebruikt in een semiklassieke berekening van het fotodissociatieproces. Voor de atomaire verdeling over de fijnstructuurniveaus vinden we een goede overeenstemming met experimentele resultaten. Voor de hoekverdeling is de overeenstemming alleen kwalitatief. We vinden dat de polarisatie van de fragmenten, die verwaarloosd is door Buijsse *et al.*, de resultaten kan beïnvloeden. Ook details in de Coulomb- en spin-baaninteracties op grotere O–O afstand zijn belangrijk.

Dit lange-afstandsgebied bevindt zich bij een internucleaire afstand van ongeveer 5.5 a_0. Een van de toestanden, de $1^3\Pi_u$ toestand, heeft in dit gebied een ondiep minimum ($\approx$ 200 cm^{-1}), dat twee gebonden vibratieniveaus bevat. Deze niveaus veroorzaken verstoringen in de Herzberg rotatievibratie-elektronische toestanden die ook experimenteel zijn waargenomen. In Hoofdstuk 4 gebruiken we onze potentialen en koppelingen om deze verstoringen uit te rekenen. We vinden dat de $1^3\Pi_u$ toestand een erg gemengd karakter heeft en we geven een nieuwe toekenning van de verstorende $1^3\Pi_u$ niveaus.

In Hoofdstuk 5 presenteren we een volledige *ab initio* studie van het excitatiemechanisme. We beschrijven *ab initio* berekeningen van tien elektronisch aangeslagen intermediaire toestanden en koppelingen die intensiteit aan de Herzberg-overgangen geven. We berekenen excitatiedoorsneden, geïntegreerd over de lijnen van alle "branches" in de Herzberg-overgangen en vergelijken deze met gemeten waarden. De overeenstemming is erg goed, in het bijzonder voor de Herzberg I en II overgangen.

Hiermee hebben we bijna alle aspecten van de Herzberg-overgangen bestudeerd, zowel in de banden als in het continuum. Alleen mogelijke coherentie-effecten in de fotodissociatie hebben we niet onderzocht. Hiervoor zou een volledig quantummechanische verstrooiingsberekening nodig zijn. Alle ingrediënten die nodig zijn voor een dergelijke berekening zijn te vinden in dit proefschrift.

List of publications

- Chapter 2 of this thesis:
  Mirjam C. G. N. van Vroonhoven and Gerrit C. Groenenboom, *Photodissociation of O_2 in the Herzberg continuum. I. ab initio calculation of potential energy curves and properties*, J. Chem. Phys. **116**, 1954–1964, (2002)
- Chapter 3 of this thesis:
  Mirjam C. G. N. van Vroonhoven and Gerrit C. Groenenboom, *Photodissociation of O_2 in the Herzberg continuum. II. calculation of fragment polarization and angular distribution*, J. Chem. Phys. **116**, 1965–1975, (2002)
- Chapter 4 of this thesis:
  Mirjam C. G. N. van Vroonhoven and Gerrit C. Groenenboom, *Reassignment of the O_2 spectrum just below dissociation threshold based on ab initio* calculations, J. Chem. Phys. **117**, 5240–5251, (2002)

Curriculum Vitae

Naam: Maria Cornelia Gertruda Nicolaas van Vroonhoven (Mirjam)
Geboren: 1 september 1975 te Sittard

Opleiding:

1987 – 1993: Gymnasium-β aan het Sint Janscollege te Hoensbroek-Heerlen

1993 – 1998: Studie Scheikunde aan de Katholieke Universiteit Nijmegen
Afstudeerrichting: Informatische Chemie, met een hoofdvakstage in de Theoretische Chemie.
Titel afstudeerverslag: "Quasi-adiabatic method to solve the coupled channels problem".
Afstudeerbegeleider: Dr. ir. G.C. Groenenboom.

1998 – 2003: Promotie onderzoek bij de vakgroep Theoretische Chemie aan de Katholieke Universiteit Nijmegen. Dit proefschrift is het resultaat van dit onderzoek.
Promotor: Prof. Dr. ir. A. van der Avoird
Co-promotor: Dr. ir. G.C. Groenenboom.